UNIVERSITÀ DEGLI STUDI DI NAPOLI "FEDERICO II"

DOTTORATO DI RICERCA IN

INGEGNERIA ELETTRONICA E DELLE TELECOMUNICAZIONI

XXIV ciclo

DIGITAL PROCESSING FOR FLUOROSCOPY-BASED INTERVERTEBRAL KINEMATIC ANALYSIS

TOMMASO CERCIELLO

Il Coordinatore del Corso di Dottorato

Prof. NICCOLÒ RINALDI

Il Tutore

Prof. LUIGI PAURA

I supervisori

Prof. MARIO CESARELLI

Prof. PAOLO BIFULCO

a.a. 2010 – 2011

Digital processing for fluoroscopy-based intervertebral kinematic analysis

Tesi di Dottorato in Ingegneria Elettronica e delle Telecomunicazioni

Ing. Tommaso Cerciello

Spinal degenerations can lead to segmental instability that is regarded as a major cause of back pain and is often an important factor in deciding on surgical fusion or prosthesis implant. The spinal kinematics analysis can provide useful information for diagnosis of instability and for the assessment of therapy and surgical treatment or for performance evaluation of disc prostheses. Digitized videofluoroscopy permits to analyze spinal motion during the full patient's movement, with an acceptable low X-ray dose. By recognizing the vertebrae position on successive fluoroscopic images through manual selection or automated algorithms the relative kinematics between pairs of adjacent vertebrae (i.e. intervertebral kinematics) can be easily estimated. The application of fluoroscopy in the study of spinal kinematics is, however, limited because large errors can occur in the measurements.

This thesis presents a comprehensive study of an innovative technique designed to provide a more accurate estimation of intervertebral kinematics. The recognition of vertebrae along the fluoroscopic sequence is implemented using an automated template-matching algorithm and involving a strong enhancement of the outline of vertebrae by resorting to derivative operators. Particular attention is devoted to fluoroscopic noise suppression and to edge-preserving filter design. Spline interpolation of the kinematic data extracted by videofluoroscopy is applied in order to obtain a more complete, continuous description of spinal kinematics and, more specifically, of instantaneous center of rotation.

In the introductory part of the thesis (Chapter I and II) the motivation of the study and a survey of spinal measurement techniques are given. The feasibility of videofluoroscopic analysis of spinal motion is extensively discussed. In Chapter III common kinematic parameters (such as range of motion, center of rotation, etc.) utilized for describing intervertebral spinal behaviour are presented, providing particular emphasis on the difficulty to determine a "boundary" between normal and abnormal measures of segmental kinematics for the definition of spinal instability. An extensive review of recent proposals in analysis of segmental motion is reported.

Manual recognition of anatomical landmarks in videofluoroscopy can be very problematic. It is also well-known that derivative operators, commonly used for automatic recognition, are highly sensitive to noise. Chapter IV attempts to address this issue: fluoroscopic noise model, also in presence of non-linear gray-level transformations for image enhancement, is presented; various denoising algorithms specifically designed for signal-dependent noise and AWGN are examined and a performance comparison among them is carried out.

In Chapter V the proposed algorithm for automated vertebrae recognition is described and its performance is experimentally analyzed on fluoroscopic images of a calibration model. A comparison with a manual selection procedure and other automated algorithms on real lumbar fluoroscopic sequences is presented.

In Chapter VI a continuous-time description of intervertebral motion by cubic smoothing spline interpolation is presented and the evaluation of instantaneous center of rotation of spinal motion segments by videofluoroscopy is discussed.

Declaration of authorship

I, TOMMASO CERCIELLO, declare that the thesis entitled

DIGITAL PROCESSING FOR FLUOROSCOPY-BASED INTERVERTEBRAL KINEMATIC ANALYSIS

and the work presented in the thesis are both my own, and have been generated by me as the result of my own original research. I confirm that:

- this work was done wholly or mainly while in candidature for a research degree at this University;
- where any part of this thesis has previously been submitted for a degree or any other qualification at this University or any other institution, this has been clearly stated;
- where I have consulted the published work of others, this is always clearly attributed;
- where I have quoted from the work of others, the source is always given. With the exception of such quotations, this thesis is entirely my own work;
- I have acknowledged all main sources of help;
- where the thesis is based on work done by myself jointly with others, I have made clear exactly what was done by others and what I have contributed myself;
- parts of this work have been published as:

Bifulco, P., Cesarelli, M., Cerciello, T., Romano, M., 2012 (*expected*). A continuous description of intervertebral motion by means of spline interpolation of kinematic data extracted by videofluoroscopy. Journal of Biomechanics (*submitted: under second revision*).

Cerciello, T., Romano, M., Bifulco, P., Cesarelli, M., Allen, R., 2011. Advanced template matching method for estimation of intervertebral kinematics of lumbar spine. Medical Engineering & Physics, 33 (10), 1293-1302.

Cerciello, T., Cesarelli, M., Paura, L., Bifulco, P., Romano, M., Allen, R., 2011. Noise-parameter modeling and estimation for X-ray fluoroscopy. In: Proceedings of the 4th International Symposium on Applied Sciences in Biomedical and Communication Technologies, Barcelona, Spain, ACM Proceedings, 1-5.

Cerciello, T., Bifulco, P., Cesarelli, M., Paura, L., Pasquariello, G., Allen, R., 2010. Noise reduction in fluroscopic image sequences for joint kinematics analysis. In: Proceedings of the 22nd Mediterranean Conference on Medical and Biological Engineering and Computing, Chalkidiki, Greece, Springer IFMBE Proceedings, 29, 323-326.

Cerciello, T., Bifulco, P., Cesarelli, M., Romano, M., D'Antò, M., Pasquariello, G., 2010. Continuous description of intervertebral kinematics by spline interpolation of motion data obtained processing fluoroscopic lumbar sequences. In: Proceedings of the Second National Congress of Bioengineering, Turin, Italy, Atti del Congresso Nazionale di Bioingegneria, Pàtron Editore, 1-2.

D'Antò, M., Cesarelli, M., Bifulco, P., Romano, M., Fiore, F., Cerciello, V., Cerciello, T., 2010. Perfusion CT of the liver: slop method analysis. In: Proceedings of the Second National Congress of Bioengineering, Turin, Italy, Atti del Congresso Nazionale di Bioingegneria, Pàtron Editore, 1-2.

Cerciello, T., Bifulco, P., Cesarelli, M., Romano, M., Allen, R., 2009. Automatic vertebra tracking through dynamic fluoroscopic sequence by smooth derivative template matching. In: Proceeding of the 9th International Conference on Information Technology and Applications in Biomedicine, Larnaca, Greece, IEEE Proceedings, 1-4.

Bifulco, P., Cesarelli, M., Romano, M., Allen, R., Cerciello, T., 2009. Vertebrae tracking through fluoroscopic sequence: a novel approach. In: Proceedings of the World Congress on Medical Physics and Biomedical Engineering: The Triennial Scientific Meeting of the IUPESM, Munich, Germany, Springer IFMBE Proceedings 25(4), 619-622.

Signature:

Date:

Acknowledgments

Firstly, I want to express my gratitude for the guidance and continuous support of Prof. Paolo Bifulco. I have greatly benefited from his wide and comprehensive knowledge and experience. Prof. Bifulco has always encouraged me to make my work more efficient and meaningful through his numerous advices on the subject and beyond.

I am very grateful to Prof. Mario Cesarelli for giving me the opportunity to attend my PhD and for the continuous supervision of my work. Prof. Mario Cesarelli has always been very supportive and constructive in these three years.

I would like to thank to Prof. Luigi Paura for the supervision of my work and for giving me the opportunity to face my research topic under different points of view. His contribution to Chapter IV of this thesis was fundamental.

I would like to thank to Prof. Robert Allen for giving me opportunity to study abroad, for his great kindness and for the proof reading of my publications. I would like to thank also Dr. Mike Kondracki for providing the DVF sequences and landmark data used in Chapter V and VI and for helpful discussion.

I am immensely grateful to Dr. Antonio Fratini for his support and very useful advices in these years. He has been like an older brother for me.

I am indebted to my colleagues as well. Giulio Pasquariello, Mariano Ruffo and Marcella Matrecano were always there to give a hand and an advice for the resolution of my research problems. I am very grateful for that. Felice Di Iorio and Michela D'Antò were always willing to share their experience and know-how with me.

I am also grateful to Mr. Cosmo Furno for our pleasant discussions and Ms. Gabriella Boscaino for the administrative support.

Financial support during the three years was provided by ASL Napoli 1 Centro. I thank Ing. Gennaro Rutoli for giving me the opportunity to collaborate with this Institution.

Finally, I would like to thank my family for their continual support and encouragement and my girlfriend, Giulia, for her selfless love and patience. The magnitude of their contribution cannot be expressed in few words.

Tommaso Cerciello, November 2011

For if he like a madman lived,
At least he like a wise one died.

Table of contents

List of Figures

List of Tables

Nomenclature

Abbreviations

AWGN	Additive White Gaussian Noise
DVF	Digitized Video Fluoroscopy
MRI	Magnetic Resonance Imaging
ROM	Range Of Motion
CR	Center of Rotation
FCR	Finite Center of Rotation
ICR	Instantaneous Center of Rotation
IAR	Instantaneous Axis of Rotation
IHA	Instantaneous Helical Axis of motion
NZ	Neutral Zone
EZ	Elastic Zone
FSU	Functional Spinal Unit
FE	Finite Element
RMS	Root Mean Square
SD	Standard Deviation

Symbols

x	Horizontal coordinate of image
y	Vertical coordinate of image
X,Y	Image dimensions
g	Degraded (noisy) pixel value
f	Input pixel value
q	Spatial representation of degradation function
η	Spatial representation of noise
$\tilde{f}$	Estimate of input image
$\bar{G}$	Fourier Transform of g
$\bar{F}$	Fourier Transform of f
$\bar{Q}$	Fourier Transform of q
$\bar{H}$	Fourier Transform of η
u	Horizontal coordinate of image Fourier transform
v	Vertical coordinate of image Fourier transform
N	Detected photon count
λ	Expected photon count
$\mathcal{P}(...)$	Poisson distribution
r	Image position
c_d	Constant detector gain
G	Image intensity
s	Expected image intensity
H	Noise intensity
$\mathcal{N}(...)$	Normal distribution
σ^2	Variance
$\widehat{\sigma^2}$	Sample variance
$\hat{\mu}$	Sample mean

b	Number of image bit precision
c_{ln}	Logarithmic positive constant
G_{ln}	Logarithmized image intensity
S_{ln}	Logarithmized expected image intensity
H_{ln}	Logarithmized noise intensity
γ	Gamma parameter
c_{γ}	Gamma positive constant
G_{γ}	Gamma image intensity
s_{γ}	Gamma expected image intensity
H_{γ}	Gamma noise intensity
g'	Filtered pixel value
σ_{ql}	Noise standard deviation associated with the current pixel value
w	Spatial hemi-dimension of filter
Δ_S	Average gray-level transition at vertebra edges
τ	Filter threshold
a	Step filter function
NCC	Normalized cross-correlation index
G_x	Horizontal image gradient
G_y	Vertical image gradient
T_x	Horizontal template gradient
T_y	Vertical template gradient
I,J	Template dimensions
G'	Image gradient
T'	Template gradient
θ	Angle between the image gradient and template gradient
(ICR_x,ICR_y)	Coordinates of instantaneous center of rotation
ω	Intervertebral angular velocity
v_x	Intervertebral horizontal linear velocity
v_y	Intervertebral vertical linear velocity
r_x	Horizontal translation
r_y	Vertical translation
$z(t_i)$	Noisy kinematic sample
$c(t)$	Cubic smoothing spline function
p	Smoothing parameter
H_{lp}	Transfer function of cubic smoothing spline filter
w_t	Low-pass filter cut-off frequency
I_k	Bessel function of the first kind
K	Difference between two detected photon counts
D	Difference-image intensity
$\mathcal{S}(...)$	Skellam distribution

Chapter 1

Introduction

Any fact becomes important when it's connected to another. The connection changes the perspective; it leads you to think that every detail of the world, every voice, every word written or spoken has more than its literal meaning, that it tells us of a Secret. The rule is simple: Suspect, only suspect.
Umberto Eco

1.1 Motivation of the study

Common spinal disorders can be associated with segmental instability that is considered a potential cause of back pain and an important factor in deciding on surgical treatment. Segmental instability can be recognized by estimating range of motion (i.e. relative translation and rotation of two adjacent vertebrae between full flexion and full extension) and/or finite center of rotation observed on lateral spine radiographs. This information is, however, incomplete (i.e. only end-of-range spinal positions are assumed in order to limit the X-ray dosage to the patient) and may not be sufficient to characterize any deviation of spinal motion that might be associated with spinal disorders. The use of a fluoroscopic device can offer a continuous screening of spontaneous spinal motion with an acceptable, low X-ray dose.

Fluoroscopic measurement of intervertebral kinematics is, however, generally confined to the flexion-extension planar motion and requires the assumption of no out-of-plane coupled motion (that is longer valid in flexion-extension movement). The application of fluoroscopy has been, to date, partially limited by the contention about the appropriateness of the technique: several authors have expressed concern about studying a three-dimensional dynamic system using a two-dimensional imaging method. Recently, three-dimensional vertebral displacements have been successfully represented utilising biplanar fluoroscopy. This method is, however, considered radiation intensive. In addition, biplanar fluoroscopic devices are not generally available in clinical environment.

By recognizing the vertebrae position on successive fluoroscopic images through manual landmarking or automated algorithms the intervertebral kinematics can be easily estimated. Manual landmarking is widely employed in clinical setting, but it can result in a very subjective and inaccurate procedure. Various automated approaches have been proposed in order to limit the reliance on the operator of the recognition procedures. However, regardless of the specific methodology employed (i.e. manual landmarking or automated recognition), the image noise appears to be, to date, a significant restriction to an accurate estimate of intervertebral kinematics (i.e. large relative errors can occur in the kinematic measurements as a consequence of the low quality of fluoroscopic images). Actually, the need of extremely accurate intervertebral kinematic measurements has limited the clinical application of videofluoroscopy. This is particularly true for estimation of intervertebral center of rotation.

This thesis intends to present a comprehensive study of an innovative technique designed to support a very accurate estimation of intervertebral kinematics by videofluoroscopy and to aid clinicians in diagnosing lumbar segmental instability. At this aim, the improvement of estimation accuracy with respect to the state-of-art algorithms has been addressed and clinical effectiveness of the proposed methodology has been considered as a primary target in designing the estimation procedure. A very extensive investigation of fluoroscopic noise has been presented, providing an experimental validation of the proposed noise models, and various denoising algorithms have been investigated and compared in order to obtain the

most effective trade-off between noise reduction and edge preservation for improving the accuracy of the vertebrae recognition procedures in the fluoroscopic images.

The scope of the study is presented in paragraph 1.2, while the main results are summarized in paragraph 1.3. The outline of contents is illustrated in paragraph 1.4.

The research presented in this thesis was carried out within the PhD program in Electronic and Telecommunication Engineering of University "Federico II" of Naples and has been financially supported by the Local Heath Unit ASL Napoli 1 Centro.

1.2 Scope of the study

This work of thesis is motivated by the need of an accurate estimation of intervertebral kinematics by videofluoroscopy in order to support clinicians in diagnosing segmental instability. In summary, the main objectives of this thesis are:

- to investigate noise statistics and its characteristics in fluoroscopic images, also in presence of image white-compression transformations applied for image enhancement;

- to compare different denoising algorithms in order to select the most effective in terms of noise reduction and edge preservation for quantum-limited medical images (such as fluoroscopic images);

- to design an automated vertebrae recognition procedure in order to improve accuracy of the estimation of intervertebral kinematic parameters with respect to state-of-art processing methods of *in vivo* fluoroscopic sequences;

- to investigate the feasibility of spline interpolation of discrete-time intervertebral kinematic data for obtaining a continuous-time representation of intervertebral kinematic signals and for estimating intervertebral instantaneous center of rotation.

1.3 Summary of the main results

The original contributions of this thesis can be summarized as:

- a derivation of the relationship between variance and mean of the fluoroscopic image noise after applying image gamma-correction transformation for image enhancement;

- an experimental comparison on piecewise simulated and spinal real data of various denoising algorithms specifically designed for both the signal-dependent noise and AWGN;

- the design of an automated vertebrae recognition procedure based on gradient cross-correlation template matching for estimating intervertebral kinematics during flexion-extension spinal motion in the sagittal plane and its experimental validation with respect to a calibration model and other state-of-art estimation procedures;

- a theoretical investigation of the smoothing and continuous-time representation of experimental kinematic data extracted by spinal videofluoroscopy, specifically designed to estimate the actual trajectory of ICR in lumbar spine during *in vivo* flexion-extension motion.

1.4 Structure and organisation

In the introductory part of the thesis (Chapter I and II) the motivation of the study and a survey of spinal measurement techniques are given. The feasibility of videofluoroscopic analysis of spinal motion is extensively discussed. In Chapter III common kinematic parameters (such as range of motion, center of rotation, etc.) utilized for describing intervertebral spinal behaviour are presented, providing particular emphasis on the difficulty to determine a “boundary” between normal and

abnormal measures of segmental kinematics for the definition of spinal instability. An extensive review of recent proposals in analysis of segmental motion is reported.

Manual recognition of anatomical landmarks in videofluoroscopy can be very problematic. It is also well-known that derivative operators, commonly used for automatic recognition, are highly sensitive to noise. Chapter IV attempts to address this issue: fluoroscopic noise model, also in presence of non-linear gray-level transformations for image enhancement, is presented; various denoising algorithms specifically designed for signal-dependent noise and AWGN are examined and a performance comparison among them is carried out.

In Chapter V the proposed algorithm for automated vertebrae recognition is described and its performance is experimentally analyzed on fluoroscopic images of a calibration model. A comparison with a manual selection procedure and other automated algorithms on real lumbar fluoroscopic sequences is presented.

In Chapter VI a continuous-time description of intervertebral motion by cubic smoothing spline interpolation is presented and the evaluation of instantaneous center of rotation of spinal motion segments by videofluoroscopy is discussed.

Chapter 2

Spinal measurements

Measure what is measurable, and make measurable what is not so
Galileo Galilei

Measurement of segmental motion can offer an objective, valuable method to assess functionality of spinal segments. Very accurate measurements of segmental motion can be achieved by the attachment of metal pins to the vertebral bone. This method has, however, serious limitations due to its invasiveness and its application is confined to surgical setting. Spinal motion measurements can be also inferred from the anatomical relationship between spinal column and body surface. Skin-mounted sensors have been extensively employed in clinical setting due to their non-invasiveness, simplicity and availability. Their accuracy is, however, considerably limited by skin extensibility (i.e. non-rigid connection with bones) and no reliable information about the behaviour of a single motion segment can be extracted. In the last decades imaging technologies (fluoroscopy, MRI, etc.) have allowed a significant advancement in the investigation of segmental instability. Nowadays, it is commonly accepted that radiological assessment of intervertebral kinematics is the most reliable non-invasive method for diagnosis of instability. In this Chapter some common techniques used for spinal measurements are presented, providing particular

emphasis on the appropriateness of videofluoroscopy to the analysis of spinal motion.

2.1 Skin surface measurements

Inclinometers, goniometers and skin-mounted sensors are very simple tools for clinical measurement of spinal movements. Despite their simplicity, they have proved useful in providing reference values and demonstrating range of motion changes (Burton and Tillotson, 1988). Accurate clinical measurements are, however, provided only for large spinal tracts; as a result, it is very difficult to recognize a specific intervertebral disorder (Anderson and Sweetman, 1975; Pearcy, 1986). In addition, skin markers are prone to large measurement errors due to skin extensibility (Portek et al., 1983). In a cross-comparison study of several clinical measures of lumbar spine mobility with biplanar radiography, Portek et al. (1983) pointed out little correlation between different surface techniques (inclinometer, skin distraction and plumb line) or between surface techniques and radiographic measurements (considered as reference standard).

More recent three-dimensional surface measurement devices can offer a more acceptable and effective clinical tools in investigating spinal motion (Dolan and Adams, 1993; Hindle et al., 1990; McGill and Brown, 1992; Pearcy and Hindle, 1989). Nevertheless, surface measurements have been largely superseded by radiographic methods that are currently the mainstay of movement analysis of human spine.

2.2 Radiographic measurements

Biplanar or stereo radiography can provide a highly accurate measure of three-dimensional vertebral motion (Pearcy et al., 1984a). In particular, Roentgen stereophotogrammetric, based on the attachment of small opaque markers to the vertebral bone, has been regarded as the most accurate method for measuring spinal kinematics (Axelsson et al., 1992; Selvik, 1989). Its employment is, however, limited to post-surgical assessment of intervertebral kinematics due to its invasiveness. In

addition, as a consequence of the use of two radiological sources, some general issues on X-ray exposure to the patient exist.

For these restrictions, in clinical setting diagnosis of segmental instability is generally based on uniplanar functional radiography (i.e. with the use of a single radiological equipment). Estimation of segmental motion is achieved either graphically, using superimposed serial radiographs of the type used by Penning et al. (1984), or by digitization of points marked on these radiographs and their subsequent computer-based computation, as employed by Pearcy et al. (1984ab).

Functional radiography is not, however, without risks and limitations. The number of exposures to the patient must be restricted to maintain radiation at an acceptable level. X-ray exposure restriction confines the technique to clinical measurements of few, end-of-range spinal positions. This information, though valuable, is incomplete and may not be sufficient to characterize "abnormal" spinal motion that might be associated with spinal disorders (Breen et al., 1989; Hindle et al., 1990).

2.3 Fluoroscopy

X-ray fluoroscopy provides digital-television viewing of structures inside the body, with an acceptable, low X-ray dose. In the last decades the use of fluoroscopic devices has been extended to the screen of spine during patient's motion for diagnosis of spinal disorders.

At the beginning the large doses of radiation constrained the application of X-ray fluoroscopy, but successive improvements in screen phosphors, image intensifier and flat panel detectors have allowed for increasing image quality while minimizing the radiation dose to the patient. This has widened the possibilities for clinical investigation by fluoroscopy that, despite many recent developments in magnetic resonance and computer tomography, remains the principal imaging method for continuous-time analysis of spinal motion.

The application of fluoroscopy (and also of plain radiography) in the field of spinal kinematics has been, however, partially limited by the contention about the appropriateness of the technique: several authors have expressed concern about studying a three-dimensional dynamic system using a two-dimensional imaging

method (Hindle et al., 1990). The use of a single fluoroscopic device limits spinal analysis to planar motion (e.g. flexion-extension in the sagittal plane) and requires the assumption of absence of out-of-plane coupled motion (i.e. axial rotation). Although this hypothesis can be assumed in flexion-extension motion (mainly due to the anatomic symmetry), it is no longer valid in lateral bending (Panjabi et al., 1992a; Van Mameren et al., 1992, Breen, 1991; Bifulco et al., 2002; Bifulco et al., 2010). Recently, three-dimensional displacements have been successfully represented utilising biplanar fluoroscopy (Bifulco et al., 2010). This method is, however, thought cumbersome and radiation intensive. In addition, biplanar fluoroscopic devices are not generally available in clinical environment.

2.3.1 Digitized videofluoroscopy

It has long been supposed that initial and final position plain-film radiographs of trunk bending also represent the extremes of intervertebral motion. However, using videofluoroscopy Breen et al. (1989) observed that it is quite possible for vertebral segments to undergo their largest rotation within the trunk range and not simply mirror trunk motion. Aberrant intervertebral motion may be, therefore, missed if only extreme spinal positions are evaluated.

Digitized videofluoroscopy (DVF) permits to continuously screen spinal motion: low-dose, planar motion X-rays of the spine are captured during the full patient's movement (and not only at the extremes) and digitized for successive analysis. Breen et al. (1989) were the first to demonstrate the feasibility of obtaining a quantitative analysis of lumbar intervertebral motion by DVF. However, since long sessions can be required during spinal sequence acquisition giving potentially large X-ray dose to the patient, the use of videofluoroscopy had initially raised issue of patient safety. In answer to this, Breen (1991) determined absorbed radiation dosage values for a typical patient screening and proved that X-ray exposure associated with DVF is significantly reduced with respect to standard plain-film X-ray.

DVF images can be achieved actively in the patient's upright position (i.e. spontaneous motion) or passively in the recumbent position. By recognizing the position of vertebrae from successive fluoroscopic images it is possible to estimate the motion occurred (e.g. intervertebral translation and rotation). Previous studies on

the subject utilized manual identification of anatomical landmarks for vertebrae recognition (Van Mameren et al., 1992; Breen, 1991; Simonis, 1994; Kondracki, 2001). It requires that, for each frame of a fluoroscopic spinal sequence, the operator locates vertebral landmarks (e.g. vertebra corners) by hand. This operation can, however, result in a subjective, tedious and often insufficiently accurate procedure. Indeed, large errors in the estimation of kinematic parameters may result from relatively small errors in the identification of spatial landmark coordinates (Panjabi, 1979; Panjabi et al., 1992a). More recent methods involve automated vertebrae recognition in the attempt to reduce the reliance on the operator and to improve estimation accuracy: common approaches are based on template matching techniques (Bifulco et al., 2001; Cerciello et al., 2011b; Van Mameren and Allen, 1997), vertebral body outline descriptors (McCane et al., 2006; Zheng et al., 2004) or Bayesian estimators (Lam et al., 2009), for example. Recently, Person et al. (2011) proved that the use of computer-assisted quantitative motion analysis software substantially improves the reliability of intervertebral measurements and the classification of segmental instability with respect to manual identification. Nevertheless, manual landmarking is still the most employed technique for vertebrae recognition in clinical setting.

The effectiveness of DVF analysis of spinal motion does not commonly recognize mainly due to the large errors in the kinematic measurements. Regardless of the specific methodology employed (i.e. manual landmarking or automated recognition), image noise appears to be a major limitation to an accurate estimate of intervertebral kinematics (Cerciello et al., 2011b). An appropriate denoising of fluoroscopic images should be, therefore, applied in order to improve the accuracy of kinematic estimation. In Chapter IV a literature review of a few algorithms for fluoroscopic image denoising is discussed.

2.4 Kinematic MRI

Magnetic resonance (MRI) has largely superseded radiography and fluoroscopy in clinical setting. Nevertheless, DVF is still regarded as the most suited for the

dynamic analysis of spinal motion with respect to the single slices or surfaces of structures observed on MRI scans.

Traditional MR imaging can be a powerful tool in the assessment of disc degeneration and herniation (Leone et al., 2007), but its clinical application for diagnosis of segmental instability is limited. Real-time imaging analysis required for the full investigation of spinal motion in patient's upright, weight-bearing or recumbent conditions has been, for a long time, hampered by the bore size of traditional MRI systems and their slow imaging times. More recently, kinematic MRI (often referred to as dynamic or dynamic-kinetic MRI) technology has been developed to allow clinicians to examine and analyze mechanical instability of human joint. In particular, the proliferation in clinical environment of open MRI units and short-bore high-field systems are providing a great opportunity to apply kinematic MRI techniques to spinal motion analysis.

In recent works kinematic MR imaging is resulted to be effective in quantifying the lumbar spine range of motion and changes in disc height (Leone et al., 2007). However, the potential of kinematic MRI in evaluating segmental instability has not been yet completely investigated and no comparison of accuracy of different imaging techniques (fluoroscopy, MRI, etc.) in estimating segmental kinematics has been provided.

Chapter 3

Segmental instability

The vertebral column is a flexuous and flexible column,
formed of a series of bone called vertebræ
Henry Gray

Spinal degeneration can lead to segmental instability that is suggested to be a major cause of back pain and is often an important factor in deciding on surgical fusion or prosthesis implant (Dimnet et al., 1982; Leone et al., 2007; Niosi and Oxland, 2004; Panjabi, 1992a; Panjabi, 1992b; Panjabi, 2003). Analysis of intervertebral kinematics can provide useful information for diagnosis of instability, for assessment of therapy and surgical treatment or for evaluation of performance of disc prostheses. Intervertebral kinematics is, however, difficult to measure *in vivo*: direct measurements are not clinically feasible and small errors in the estimation of vertebrae position may cause large errors in the kinematic measurements. In addition, no acceptable definition of segmental instability appears to exist. In 1990, White and Panjabi proposed a general definition of instability[1] based on the observation that

[1] "the loss of the ability of the spine under physiologic loads to maintain its pattern of displacement so that there is no initial or additional neurological deficit, no major deformity, and no incapacitating pain" (White and Panjabi, 1990).

“normal” loads imposed on an unstable spine lead to “abnormal” deformations or displacements. However, researchers do not agree on the interpretation of this definition. Some authors have suggested that greater acknowledgment should be paid to the magnitude of the force, or perturbation, required to destabilize spinal segments (Farfan and Gracovetsky, 1984). On the contrary, for others the emphasis has been on the magnitude of vertebral displacement (i.e. kinematic parameters) associated with abnormal deformations and loss of tissue stiffness (Scholten et al., 1988). This latter approach is more appreciated in clinical environment due to the possibility to more easily attained an objective, valuable measurement of the effects of instability with respect to its causes. In this Chapter a description of different radiological techniques proposed in literature for measuring kinematic descriptors of instability is provided. In addition, a wide review of recent, significant findings in the analysis of segmental motion is reported.

3.1 Radiological instability

Segmental instability is generally diagnosed by measuring abnormal vertebral displacements observed on lateral radiological projections (Leone et al., 2007). Knuttson (1944) was the first to report vacuum phenomenon in intervertebral disc and to present its association with lumbar spine instability through radiographic investigation. Since the work of Knuttson, segmental instability has been traditionally diagnosed by radiological measurements of range of motion (ROM) (i.e. intervertebral rotation and translation) between full flexion and full extension in the sagittal plane (i.e. functional radiography). White and Bernhardt (1999) proposed a checklist approach to radiographic diagnosis of instability based on evaluation of segmental ROM and/or local tissue damage. Similarly, many surgeons use, to date, flexion-extension lateral spinal views to disclose abnormal vertebral motion before deciding on surgical treatment: intervertebral anterior translation greater than 3 mm and intervertebral sagittal rotation greater than 10° are generally indications for surgical fusion or prosthesis implant (Leone et al., 2007). However, as reported by Nizard et al. (2001), this method is challenging and debatable for several reasons: its diagnostic value cannot be determined because of the lack of a non traumatic and

routinely applicable reference standard to define intervertebral instability; its reproducibility is difficult, a slight variation in patient positioning or in the direction of X-ray beam may result in a significant variation in the intervertebral ROM; the appropriate way to obtain flexion-extension radiographs and the method to measure ROM are still not standardized. In addition, clinical measurements of ROM can be affected by large errors due to low quality of radiographs and concomitant vertebral rotation about the vertical axis of spine (i.e. out-of-plane coupled motion). As a result, a large range of "abnormal" motion has been reported in literature with a substantial overlap of asymptomatic motion patterns, and the cut-off between normal and abnormal spinal movement is difficult to determine. Nevertheless, the majority of clinicians still use functional radiography for diagnosis of instability due to its simplicity, low expense and wide availability.

3.2 Range of motion

Several methods for directly measuring vertebral displacements through lateral flexion-extension radiographs have been proposed. These generally determine the segmental ROM (i.e. translation and rotation of the upper vertebra with respect to the lower of a motion segment) by end-of-range spinal positions (i.e. full flexion – full flexion).

A simple radiological assessment of vertebral translation is based on "George's line" (Yochum and Row, 1996). This line is formed by the posterior vertebral bodies as viewed on a lateral X-ray radiograph and involves no quantification, being simply a visual inspection: normally, the line should be smooth and unbroken with any deviation suggesting excessive translation (Figure 3.1). One of the earliest study that related radiological measurement of excessive lumbar translation in sagittal plane and segmental instability was conducted by Morgan and King (1957). This technique is, to date, one of the few employing the anterior borders of lumbar vertebrae (Figure 3.2). Stokes and Frymoyer (1987) improved this simple technique using biplanar radiography in order to obtain a more accurate measure of translation by reducing the artefact produced by angular motion between segments. Posner et al. (1982) adapted this method incorporating the measurement of sagittal intervertebral rotation and also

measuring translation as a percentage of vertebral body width. This approach has allowed to directly compare data extracted by different studies without the need to account for magnification or distortion of radiographs. A further modification of this measurement technique was then developed by Dupuis et al. (1985) (Figure 3.3). Although several recent works have utilized "Dupuis" method or modified version of it (Bram et al., 1998; Fujiwara et al., 2000; Murata et al., 1994), a comparison study, based on an experimental model of the L4-L5 motion segment, suggested that the method described by Morgan and King (1957) provides the overall best performance and the least interference due to concomitant motion (Shaffer et al., 1990). In this regard, it is interesting to note that the earliest and simplest technique is resulted superior to later, more elaborate approaches.

Unlike functional radiography, videofluoroscopy permits to describe intervertebral kinematics during the full patient's movement. Once located the vertebral bodies at each frame of the fluoroscopic sequence (by manual landmarking or automated recognition), the planar, rigid motion of the vertebrae results to be completely described in terms of vertebral translation and rotation (i.e. three degrees of freedom). For each pair of adjacent vertebrae (i.e. motion segment), the motion of the upper vertebra can be thus estimated with respect to the lower which is considered fixed (i.e. intervertebral kinematics) and concise measurements of segmental ROM can be easily derived from the computed kinematic data. The clinical effectiveness of *in vivo* ROM estimation by videofluoroscopy is, however, questioned: both manual marking and automated recognition of vertebral bodies might result in an insufficiently accurate procedure mainly due to the low quality of fluoroscopic images (Cerciello et al., 2011b). Recently, Cerciello and colleagues have proposed a new methodology for automated recognition of vertebrae in fluoroscopic sequences that was proved to provide an estimate of *in vivo* intervertebral kinematics with a measurement error reasonably smaller that the expected measurements of abnormal translation and rotation. This offers encouraging expectations on future clinical application of DVF analysis for diagnosis of intervertebral instability.

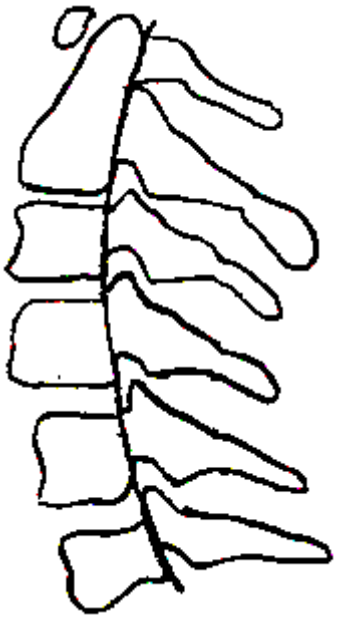

Figure 3.1. A particular of the George's line (or the Posterior Body line) for cervical spine.

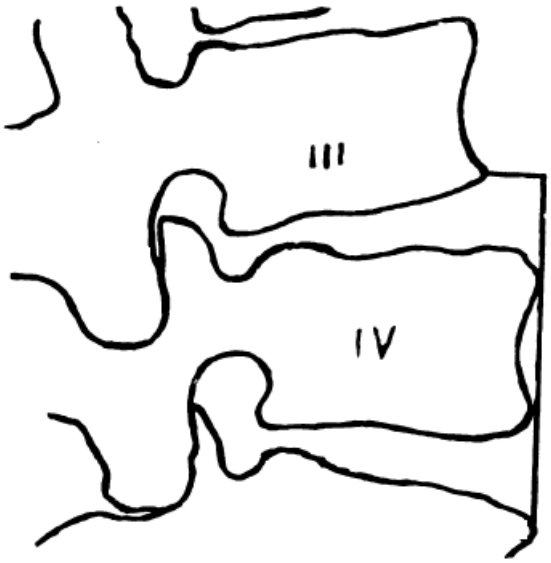

Figure 3.2. Segmental instability can be demonstrated by drawing a line along the front border of each individual vertebral body. Instability exists if the line does not pass close to the anterior lip of the vertebral body (epiphysial bone ring) immediately below and above it (from Morgan and King, 1957).

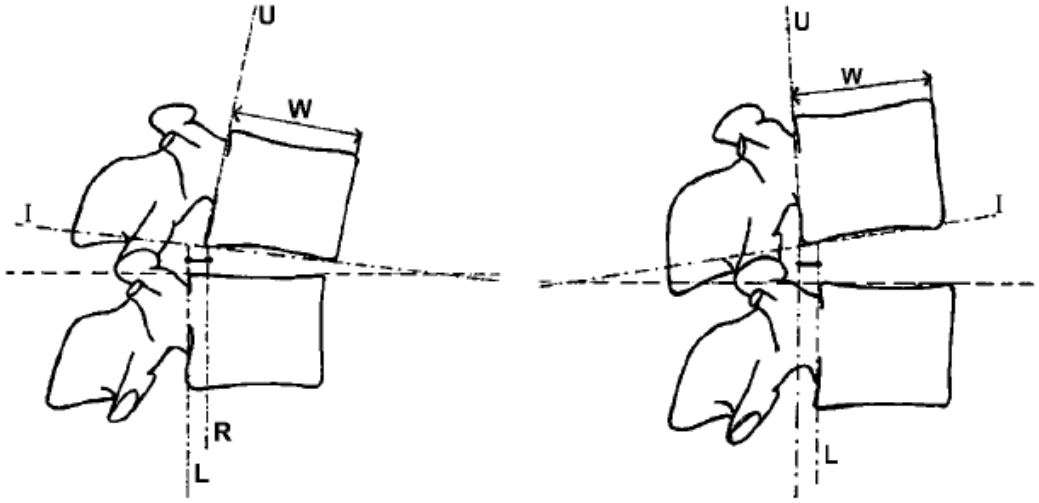

Figure 3.3. Translation is measured by drawing lines *U* and *L* along the posterior cortices of upper and lower vertebral bodies. A third line *I* along inferior endplate of the superior vertebral body is drawn and a fourth line *R* is drawn parallel to *L* through the intersection point of lines *I* and *U*. Translation is defined as the perpendicular distance between parallel lines *L* and *R*. To obviate inaccuracies due to X-ray magnification factor, translation is measured as percentage of the width of the upper vertebral body *(W)*. Sagittal rotation is measured by drawing perpendicular lines to posterior body lines (*U* and *L*) (from Dupuis et al., 1985).

3.3 Center of rotation

Center of rotation (CR) is frequently used to characterize joint motion, to detect abnormality and to evaluate treatment and rehabilitation. Its first application in the field of intervertebral kinematics appears to be that of Rosenberg (1955), who applied it to serial lumbar radiographs of thirty subjects in a preliminary attempt to establish its normal location. Since then it has gained much favour as a kinematic parameter in the study of spinal motion through lateral radiographs, especially in regard to cervical and lumbar regions.

In clinical setting a rough approximation to ICR[2], the so-called finite center of rotation (FCR), is generally assumed due to the small number of spinal positions available (to limit the X-ray exposure to the patient). By plotting FCRs obtained between different pairs of spinal positions in flexion-extension movement or

[2] If a body is both translating and rotating in a single plane, the instantaneous centre of rotation is defined as the point about which the body moves, at any instant of time, with pure rotation (Meriam and Kraige, 2002; Wilcox, 2006).

sidebending, it is possible to describe a path of CRs, or centrode. How far apart these CRs are from each other and where, in relation to the anatomy, they are located is thought to tell us something about the mechanical behaviour of each motion segment.

Several approaches for computing FCR from lateral plain-film X-rays have been proposed. Reuleaux (1875) graphically demonstrated that FCR is the point of intersection of the mid-perpendiculars of two distinct landmark displacement vectors (Figure 3.4). This approach assumes that the pairs of landmark coordinates are error-free, but if there are errors in the landmark positions the errors in FCR can be large for small angles of rotation. Panjabi (1979) presented an analytical expression for the procedure of Reuleaux, and successively White and Panjabi (1978) showed that the accuracy of the procedure can be improved by using multiple marker pairs with the weighted mean of multiple FCR estimates. Spielgeman and Woo (1987) and Crisco et al. (1994) presented procedures which only require a pair of markers. Challis (1995; 2001) firstly proposed an innovative approach based on a least-squares procedure that is resulted to be slightly more accurate than other earlier procedures. More recently, McCane et al. (2005) have provided a least-squares derivation similar to that proposed by Challis (2001), but more trivial to implement.

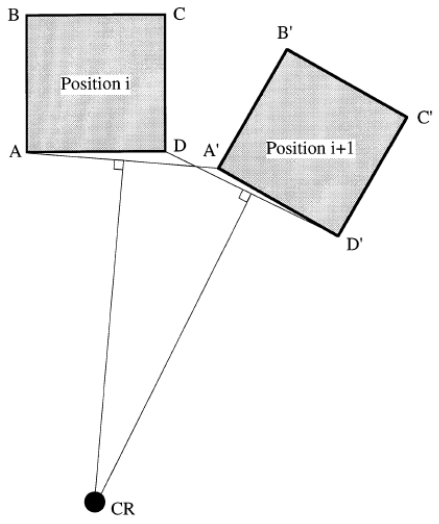

Figure 3.4. Consider a body moving from position *i* (ABCD) to position *i*+1 (A'B'C'D'). If at the two positions the coordinates of any two points (A and D, for example) are known, then the CR for this increment of movement can be calculated by erecting perpendicular bisectors between A and A' and between D and D'. The CR is at the intersection of the bisectors. Thus, the body can move from any initial position (*i*) to any final position (*i*+1) by a pure rotation about the CR (from Chen and Katona, 1999).

Large inconsistencies in FCR location have been reported in literature (see paragraph 3.7.2). They have been attributed to highly sensitive of FCR to measurement errors indeed, small measurement errors at segmental level can determine a significant misalignment of FCR, especially for small angles of rotation. In accord to this, Panjabi et al. (1982) observed that accuracy of FCR estimation is directly proportion to the magnitude of sagittal rotation (Figure 3.5). This finding has been confirmed by several, more recent studies (Chen and Katona, 1999; Panjabi et al., 1992a). In order to minimize the measurement errors, FCR is calculated between end-of-range spinal positions (i.e. full flexion and full extension), but, as a result, no information are available about the motion occurred in between the extremes of motion path. Although these aspects limit the clinical effectiveness of FCR, this continues to be a widely used parameter for evaluation of segmental instability, probably because of its inherent potential for addressing rotational and translational motion together. Indeed, it is commonly believed that an inconsistent distribution of the proportional amounts of translation and rotation, corresponding to mechanical irregularity of the joint, would result in a lengthened centrode that, therefore, may directly illustrate segmental instability. It is important to note, however, that the segmental motion occurred in between the extremes of spinal movement may be significantly varied with respect to that represented by the corresponding FCR.

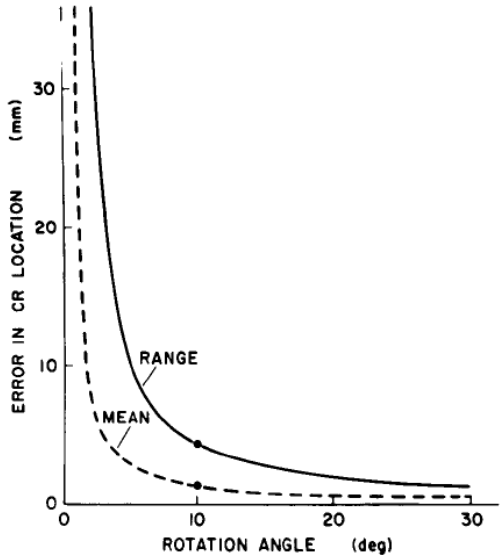

Figure 3.5. Error sensitivity of CR location as a function of the angle of rotation. It becomes increasingly difficult to determine the location of a CR of a joint as the angle of rotation decreases (form Panjabi et al., 1984).

The evaluation of CR at any instant of the patient's movement (i.e. the estimate of ICR) can be very useful for correctly diagnosing segmental instability. DVF, providing a continuous screen of spinal motion, appears to offer a perfect match for the estimation of ICR. This can be calculated along all the DVF sequence (and not only between end-of-range spinal positions) by the knowledge of intervertebral kinematics at the frame rate. Nevertheless, DVF has not been extensively used for measuring CR *in vivo* spinal motion. This is most probably a consequence of the highly sensitive of CR to measurement errors that can be significant in DVF analysis. Recently, Bifulco et al. (2011) have preliminary proposed a spline-based method designed for a continuous-time description of intervertebral motion extracted by videofluoroscopy. This study has presented, for the first time, *in vivo* ICR locations. The method seems to provide an effective technique for continuous description of intervertebral motion and, in particular, of CR, while maintaining standard clinical measurements for diagnosis of instability.

3.4 Axis of rotation

For a three-dimensional rotating body with one fixed point the concept of ICR can be extent to instantaneous axis of rotation (IAR). Generally, in planar motion the term "ICR" is generally preferred (since IAR is perpendicular to the plane and corresponds to ICR) (for instance, Cossette et al., 1971; Soudan et al., 1979; Van Mameren et al., 1992), while in those studies where the three-dimensional information can be recovered (e.g. in bi-planar radiography) the use of the term "IAR" can be more appropriate (Pearcy, 1985). This concept cannot be, however, overemphasised since the index is applied to projections or images of spine and, thus, can provide only inferential data regarding the actual three-dimensional structures. In any case, it is not bad thing that terminology, as applied to the image, should acknowledge and remind us about the true three-dimensional nature of the original examined structure. It must also be borne in mind that IAR and ICR are hypothetical concepts, not absolute measures. Their location only represent an axis or a point about which a vertebra, or other body, could be rotated to produce the roto-translation movement observed between two radiological images.

Where there are sufficient data to fully describe the complex three-dimensional motion of human joint, a more appropriate index, such as the instantaneous helical axis of motion (IHA), might be preferred (Dimnet and Guinguand, 1984; Woltring et al., 1985). This is achieved by describing the motion of a rigid body in terms of helical or screw motion. IHA is, in other words, the three-dimensional counterpart to the two-dimensional ICR. The precision of IHA index is, however, far outweighed by its conceptual complexity which at the present time prevents its use with regard to spinal motion in clinical setting (White and Panjabi, 1990).

3.5 The neutral zone

Spinal ligaments and intervertebral disc are able to vary their stiffness throughout a ROM. This viscoelastic behaviour allows greater movement within and around the neutral position (i.e. when vertebral bodies are aligned), but progressively limits motion towards the end of ROM (i.e. full flexion-extension). This suggests that lumbar spine offers little resistance to bending throughout this range (with low energy expenditure and stress in spinal soft tissue), but provides a significant opposition to potentially damaging movements at the end of range. From this information it has been inferred that subjects with poor mobility in lumbar spine can generate high, potentially harmful, stresses in lumbar disc and ligaments on simple forward bending (Panjabi, 1992c).

The region of relative ligamentous "laxity" around the neutral position is generally termed as "neutral zone" (NZ), while that part of the ROM associated with increasing ligament stiffness as "elastic zone" (EZ) (Panjabi, 1992c). Panjabi (1992c; 1998) demonstrated a method of measuring NZ *in vitro* and proposed that it represents an index of segmental instability by showing that NZ is more sensitive to injury and degeneration than the corresponding ROM. This notion continues to find support in literature.

The procedure for determining NZ involves repeated loading of a spinal specimen. After removal of the load it was noted that the specimen does not return fully to its initial position, but only partially, showing residual displacement. Loading, and hence displacement, can then undertaken in the opposite direction. When this

load/unload cycle is repeated three times, the residual displacement just prior to the third load cycle, for each direction, defines the end of the NZ. Further load/displacement form this point defines the EZ and the point midway between the two NZ is taken as the neutral position (Figure 3.6).

Although the determination of NZ is an *in vitro* process involving load/deformation data, it is possible to relate this concept to the time/displacement information generated by *in vivo* videofluoroscopic studies. For example, since viscoelasticity is a time-dependent phenomenon, one might expect the angular change through the NZ to be greater per time increment than motion during the EZ. In particular, by considering that NZ must be found at the commencement of the motion and EZ towards the end of range, Kondracki and Breen (1993) have developed a "laxity index" (analogous to NZ concept) comparing displacement during each half of a motion sequence. However, few studies have, to date, investigated the matter and *in vivo* techniques for measuring NZ appear to be still lack of confidence

.

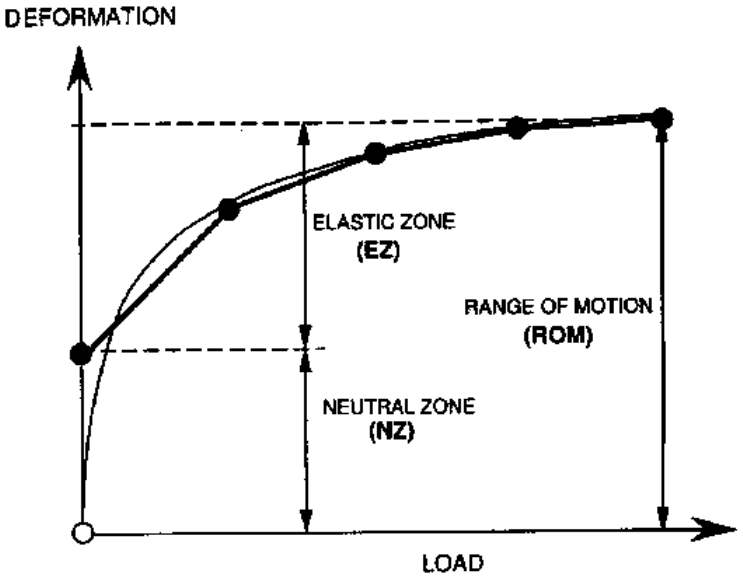

Figure 3.6. The load-deformation curve of a soft tissue or a body joint is highly nonlinear. The joint is highly flexible at low loads; it stiffnes as the load increases. To analyze this nonlinear biphasic behavior, the load-displacement curve is divided into two parts: neutral zone (NZ), the region of high flexibility; and elastic zone (EZ), the region of high stiffness. The two zones together constitute the physiological range of motion (ROM) of a joint (from Panjabi, 1992b).

3.6 A novel approach to instability

Spinal muscle actions can vary the laxity of motion segments, but these active counterparts have been long thought to have smaller influence than their corresponding passive mechanisms. In 1992 Panjabi attempted to question this approach and to conceptualise a novel model of segmental instability based on a broader view of how stability might be achieved physiologically. The concept is that human spine is a dynamic structure and thus stability cannot be reduced to a static resolution of forces. Stability must be, therefore, a function of a rapidly adapting system capable of responding to constantly fluctuating loading conditions. This necessitates the inclusion of neuromuscular elements into any dynamic model of spinal stability. In answer to this suggestion, Panjabi (1992b) proposed a model including three interacting subsystems (Figure 3.7).

The passive subsystem consists of solid structures such as vertebral bodies, facet joints and capsules, discs and ligaments. In addition, it also includes the passive mechanical properties of skeletal muscles. It is here that the concept of NZ is evident. Around the neutral position the components of the passive subsystem are unable to provide any significant resistance. This subsystem is, however, considered passive only for these structures that do not generate forces or produce movement. In other words, they are also dynamic in the sense that transducers, as an integral part of the these tissues, are capable of monitoring the mechanical behaviour of spine during motion. This information can then be fed-back to the neural subsystem. Since passive elements contribute little resistance throughout the NZ it is likely that, during this phase, they almost entirely function as transducers.

The active subsystem comprises the paraspinal musculature and tendons. These structures generate forces and moments required in maintaining stability. The force transducers, that reside in the muscle tendons and muscle spindles, are responsible for gathering information on the magnitude forces being produced by each muscle and as such as are part of the neural control subsystem.

The neural subsystem processes the information received from the various transducers. Acting on this information the active subsystem can then controlled to achieve the required tension in individual muscles until the condition for stability are

met. Panjabi (1992bc) suggested that the magnitude of muscle contraction is determined most probably on basis of information received regarding ligament strain rather than internal stresses. This is particularly expected throughout the NZ where the reactive forces are small compared to the relatively large ligament deformations.
This remarkably coordinated arrangement is likely to be capable of a great degree of compensation and optimisation and is, furthermore, liable to achieve this in a highly variable fashion.
Given that, it is not surprising that instability is difficult to evaluate. With a multitude of compensatory mechanism in place it is not unexpected that attempts to reveal instability by provocation, a common clinical technique for divulging latent abnormalities, are met with resistance by the patient. A control system of this nature is, by necessity, complex and must function on an instantaneous basis under almost infinitely variable conditions. It is, therefore, prone to dysfunction. Muscles may be recruited inappropriately, contracting too soon or too late, with insufficient force or too vigorously. Overall the objectives for immediate stability might be accomplished at the expense of long-term component damage. Accumulated injury to various anatomical tissues such as the disc, ligaments and facet joints may result in accelerated degeneration with all its attendant problems of pain and dysfunction. Furthermore, it is not inconceivable that degeneration or damage of this kind can lead to additional stability compromise.

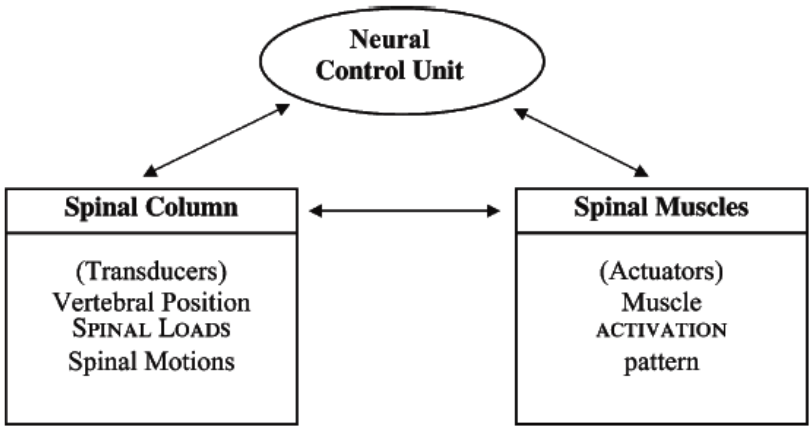

Figure 3.7. The spinal stabilizing system. It can be thought of as consisting of three subsystems: spinal column; muscles surrounding the spine; and motor control unit. The spinal column carries the loads and provides information about the position, motion, and loads of the spinal column. This information is transformed into action by the control unit. The action is provided by the muscles, which must take into consideration the spinal column, but also the dynamic changes in spinal posture and loads (from Panjabi, 2003).

3.7 A literature review

A large number of *in vitro* (or cadaveric) studies were traditionally directed to analyze segmental kinematics and its relationship with the properties of spinal tissues. By improving our understanding of how the intervertebral disc and other structures behave under differing mechanical conditions we can better explain any spinal motion changes in the patient. At this aim, in the last decades researchers have attempted to combine *in vitro* findings with the *in vivo* observations of human spine function. Nevertheless, no model of segmental instability has been, to date, proposed that adequately relates patient's symptoms, biomechanical aspects and clinical measurements. This is probably due to the complex spinal function (i.e. a large number of factors contributes to spinal motion) and the great variability of symptoms and motion changes observed between individuals.

In paragraph 3.7.1 and 3.72 recent findings in determining the intervertebral ROM and CR of lumbar spine are presented, respectively.

3.7.1 Lumbar spine range of motion

Several studies have attempted to determine the "boundary" between normal and abnormal measures of segmental ROM in order to numerically define the segmental instability. Much of the early experimental works on cadaveric specimens involved the smallest functional component of spine, the motion segment. This was described by Junghanns (1931) as comprising two adjacent vertebrae and all intervening soft tissues. The definition of motion segment, however, led to confusion since the majority of researchers left only ligamentous tissue between segments. In 1978, White and Panjabi revised the definition of motion segment including only the disc, apophyseal joint and ligaments as intervening tissues. They renamed this motion segment as the functional spinal unit (FSU) (Figure 3.8). This definition was largely accepted by the scientific community and FSU is still adopted for investigating mechanical behaviour of spine.

In 1982, Posner and colleagues undertook one of the first *in vitro* studies of lumbar and lumbosacral spine in an attempt to obtain numerically-based information on normal motion. They suggested that maximal anterior translation in normal lumbar

motion segment was no more that 2.3 mm or 8% of the anteroposterior (AP) diameter of the lower vertebral body. These figures are in good agreement with the *in vivo* stereoradiographic work of Pearcy (1985) and with a previous *in vitro* study of Nachemson (1981) who suggested that only translatory motion in excess of 4 mm between two vertebrae could safely be described as abnormal. Posner and co-workers were also one of the first groups to counsel the subdivision of lumbar spine into lumbar (L3-L5) and lumbosacral (L5-S1) regions on a functional basis. To be fair, this kinematic demarcation, particularly for flexion-extension, was first noted by Knutsson (1944). Based on the findings of Posner et al. (1982), White and Panjabi (1990) revised the figures for anterior translation and suggested that 4.5 mm or 15% of the adjacent vertebral body diameter as the upper limit of normal motion. It is interesting to note that also this revised figure is open to contention. In a more recent *in vivo* study involving radiographic measurement of asymptomatic individuals the determination of 5 mm translation was so common in the L3-L5 region, as 4 mm in the L5-S1 segments, that these values cannot be considered pathological (Tallroth e al., 1992). According to this, Soini et al. (1991), using discography and plain-film radiography on a series of 77 patients, concluded that disc degeneration seldom results in abnormal angular movement and instability of lumbar spine. Similarly, the seminal work by Boos et al. (1995) was unable to establish any significant differences between a group of patients with symptomatic disc herniation and asymptomatic volunteers matched for age, sex and work-related risk factors.

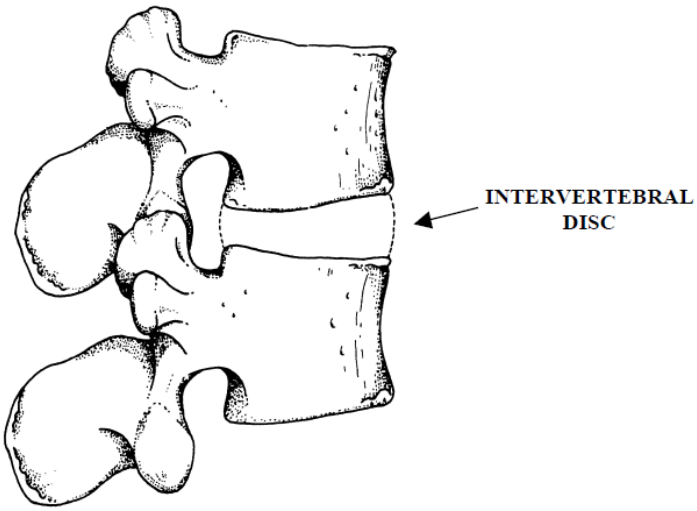

Figure 3.8. A schematic representation of the functional spinal unit (from Bogduk, 1997).

In the same years a Japanese group using both standard plain-film radiographic methods and MRI imaging of disc changes were again unable to confirm any clear association (Murata et al., 1994). The authors, employing conventional kinematic parameters of vertebral tilting and translation on 109 low back pain patients, could show only a little correlation with the degree of disc degeneration as evaluated on MRI. Using the method proposed by Dupuis et al. (1985), measurements of angular and translatory motion were taken from recumbent films, while standing, weight-bearing radiographs were used to measure disc height. With these criteria the authors claimed to identify segmental instability at all lumbar levels, even in patients who appeared to have normal discs or only mildly degenerated ones. A similar study on cervical spine instability and disc degeneration concluded that signs of instability were more likely in the early phases of degeneration (Dai, 1998). This result is in agreement with similar findings obtained by Kirkaldy-Willis (1992) and Gertzbein (1985). Another study employing MRI techniques attempted to use abnormal disc findings to predict lumbar segmental instability (Bram et al.,1998). The authors reviewed case files of 60 patients with both MR image and sagittal flexion-extension radiographs. Instability was, again, defined using measurements of shear translation adapted from Dupuis et al. (1985). Instability was assigned where the horizontal translation exceeded 3 mm. These measures were taken by radiologists blinded to the MR results of disc abnormalities. They concluded that the presence of annular tears in the disc and traction osteophytes were the findings most related to segmental lumbar instability. These conclusions are interesting, but are questionable when the sole basis for the definition of instability rests on a 3 mm shear translation. More recently, a study has claimed to have established a relationship between disc degeneration, facet arthrosis and segmental instability (Fujiwara et al., 2000a). Again using MRI and the Dupuis method for determining ranges of rotation and translation, Fujiwara and co-workers showed a positive association between disc degeneration and anterior translatory instability. Fujiwara's team employed the recumbent radiographic protocol proposed by Wood et al. (1994). This non-weight bearing and unloaded method is thought to reveal abnormal movements concealed by compression preload. In addition, they noted a negative association with facet joint osteoarthritis and both abnormal tilting movements and anteroposterior translatory

instability. In conclusion, they suggested that, with increasing degeneration of the disc and facet joints, the disc loses its anterior translation stiffness, but that facet joint osteoarthritis limits abnormal tilting movement and anteroposterior translation. Once again, however, the basis upon which the diagnosis of instability rests is subject to question. In this study, Fujiwara and colleagues subdivided translatory instability into anterior, posterior and anteroposterior by using the difference in magnitude of intervertebral displacements in flexion and extension. Where anterior displacement exceeded posterior displacement, by 1 mm or greater, the motion segment was determined to have anterior translatory instability. Their intraobserver error (1 mm for translation and 3.2° for rotation) was, however, comparable to the expected measurement of abnormal motion. In addition, their sample population comprised 70 patients with low back pain, leg symptoms or both with no matched control group. This approach is likely to lead to false conclusions because of the well-established lack of correlation between degeneration and symptoms.

These studies do not appear, thus, to provide the detailed correlative findings between spinal disorders and experimental or clinical measurements that might be anticipated. Nevertheless, the notion that intervertebral disc forms the most important restraint between spinal segments, and thus that disc degeneration is the primary cause of segmental instability, has been commonly expressed.

3.7.2 Lumbar spine center of rotation

Clinical investigations have extensively supported that CR is more sensitive to spinal disorders with respect to segmental ROM that can result within a normal range even in presence of severe disc degeneration (for instance, Fujiwara et al., 2000; Schneider et al., 2005). Similar considerations have been raised by a few studies on cervical spine kinematics which recognized CR as the most sensitive parameter to assess disc degeneration (Bogduk and Mercer, 2000; Dimnet et al., 1982; Hwang et al., 2008; Lee et al., 1997; Subramanian et al., 2007; Van Mameren et al., 1992). The knowledge of the location of CR can be, therefore, relevant for clinicians to diagnose mechanical instability of spine. A proper interpretation of CR location could allow the clinician to objectively choose the best surgical approach and the appropriate instrumentation to correct a misleading CR. Another potential value of determining

the CR is the development and evaluation of arthroplasty technoogies. This may be achieved by optimizing the CR location for implant systems attempting an CR location close to that of healthy motion segments.

Several studies have reported intervertebral FCRs of lumbar spine during flexion–extension in the sagittal plane. Yoshioka et al. (1990) studied 61 healthy cases of L1–L5 lumbar segment using 2D X-ray measurements and concluded that the flexion–extension center of rotation was 2.6 to 5.9 mm posterior to the central axis of the lower vertebral body. Gertzbein et al. (1984, 1985) reported that a greater scatter of FCRs was detected for spinal segments having morphologic changes caused by disc degeneration. In their first work Gertzbein and co-workers (1984) studied the flexion–extension FCRs of 10 cadaveric specimens and reported an average location of the FCR of 11.6 mm from the posterior edge of the vertebral body. Similar results have also been reported in separate cadaveric series by White and Panjabi (1990) and Rousseau et al. (2006ab). Xia et al. (2010), using a combined dual fluoroscopic and MR imaging technique during flexion–extension and left–right twisting of trunk, have found that the FCRs in the sagittal plane was located posterior to the centers of the lower vertebral bodies for the L2-L3 and L3-L4 segments.

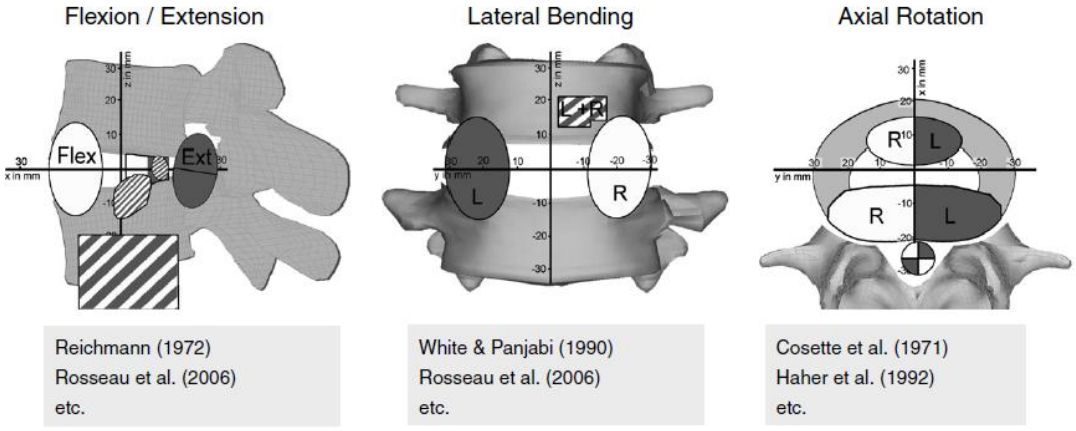

Figure 3.9. A few locations of the center of rotation in the lumbar spine proposed in literature.

Relatively few studies have reported the FCRs of lumbar vertebrae in the transverse plane. Cossette et al. (1971) determined the FCR in the anterior region of the disc for axial rotation. On the contrary, Haher et al. (1992) explored the CR in the posterior region of the disc under lower moments and posterior to the disc in the area of the neural channel for larger moments. More recently, Qiu et al. (2003) determined the location of FCRs in flexion, extension and lateral bending but for thoracic spine.

In these studies the relationship between CRs and facet joint forces remained unconsidered. Nevertheless, disc and facets work together to constrain spinal kinematics. Few *in vitro* studies have measured the facet joint forces in the lumbar spine (Rousseau et al., 2006a; Rousseau et al., 2006b; Wilson et al., 2006; Luo et al., 1996): these studies, however, require to cut through the facet joint capsules modifying biomechanical behavior. A finite element (FE) model can avoid many of the restrictions of experimental studies while providing more detailed information about the complex motion pattern and stress–strain distribution in a FSU during flexion-extension or axial motion. Shirazi-Adl et al. (1986) analyzed motion of the L2-L3 segment under an axial torque alone and combined with a compression load using a finite element (FE) model. They found that with the application of a small torque (1 Nm) the FCR in transverse plane was located roughly at the center of the vertebral body. When a larger torque was applied, however, the FCR shifted posteriorly and with hypertorsion (60Nm) it was posterior to the vertebral body. Schmidt et al. (2008a) using an FE model found, similarly, that when a larger torque (7.5Nm) was applied the FCR was closer to the facet joints.

The analysis of CR loci may have important clinical implications for evaluation of performance of disc prostheses and for deciding on the location of disc implantation. Several short and mid-range follow-up studies have recently reported satisfactory clinical results using various total disc replacement designs (Blumenthal et al., 2005; Le Huec et al., 2005; Zigler et al., 2007). Other reports argued that long-term follow-up studies of the currently available total disc replacement designs do not show better results than spinal fusion surgeries (Putzier et al., 2006). There are studies showing that the location of the artificial disc during implantation can significantly affect the clinical outcome (McAfee etal.,2005).). In clinical practice the artificial disc was generally positioned in a relatively posterior position during surgery. McAfee et al.

(2005) described that the ideal location for placement of the Charité prosthesis is 2 mm posterior to the midpoint of the vertebral body in the sagittal plane. This is consistent with the fact that the CR in the sagittal plane is at the posterior portion of the vertebra. However, no study has, to date, investigated the effect of the CR of an artificial disc in the transverse plane. From a biomechanical standpoint, changes in the location of CR in the transverse plane may introduce additional constraints to the rotational motion of lumbar spine

Many of the above mentioned studies propose findings that diverge from each other (Figure 3.9). Most probably, this is associated with the highly sensitivity of CR to measurement errors, especially when it is determined from anatomical landmarks (Panjabi, 1992a). In addition, there are no *in vivo* measurements regarding the instantaneous position of the center of rotation (i.e. ICR) and even only few data regarding this parameter *in vitro*. Recently, Wachowski et al. (2007; 2009a; 2009b; 2010) have reported, for the first time, the actual IHA for different L3-L4 cadaveric specimens that is resulted to migrate from one facet joint to the other under combined compressive loads and axial torques and from the facets to the centre of the disc in flexion-extension. Similar findings have been found by Bifulco et al. (2011) for the L2-L3 segment in a preliminary *in vivo* study based on fluoroscopic analysis of passive flexion-extension spinal movement.

3.8 Summary

Radiological measurement of segmental ROM is commonly adopted in deciding on surgical fusion or prosthesis implant. However, the definition of a "boundary" between normal and abnormal measures of segmental ROM appears to be problematic due to the large number of biomechanical aspects involved and the insufficient accuracy of measurement techniques. A great effort is taking place in order to correlate *in vitro* findings to the clinical measurements of healthy and symptomatic subjects. However, no acceptable definition of segmental instability has been, to date, proposed. Encouraging expectations on a better definition of instability would seem to derive from the assessment of segmental CR. It has been long recognized that CR is much more sensitive to disc and ligamentous degeneration

with respect to segmental ROM. An appropriate interpretation of the CR location could, therefore, permit to more objectively diagnose instability and to choose the best rehabilitative or surgical approach. At the present, large inconsistencies have been reported on FCR locations in cadaveric and *in vivo* studies. However, recent works seem to confirm the possibility to calculate the actual ICR of *in vivo* spinal segments.

Chapter 4

Noise modeling and reduction in X-ray fluoroscopy

It remains completely unknown to us what objects may be by themselves and apart from the receptivity of our senses. We know nothing but our manner of perceiving them
Immanuel Kant

Noise removal is essential in order to enhance and recover anatomical details that may be hidden in the fluoroscopic images and, consequently, to prevent large errors in kinematic measurements. As shown in the following, various image restoration and enhancement methods are available in the literature for counteract the degradation due to the noise. The effectiveness of these image restoration algorithms strongly depends on the validity of the utilized image noise model. The literature is rich in methods which assume the additive white Gaussian noise (AWGN) model. However, many important medical imaging modalities, including X-ray fluoroscopy, a reasonable noise model is the signal-dependent Poisson noise one that, of course .
In the first section of this Chapter a description of fluoroscopic noise model and of some common noise estimation techniques is presented. In the second section a performance comparison of denoising algorithms specifically designed for both the signal-dependent noise and AWGN is proposed.

4.1 Image noise modeling

The degradation process (q) of an imaging acquisition system is generally modeled as a function that, together with an additive noise term, operates on an input image f(x,y) (with $x \in [1, X]$ and $y \in [1, Y]$) to produce a degraded image g(x,y) (Figure 4.1). The objective of restoration is to obtain an estimate $\hat{f}(x,y)$ of the original image from some knowledge about the degradation function and the additive noise term. In the case that q is a linear, position-invariant process, the degraded image is given in the spatial domain by:

$$g(x, y) = f(x, y) * q(x, y) + \eta(x, y) \quad (1)$$

where q(x,y) is the spatial representation of the degradation function and the symbol "*" indicates convolution. Since the convolution in the spatial domain is equal to multiplication in the frequency domain, the previous equation can be also expressed as:

$$\overline{G}(u, v) = \overline{F}(u, v)\overline{Q}(u, v) + \overline{H}(u, v) \quad (2)$$

where the terms in capital letters are the Fourier transforms of the corresponding terms in Eq. (1).

In several situations the major degradation in an image is represented by the additive noise, while other degradation sources can be often neglected. In these cases, Eqs. (1) and (2) become:

$$g(x, y) \cong f(x, y) + \eta(x, y) \quad (3)$$

and

$$\overline{G}(u, v) \cong \overline{F}(u, v) + \overline{H}(u, v). \quad (4)$$

The principal sources of noise in digital images arise during image acquisition, pre-processing and/or transmission. The level of noise during acquisition depends on a variety of factors, such as environmental conditions, and on the quality of sensing elements. Interference in the channel used for transmission and quantization error are other typical noises superimposed to the images.

As in the previous example, image noise is frequently assumed to be additive, independent of spatial coordinates and uncorrelated with respect to the image itself (i.e. there is no correlation between pixel values and values of noise components). Because of its mathematical tractability in both the spatial and frequency domains, Gaussian noise model is also commonly used.

These assumptions (i.e. AWGN model) are, however, unreasonable in several applications and in particular for imaging acquisition systems using photon-counting devices (e.g. X-ray fluoroscopy) that are dominated by signal-dependent Poisson noise. In the next section the Poisson noise model generally adopted for X-ray fluoroscopy is extensively discussed.

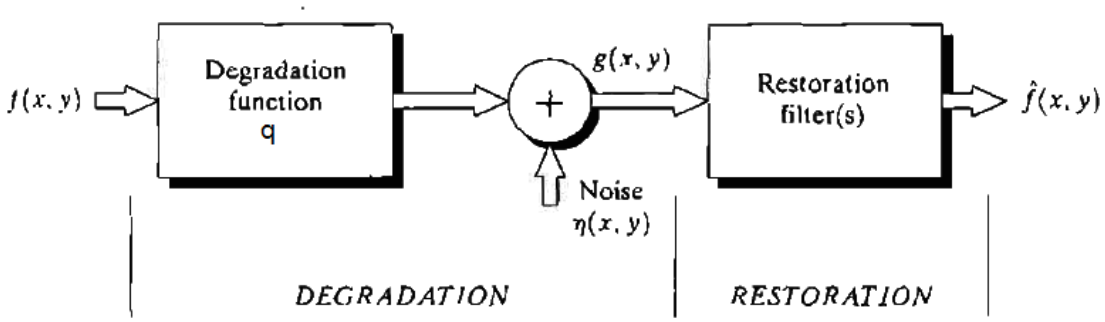

Figure 4.1. Model of the image degradation/restoration process (from Gonzalez and Woods, 1992).

4.2 Fluoroscopic noise modeling

Fluoroscopy is commonly used when dynamic images of anatomical structures are required. In these cases long sessions of X-ray exposure are necessary and the dosage to the patient must be limited. The most direct method of reducing the dosage lies in the manipulation of parameters in the X-ray generator (i.e. tube current and potential, pulse width and filtration). By varying these parameters the radiological technologist attempts to effectively administer X-ray dosage levels satisfactory to both patient's risk and image quality.

However, as a consequence of the limited number of photons available for imaging, fluoroscopic images result affected by severe noise, also known as "quantum noise". Several researchers already derived similar spatial noise models for a single or multiple fluoroscopic images (for instance, Chan et al., 1993; Harrison and Kotre, 1986; Hensel et al., 2007; Lo and Sawchuk, 1979), while the effect of non-linear gray-level image transforms (typically applied for medical image enhancement) on the statistics of fluoroscopic noise has been long ignored. In the paragraph 4.2.1 an accurate characterization of fluoroscopic noise is reported; the effect of non-linear transforms on the fluoroscopic noise characteristics is investigated in paragraph 4.2.2.

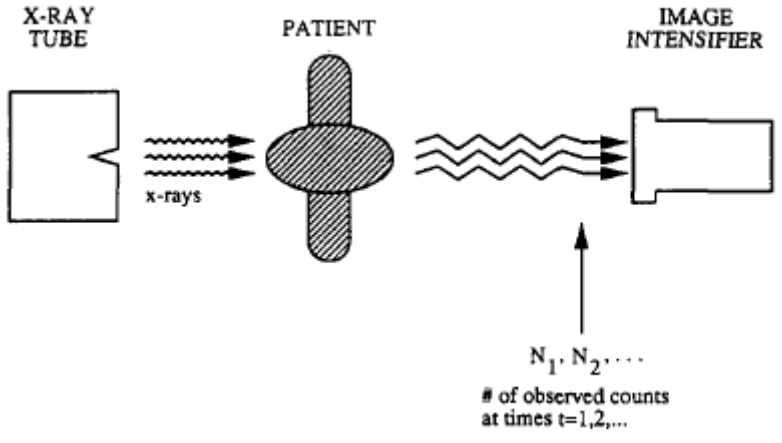

Figure 4.2. Digital fluoroscopic system front end (from Chan et al., 1993).

4.2.1 Image quantum noise

At low exposure levels the passage of photons out of the patient under a fluoroscopy system can be described by a temporally stochastic Poisson point process, as shown in Figure 4.2. The number N of photons detected at the position $r = [x,y]^T$ can be modeled in time by a Poisson distribution (for instance, Chan et al., 1993; Hensel etl al., 2007) with probability mass function equal to:

$$\mathcal{P}_N(N(r)) = \frac{[\lambda(r)]^{N(r)} e^{-\lambda(r)}}{N(r)!}, \quad (5)$$

where $\lambda >> 1$ is the expected number of photons in a given interval of time (depending on the fluoroscope frame rate) and the mean and variance of the Poisson distribution are equal to:

$$E[N(r)] = var[N(r)] = \lambda(r). \quad (6)$$

Generally, image intensity is linearly dependent on the number of detected photons (Hensel et al., 2007):

$$G(r) = c_d N(r), \quad (7)$$

with c_d positive constant detector gain depending on the characteristics of the fluoroscope. As a result, image intensity can be, in turn, modeled as Poisson-distributed:

$$\mathcal{P}_G(G(r)) = \frac{[\lambda(r)]^{\alpha G(r)} e^{-\lambda(r)}}{\alpha G(r)!} \quad (\text{with } \alpha = 1/c_d). \quad (8)$$

The Poisson noise model can be locally well-approximated with an additive sampled Gaussian noise with zero-mean and signal-dependent variance. Recently, Hensel et al. (2007) have shown that, for at least $\lambda > 10$, the Poisson noise approximation to a Gaussian distribution in X-ray fluoroscopy yields maximum relative errors below 0.1% and maximum absolute cumulative errors below 0.02.

Image intensity can be, therefore, locally decomposed as a summation of the expected pixel-intensity (s) plus a zero-mean signal-dependent noise component (for instance, Aach and Kunz, 1996; Hensel et al., 2007):

$$G(r) = s(r) + H(r) \tag{9}$$

with

$$H \sim \mathcal{N}\left(0, \sigma_H^2(s)\right). \tag{10}$$

The mean and variance of image intensity thus result:

$$E[G(r)] = s(r) = c_d E[N(r)] \tag{11}$$

and

$$var[G(r)] = var[H(r)] = c_d^2 var[N(r)] = c_d^2 E[N(r)] = c_d E[G(r)]. \tag{12}$$

According to the Poisson distribution model, variance of image noise is proportional to mean image intensity and results strongly signal-dependent (heteroscedasticity). As a consequence, given a fluoroscopic sequence the noise variance at an image location (pixel) is linearly dependent on the mean of the observed pixel values (g) at that location:

$$\widehat{\sigma_\eta^2}(r) = c_d \mu\widehat{\left(g(r)\right)}. \tag{13}$$

Although the additive Gaussian noise model has been assumed (that is more practical for addressing the problem of image non-linear transformation, discussed in paragraph 4.2.2), the relationship between noise variance and mean image intensity can be also easily derived from the properties of the Poisson distribution (see also Eqs. (7) and (8).

It should be also noted that pixel values are generally mapped within a limited data range, for instance $[0, 2^{b-1}]$ for images with b-bit precision. As a result of the noise intensity variation, pixel values could exceed the bounds of this data range. In these cases values exceeding the bounds are replaced by the bounds themselves:

$$g(r) = \max\left(0, \min\left(g(r), 2^{b-1}\right)\right). \quad (14)$$

This process is called clipping (or censoring) and corresponds to the behaviour of digital imaging sensors in the case of over- or under-exposure.

Figure 4.3 shows the experimental image noise variance as a function of the mean pixel intensity observed from a sequence of fluoroscopic images of a step phantom. To obtain the mean-variance relationship of the fluoroscopic images, about 100 repeated fluoroscopic images of the step phantom were acquired when the platform was static (image size was 1024 by 1024 pixels, image intensity had 16-bit precision; the fluoroscope system was set to 52 kVp and 28 mA.) (Figure 4.4). The mean and variance of each pixel were then calculated from the repeated measurements and plotted. It can be observed that mean and variance of the measured data are linear, which reflects the Poisson noise nature of X-ray photons. The clipping phenomena can be also observed at the extremes of the pixel value data range.

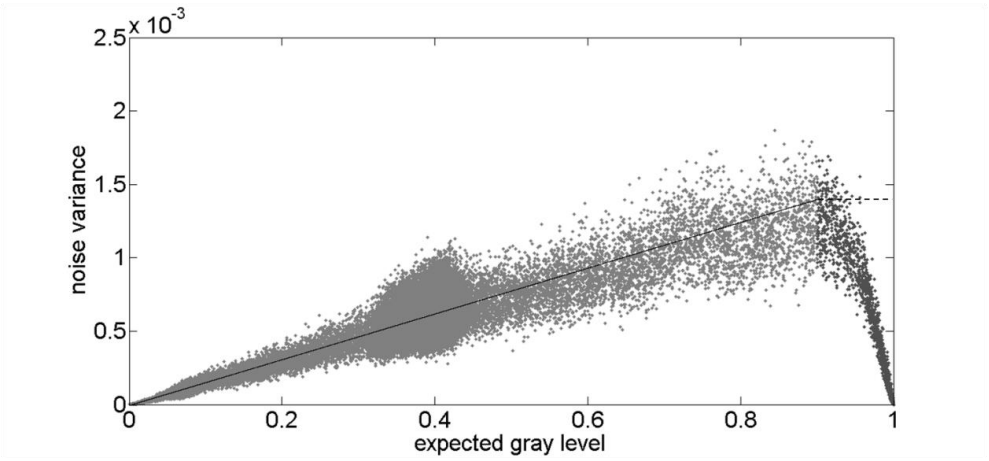

Figure 4.3. Sample noise variance (bright-gray points) obtained as a function of the mean pixel value from a fluoroscopic sequence of a step phantom. The estimated linear mean-variance characteristic is shown as a solid black line. The clipped observations (dark-gray points) have been excluded from the analysis (from Cerciello et al., 2011a).

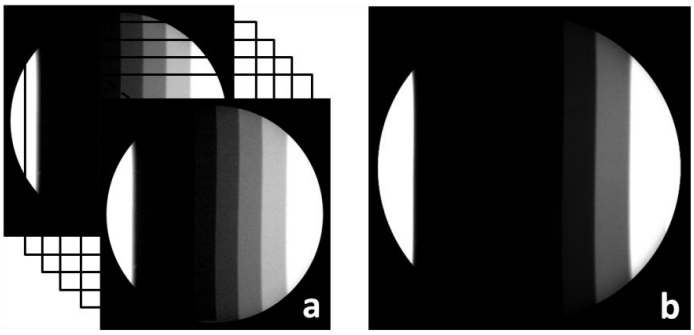

Figure 4.4. (a) Fluoroscopic images of the step phantom; (b) An enlargement of the averaged image (from Cerciello et al., 2011a).

4.2.2 White Compression

In order to compensate the exponential attenuation of X-ray photons, the logarithmic-mapping of fluoroscopic images is generally involved, according to:

$$G_{ln}(r) = c_{ln}\,\ln\big(1 + G(r)\big) \tag{15}$$

where c_{ln} is a positive constant and image intensity is incremented by one unit to avoid undefined expression (Gonzalez and Wood, 1992; Hensel et al., 2007). Logarithmic-mapping determines an expansion of darker pixels and a compression of brighter ones (i.e. white compression); in general, this improves the contrast between tissues, enhancing anatomical details, but also modifies the statistics of the noise and its characteristics.

Hensel et al. (2007) observed that after logarithmic-mapping image intensity can be still decomposed as the summation of a deterministic signal component and noise:

$$G_{ln}(r) = c_{ln}\left\{\ln\big(s(r)\big) + \ln\left[1 + \frac{H(r)}{s(r)}\right]\right\} = c_{ln}\big(s_{ln}(r) + H_{ln}(r)\big)\,, \tag{16}$$

and derived the analytical expression between noise level and mean image intensity of logarithmized data, given by:

$$\mathrm{var}[G_{ln}(r)] = c_{ln}^2\,\mathrm{var}[H_{ln}(r)] \cong c_{ln}^2 c_d \exp\left(-\frac{E[G_{ln}(r)]}{c_{ln}}\right). \tag{17}$$

More recent medical imaging devices usually introduce a luminance non-linearity by image exponentiation (i.e. gamma-correction) of the fluoroscopic images instead of using logarithmic-mapping. In this case image intensity can be expressed as:

$$G_\gamma(r) = c_\gamma G(r)^\gamma \tag{18}$$

where c_γ is a positive constant and γ-parameter for fluoroscopic medical imaging is typically ranged between 0.3 and 0.45. By varying this value it is possible to set the more appropriate level of white compression for the representation of medical image. An analytical derivation of the relationship between noise level and mean image intensity of gamma-corrected data has been recently proposed by Cerciello et al. (2011a). Cerciello and co-workers started from the observation that, according to Eqs. (9) and (18), image intensity can be re-arranged as:

$$G_\gamma(r) = c_\gamma \cdot s(r)^\gamma \cdot \left(1 + \frac{H(r)}{s(r)}\right)^\gamma = c_\gamma \cdot s(r)^\gamma \cdot \left(1 + H_\gamma(r)\right)^\gamma \tag{19}$$

and the expression $\left(1 + H_\gamma(r)\right)^\gamma$ approximated to the linear term of the binomial series. The series provide a good approximation for $H_\gamma \ll 1$ which is fulfilled in this case having mean and variance given by:

$$E\left[H_\gamma(r)\right] = 0 \tag{20}$$

$$\mathrm{var}\left[H_\gamma(r)\right] = \frac{\mathrm{var}[H(r)]}{s(r)^2} = \frac{c_d}{s(r)} = \frac{c_d}{E[G(r)]} = \frac{c_d}{c_d E[N(r)]} = \frac{1}{\lambda}. \tag{21}$$

Therefore, image intensity can be approximated as follows:

$$G_\gamma(r) \approx c_\gamma \cdot s(r)^\gamma \cdot \left(1 + \gamma H_\gamma(r)\right) = s_\gamma(r) + \gamma \cdot c_\gamma \cdot s(r)^\gamma \cdot H_\gamma(r) \tag{22}$$

and decomposed as the summation of a deterministic signal component and a noise one with variance:

$$\begin{aligned}\mathrm{var}\left[G_\gamma(r)\right] &\approx \gamma^2 \cdot c_\gamma^2 \cdot s(r)^{2\gamma} \cdot \mathrm{var}\left[H_\gamma(r)\right] = \gamma^{2} \cdot c_\gamma^2 \cdot c_d \cdot s(r)^{2\gamma-1} \\ &= \gamma^2 \cdot c_\gamma^2 \cdot c_d \cdot E[G(r)]^{2\gamma-1}. \end{aligned} \quad (23)$$

Noise level of gamma-corrected data may be referred to the signal (s_γ) observed after the gamma-correction of the image. Indeed, by noting that noise is a function of:

$$s_\gamma(r) = c_\gamma s(r)^\gamma = c_\gamma E[G(r)]^\gamma = E\left[G_\gamma(r)\right] \quad (24)$$

which is equivalent to:

$$s(r) = \left(\frac{s_\gamma(r)}{c_\gamma}\right)^{\frac{1}{\gamma}}, \quad (25)$$

noise level can be also expressed as a monotonically decreasing power function of gamma-corrected mean image intensity, given by:

$$\mathrm{var}\left[G_\gamma(r)\right] \approx \gamma^2 \cdot c_\gamma^{\frac{1}{\gamma}} \cdot c_d \cdot s_\gamma^{\,2-\frac{1}{\gamma}} = \gamma^2 \cdot c_\gamma^{\frac{1}{\gamma}} \cdot c_d \cdot E\left[G_\gamma(r)\right]^{2-\frac{1}{\gamma}}. \quad (26)$$

Figures 4.5 and 4.6 show the experimental observations of the image noise level against the mean pixel intensity obtained from fluoroscopic static images undergone logarithmic-mapping and gamma correction. The clipping phenomena at the extremes of the pixel value data range are observable again.

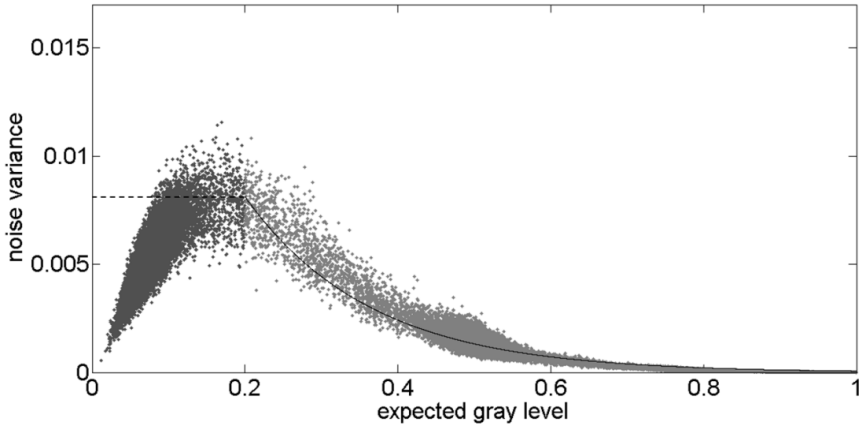

Figure 4.5. Sample noise variance (bright-gray points) obtained as a function of the mean pixel value from a logarithmized fluoroscopic sequence of a step phantom. The estimated mean-variance characteristic is shown as a solid black line. The clipped observations (dark-gray points) have been excluded from the analysis (from Cerciello et al., 2011a).

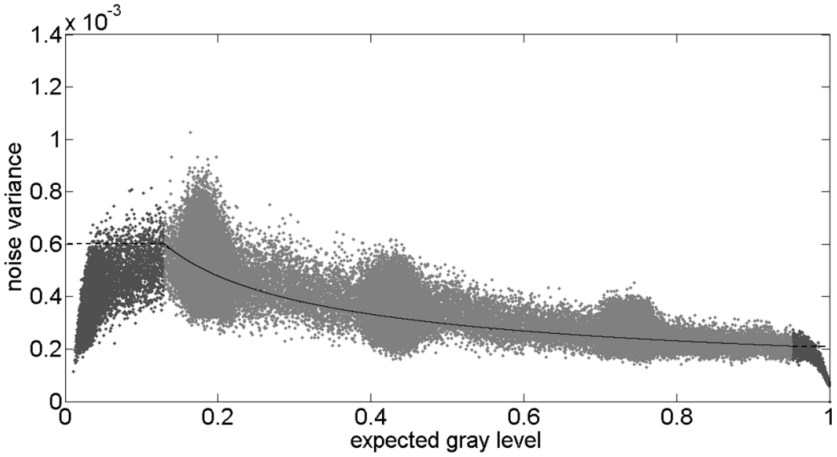

Figure 4.6. Sample noise variance (bright-gray points) obtained as a function of the mean pixel value from a gamma-corrected fluoroscopic sequence of a step phantom. The estimated mean-variance characteristic is shown as a solid black line. The clipped observations (dark-gray points) have been excluded from the analysis (from Cerciello et al., 2011a).

4.3 Estimation of noise parameters

Noise estimation methods typically assume the presence of AWGN. Under this hypothesis, common approaches estimate the noise variance in homogeneous image regions since these regions do not likely contain structure falsifying the result. More simple approaches are based on local pixel differences: if all differences between the pixel of an image block are below a selected threshold a homogeneous area is assumed and the noise level is estimated from the noise histogram (Bosco et al., 2005). Other histogram-based approaches involve more complicated procedures based on segmentation of the image in order to exclude the intensity variation associated with the signal from the estimation of noise variance. For instance, only edge pixels with a gradient below a threshold, or a percent of pixels with lowest gradients, are assumed to contribute to the estimate (Amer et al., 2005; Olsen, 1993). In any case, the definition of homogeneity for the selection of the image blocks remains problematic.

If static (i.e. motionless) images are available, a simple and very accurate noise variance estimation can be performed (see paragraph 5.2.1). However, static images are rarely obtainable and in many application the noise estimation must be performed on a single noisy image.

In a comparison study, Olsen (1993) found that pre-filtering generates a more accurate estimate of noise level with respect to the image block approach. Pre-filtering requires that an observed image is filtered to reduce the influence of structure (i.e. image inhomogeneities) and that the difference between the observed (i.e. noisy) image and the estimated (i.e. filtered) image is computed for obtaining the noise component available for the estimation. Common pre-filters are binomial and median filters. Pre-filtering method presents, however, a main restriction because the estimated image is different from the expected image (i.e. without noise); as a consequence, noise is overestimated in presence of structures.

These estimation methods are not completely valid for X-ray fluoroscopy since they assume that noise is signal-independent and provide results that are of a global nature (i.e. “average” values which are meant to be valid for the whole image). On the

contrary, an accurate pixel-wise knowledge of the fluoroscopic signal-dependent noise would be necessary in order to properly restore the image details.

Wavelet-domain image analysis can improve the accuracy of noise level estimation with respect to spatial analysis of the image content. Foi et al. (2008) have recently proposed a highly accurate algorithm based on wavelet-domain analysis for the automatic estimation of noise parameters given a single image affected by Poisson-Gaussian noise. The algorithm utilizes a special maximum-likelihood fitting of the parametric model on a collection of local wavelet-domain estimates of mean and standard-deviation. The problem of clipping (over- and under-exposure) is also taken into account, faithfully reproducing the non-linear response of imaging sensors. Foi and co-workers have adopted a noise model on the considerations that noise in digital imaging sensors is signal-dependent with a Poissonian component, modeling the photon sensing, and a Gaussian component, for the remaining stationary disturbances in output data. Even if this model has been proposed for commercial imaging sensors it can be applied to X-ray fluoroscopy (in this case the Gaussian component of noise model can be neglected).

Noise level estimation is commonly performed in spatial or transform domains, while less emphasis has been devoted in literature to the estimation of noise in time (i.e. from multiple images). Recently, Foi and colleagues (2007) have also presented an innovative approach for measuring the temporal noise in raw-data of digital imaging sensors. The method is specially designed to estimate the standard-deviation of noise as a function of the expectation of pixel raw-data output. By using an automatic segmentation of the recorded images, Foi and colleagues separate samples with different expected output and calculate their standard-deviation. Unlike other techniques that require an uniform target, their method benefits from the target non-uniformity by simultaneously estimating the variance function over a large range of output values and has the quality of showing that multiple images can provide a significant advantage in measuring the noise level.

4.4 Denoising of fluoroscopic images

Medical images are often noisy owing to the physical mechanisms of the acquisition process. The majority of the denoising algorithms assume additive white Gaussian noise (AWGN). However, common medical image modalities are degraded by non-Gaussian noise. In particular, Poisson noise is generally adopted for modeling the counting processes associated with many imaging modalities such as PET, SPECT or X-ray fluoroscopy. A comparison of several denoising algorithms specifically designed for signal-dependent Poisson noise and for AWGN is carried on. Denoising algorithms have been applied to simulated and real data affected by Poisson noise. Denoising algorithms are presented in paragraph 4.4.1. Results of the performance comparison are reported in paragraph 4.4.2 and 4.4.3 for the case of simulated data and real data, respectively.

4.4.1 Denoising algorithms

An adaptive averaging spatial filter (AVS) specifically designed for signal-dependent noise has been considered (see also Chapter V) (Cerciello et al., 2011b). The filter performs the average of the only neighbouring pixels that differ less than a selected threshold from the gray level of the central pixel of the filter mask. The threshold is set to two times the estimated standard deviation of the noise associated with the local gray level. This permits to preserve image edges with a gray-level range greater than the local noise intensity.

The TLS is an image denoising algorithm based on total least square technique for a mixture of independent additive and multiplicative Gaussian noise (Hirakawa and Parks, 2006). Although this noise is characteristic of CMOS sensors, it can be extended to the case of X-ray fluoroscopic images. An ideal image patch is modeled as a linear combination of vectors cropped from the noisy image, and the model is fitted to the real image data by allowing a small perturbation in the TLS sense. A new technique to solve the TLS problem without the knowledge of the ideal image patch when the image is corrupted by signal-dependent noise is performed.

Denoising algorithms based on gradient dependent regularizers, such as nonlinear diffusion processes and total variation denoising, modify images towards piecewise

constant functions. Although edge sharpness and location is well preserved, important information, encoded in image features like textures or certain details, is often compromised in the process of denoising. The A-TV is a mechanism that better preserves fine scale features in such denoising processes (Gilboa, 2006). A basic pyramidal structure-texture decomposition of images is employed. A first level of this pyramid is used to isolate the noise and the relevant texture components in order to compute spatially varying constraints based on local variance measures. A variational formulation with a spatially varying fidelity term controls the extent of denoising over image regions. In other words, regions of the residual part with higher local variance than that of the noise are treated as textured regions where denoising is inhibited.

Wavelet-domain denoising is generally based on the assumption that the wavelet coefficients are statistically independent or jointly Gaussian. However, in several cases (e.g. image compression) non-Gaussian models for individual wavelet coefficients are required. Moreover, statistical dependencies between coefficients should be characterized in order to derive optimal signal processing algorithms. A framework for statistical signal processing based on wavelet-domain hidden Markov models (HMM's) that concisely models the statistical dependencies and non-Gaussian statistics encountered in real signals have been assumed (Crouse et al., 1998). The method involves an efficient expectation maximization algorithm for fitting the HMM's to observational signal data. This approach can be also very useful for reconstructing image affected by non-Gaussian noise.

The K-SVD is an image denoising algorithm for AWGN based on sparse and redundant representations over trained dictionaries (Elad and Aharon, 2006). Using the K-SVD algorithm, a dictionary that describes the image content effectively can be obtained. Two training options are considered: using the corrupted image itself or training on a corpus of high-quality image database. Since the K-SVD is limited in handling small image patches, its deployment is extended to arbitrary image sizes by defining a global image prior that forces sparsity over patches in every location in the image.

The BM3D performs an image collaborative denoising strategy based on an enhanced sparse representation in transform domain (Dabov et al., 2007). The

enhancement of the sparsity is achieved by grouping similar (e.g. blocks) into 3-D data arrays which are called “groups.” Collaborative filtering is realized using the three successive steps: 3-D transformation of 2-D image blocks into a group, shrinkage of the transform spectrum and inverse 3-D transformation. The result is a 3-D estimate that consists of the jointly filtered grouped image blocks. By attenuating the noise, the collaborative filtering reveals even the finest details shared by grouped blocks and, at the same time, it preserves the essential unique features of each individual block. The filtered blocks are then returned to their original positions. Because these blocks are overlapping, for each pixel, we obtain many different estimates which need to be combined. Aggregation is a particular averaging procedure which is exploited to take advantage of this redundancy. A significant improvement is obtained by a specially developed collaborative Wiener filtering. Although the BM3D algorithm is designed for AWGN, it has been also widely used for non-Gaussian noise.

A denoising algorithm (BM3Dc) for signal-dependent clipped noisy observations, (such as digital fluoroscopic images) has been performed (Foi, 2009). The approach involves a BM3D algorithm designed for AWGN and derive specific homomorphic transformations to stabilize the variance of the clipped observations, to compensate the bias due to the clipped distribution in the variance-stabilized domain and to compensate the estimation bias between the denoised clipped variables and the non-clipped true variables.

Signal-dependent methods require to estimate the noise variance for each image pixel value (see also paragraph 4.3). At this aim, noise variance estimation has been performed through a wavelet-domain analysis approach specifically intended for clipping Poisson noise (Foi et al., 2008). This approach has been then adapted for the gamma-corrected images.

For the other denoising methods a global estimate of noise variance which are meant to be valid for the whole image is required. Noise level has been estimated as average of the sample noise variance computed on different homogeneous image areas. Canny algorithm has been performed in order to exclude intensity variation associated with the signal from the estimation of noise variance (i.e. to exclude image edges from the areas assumed for noise estimation).

4.4.2 Simulated data

The performance comparison presented in this section has been performed by using a computed radiography (CR) image of a human chest. Image size was 2140 × 1760 pixels and gray scale ranged from 0 to 65535. Algorithms have been performed by MatLab R2009b (64-bit) on a 2.27-Ghz Intel Core i3 with 4.00-GB memory. Figure 4.7 displays the original CR image and the image corrupted with Poisson noise. The CR image was scaled and corrupted by Poisson noise in order to obtain a 13 dB SNR (signal-to-noise ratio). The performance of the denoising algorithms has been evaluated in terms of PSNR (peak signal-to-noise ratio). The SNR of the denoised image (SNR_f), the MSE (mean square error) between the original image and the denoised image and the computational time (T) have been also computed. The performance of the algorithms depends on various parameters that are chosen by the user while running the software. A different tuning of these parameters for a specific image may lead to different results. In our case the parameters were chosen in order to obtain the finest image restoration (to the detriment of the computational time). In this regard, it should be stressed that diagnosis of segmental instability by videofluoroscopy does not require hard real-time computation. Therefore, computational time has not been considered as critical for evaluation of denoising algorithm.

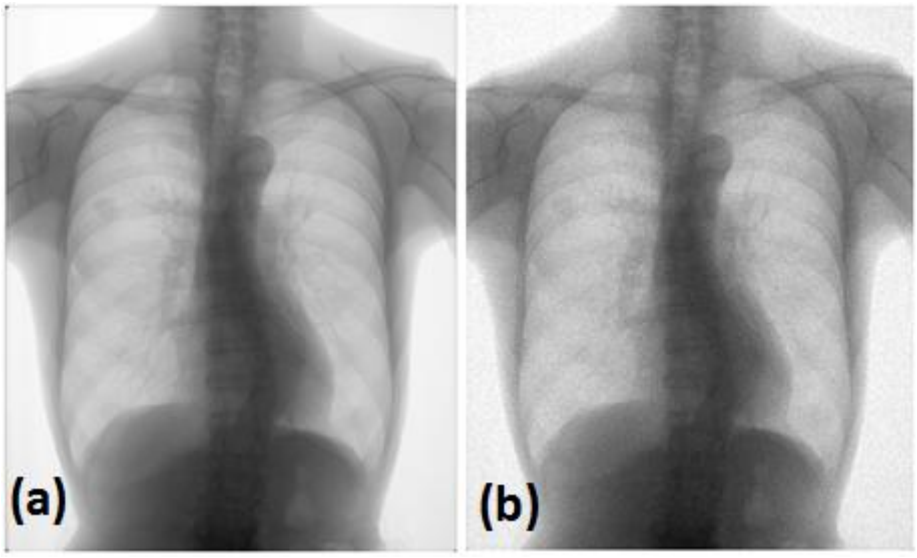

Figure 4.7. (a) The original test image; (b) The corresponding noisy image.

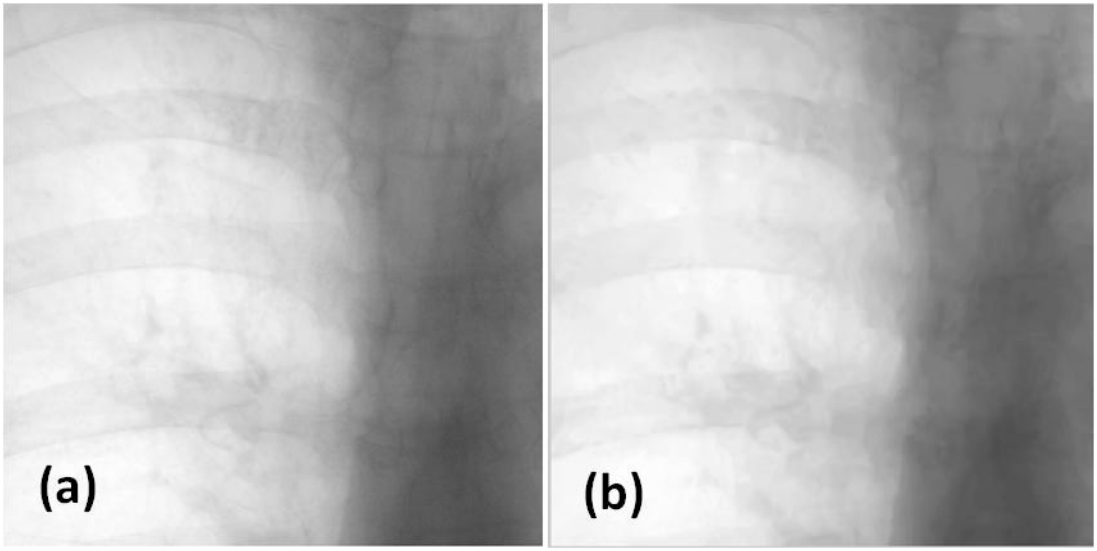

Figure 4.8. (a) A particular of the original test image; (b) The corresponding denoised image by BM3Dc filter.

Table 4.1. Poisson noise denoising – raw test image (SNR initial = 13 dB)

	PSNR [dB]	SNR_f [dB]	MSE	T [s]
AVS	41.19	25.96	4.95	10.19
TV	34.68	19.46	22.15	392.00
A-TV	39.24	24.02	7.75	2253.39
HMM's	38.55	23.32	9.16	18.72
K-SVD	38.3560	23.13	9.49	348.16
BM3D	41.11	25.89	5.03	8.16
BM3Dc	41.22	25.99	4.91	5.46

As shown in Table 4.1, on average, wavelet-based methods are resulted the most competitive. In particular, the BM3Dc filter presents the highest PSNR and SNR_f and simultaneously the shorter CPU time. Figure 4.8 shows the original CR image and the denoised image obtained by BM3Dc filtering. The AVS filter also offers an excellent image restoration against a very low computational complexity, while other denoising algorithms result slightly less performing. It is interesting to note that the filters specifically designed for signal-dependent noise provide a better image restoration with respect to the others designed for AWGN. This is consistent with the characterization of Poisson noise (see also paragraph 4.4).

The comparison has been repeated after applying a gamma-correction transformation to the noisy test image ($\gamma = 0.35$) (Figure 4.9). Results are shown in Table 4.2. In this case, denoising algorithms designed for AWGN appear to be more competitive. It might depend on the unsuitable noise model used from the other denoising algorithms with respect to the noise model change due to the gamma-correction transformation. It is not surprising that AWGN denoising algorithms perform better after applying gamma-correction. Indeed, gamma-correction inherently determines a reduction of noise variance associated with the brighter image pixels that are prevalent in the original test image.

Figure 4.9. Gamma-corrected test image.

Table 4.2. Poisson noise denoising – gamma-corrected test image (SNR initial = 13 dB)

	PSNR [dB]	SNR_y [dB]	MSE	T [s]
AVS	42.07	25.99	4.60	8.80
TV	44.79	24.07	44.79	248.66
A-TV	41.01	24.90	5.15	2210.15
HMM's	45.07	24.35	4.80	24.35
K-SVD	47.0645	26.35	1.28	73.86
BM3D	47.52	26.81	1.15	6.92
BM3Dc	39.57	18.86	7.18	5.30

4.4.3 Real data

In this section the algorithms under comparison have been applied to real spinal data from fluoroscopic images.

Although an accurate evaluation of denoising effectiveness is not achievable (i.e. an uncorrupted test image is not available), a more quantitative comparison of denoising algorithms has been proposed. The effectiveness of algorithms in reducing the noise mottle in fluoroscopic spinal image has been evaluated in terms of sample noise variance reduction on different homogeneous image areas between the noisy image and the output of the noise suppression algorithms (Figure 4.10). Canny algorithm has been performed in order to exclude image edges from the areas assumed for the estimation of noise variance. Image regions with different mean pixel intensity has been chosen and an average value of the noise variance reduction has been also computed. Edge blurring has been calculated by measuring the percentage reduction of the slope of image edge profiles in the gradient direction and also in its opposing direction between raw and filtered images (Wang et al., 2008) (Figure 4.10).

Results of comparison are summarized in Table 4.3. They are about consistent with those obtained from simulated data corrupted by Poisson noise except for the BM3Dc filter. In particular, AVS filters show a good trade-off between noise variance reduction and edge preservation with respect other denoising algorithms, simultaneously providing a less computation complexity.

Table 4.3. Poisson noise denoising – real fluoroscopic data

		AVD	TLS*	A-TV	HMM's*	KSVD	BM3D	BM3Dc
noise variance reduction [%]	dark	58.8941	36.8829	97.9552	17.2278	70.1877	75.2763	25.8156
	medium	68.9572	31.1680	78.4469	15.1050	51.1217	49.6965	26.0262
	bright	67.1158	60.6175	97.1066	15.8874	69.0566	67.7134	34.9454
	mean value	**64.9890**	**42.8895**	**91.1696**	**16.0734**	**63.4553**	**64.2287**	**28.9281**
edge slope reduction [%]	horizontal	10.5633	10.2687	22.0500	5.9751	14.6416	5.5556	5.5556
	vertical	2.1849	14.2500	26.2160	6.5782	14.0820	21.8750	12.5000
	mean value	**6.3741**	**12.2594**	**24.1050**	**6.2767**	**14.3618**	**13.7153**	**9.0278**
time [s]		8.379351	3403.480372	25.801673	79.742648	202.021826	15.554376	11.437380

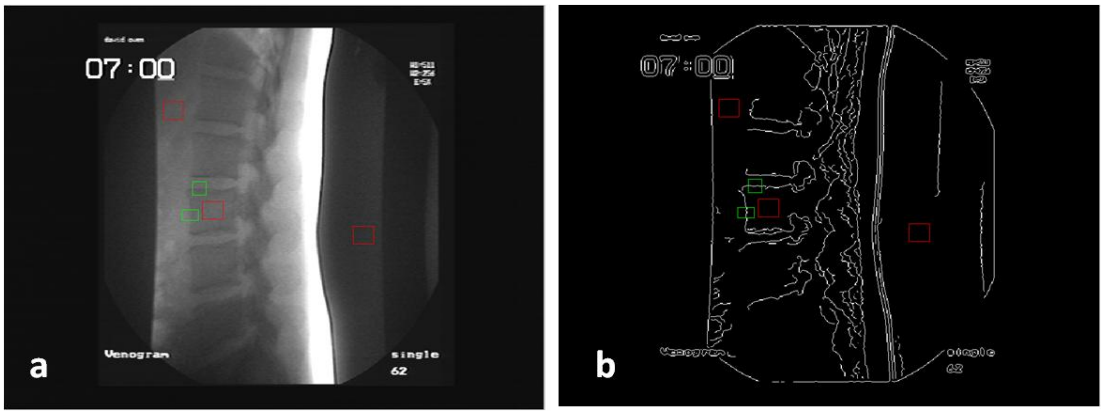

Figure 4. 10. (a) Original fluoroscopic image with an example of the areas selected for the sample noise variance and the edge blurring measurement; (b) The output of the Canny algorithm applied to the fluoroscopic image.

4.5 Summary

Image denoising is necessary to recover anatomical details that may be hidden in the fluoroscopic data and, consequently, to provide an accurate kinematic estimation. This is particularly true when edge detection algorithm are used for the estimation procedure. Various image restoration and enhancement methods have been proposed for removing degradations due to the noise. The effectiveness of these image restoration algorithms mainly depends on the validity of the image noise model. An extensive investigation of fluoroscopic noise has been proposed. The noise model changes in the case of image non-linear transformation (e.g. white compression) have been also investigated. A comparison of denoising algorithms specifically designed for both the signal-dependent noise and AWGN has been provided. Signal-dependent denoising algorithms are resulted to be, on average, more competitive. This is consistent with the characterization of the fluoroscopic noise. With respect to real noisy fluoroscopic data, adaptive averaging spatial (AVS) filters show a great balance between noise removal and low edge blurring. In the light of this, a more elaborated AVS denoising algorithm has been performed for noise reduction in the fluoroscopic spinal images in order to improve the accuracy of the estimation procedure presented in Chapter V and VI.

Chapter 5

Intervertebral kinematic estimation by digitized videofluoroscopy

[We] as people don't like uncertainty, don't like knowing that there's something we can't comprehend. And if we can't fit something into an existing pattern, then by golly we'll come up with one
William Gibson

Estimation of rigid motion between two distinct poses is a common technique for assessing joint function. For instance, by extracting the position of vertebrae from two successive radiological images it is possible to estimate the intervertebral motion that is occurred. In clinical setting very few radiographic measurements are generally performed in order to limit the X-ray dosage to the patient. As a consequence, no information are available about the intervertebral kinematics during the entire spinal motion. On the contrary, the use of a fluoroscopic device can offer a continuous screening during the full spinal motion with an acceptable X-ray dose. Fluoroscopic measurement of intervertebral kinematics is, however, confined to the planar motion and required the assumption of no out-of-plane coupled motion. Although this hypothesis can be neglected in flexion-extension motion (mainly due to the anatomic symmetry), it is no longer valid in lateral bending (Panjabi et al., 1992a; Van Mameren et al., 1992, Breen, 1991; Bifulco et al., 2002; Bifulco et al., 2010). In addition, a hypothesis of rigidity must be held for vertebrae (this is consistent with

the negligible deformation of vertebral bodies caused by the forces acting on the vertebral column during motion (Frankel and Burstein, 1974)).

Estimation of kinematic parameters describing the functionality of motion segment (i.e. intervertebral angle and position) by videofluoroscopy requires the recognition of vertebral bodies in each frame of the fluoroscopic sequence. A variety of different features or landmarks (e.g. vertebral body edges or corners, spinal processes, etc.) and measurement techniques have been proposed for the vertebrae recognition. Manual identification of anatomical landmarks is widely employed in clinical setting mainly due to its simplicity. This operation results, however, in a subjective, tedious and often insufficiently accurate procedure. Indeed, large errors in the computation of kinematic parameters may result from relatively small errors in the identification of spatial landmark coordinates. More recently, different automated approaches have been proposed in order to limit the reliance on the operator and to improve the accuracy of intervertebral kinematic estimation. In this Chapter, after a brief description of the main vertebrae recognition approaches (paragraph 5.1), a recently proposed automated method based on cross-correlation template matching for vertebrae recognition in fluoroscopic image sequences is presented in paragraph 5.2, 5.3 and 5.4. A few considerations about the clinical effectiveness of the proposed method are reported in paragraph 5.5.

5.1 Vertebrae recognition algorithms

Manual landmarking is a very tedious and laborious procedure for vertebrae recognition. Furthermore, it can be error prone (Panjabi, 1979; Panjabi, 1992a). For these reasons, there have been several previous attempts to automate landmarking procedure. Template-based approach has been generally considered to be more reliable with respect to geometric feature-based matching approaches mainly due to its robustness to image noise. This aspect is critical in determining the location of vertebral bodies as fluoroscopic images are generally affected by severe noise. In addition, by using template matching the geometrical properties of the vertebra of interest are preserved and no vertebral shape model is required (i.e. the vertebral template is selected from an image of the video sequence). As a result, variations in

the vertebral shape between individuals and between the segmental levels in one individual can be accounted for. Template-based approach suffers, however, from some disadvantages. Template matching typically needs more computationally time; if there has been any out-of-plane motion, the vertebral shape will be distorted and an exact match will be never found; since soft tissue does not move rigidly with the vertebrae, the gray level contribution from the soft tissue will change frame by frame (reducing the matching with the vertebral template).

At first, Simonis et al. (1993) developed a parallel computing technique using template matching for planar kinematic parameter calculation. Muggleton and Allen (1997) performed template matching by using an annular template which contains only the margins of the vertebra. Bifulco et al. (2001) also applied a template matching algorithm based on cross-correlation. In this case the vertebral template is utilized for a preliminary estimation of the location of the vertebra, while four small corner templates are utilized to precisely locate the vertebral landmarks from which the vertebral position can be estimated and the kinematics computed. A procedure for the restoration of vertebral rigidity based on the evaluation of the maintenance of the mutual distances between corners is also performed. These methods offer a good accuracy in recognizing vertebrae in a fluoroscopic image sequence of a calibration model, but their usability *in vivo* human sequences is not yet proved.

Zheng et al. (2004) proposed an innovative method based on the generalized Hough transform with Fourier descriptors to represent the vertebral shape. However, this approach, as others based on vertebral outline descriptors (for instance, McCane et al., 2006), strongly suffers from the image noise, especially for *in vivo* fluoroscopic images where the noise level can be comparable to the gray-level profile of vertebral edges.

Wong et al. (2004) developed a tracking algorithm using a Kalman filter which requires analytical, linear and Gaussian trajectory and measurement models. Its applicability is, however, limited as measurements from images are usually non-linear and it is difficult to obtain an analytical solution for the model in most cases.

A possible solution to tracking vertebrae is formulating it within a Bayesian framework. Lam et al. (2009) have proposed a tracking algorithm for vertebrae in a Bayesian paradigm. They set up a dynamic Bayesian network (DBN) based on prior

knowledge of anatomical configurations with a particle filter at each DBN node to track the vertebrae from digital fluoroscopic sequences. This method shows a high accuracy against known values of intervertebral angle of a calibration model (average error within about 1°) and in tracking vertebrae *in vivo* fluoroscopic sequences with respect to manual landmarking. However, *in vivo* results are presented only for absolute vertebral angle and position and not for intervertebral kinematics. In this regard, it is interesting to note that intervertebral data are obtained by difference between close values. Therefore, their relative error is considerably greater with respect to the error of absolute vertebral measures.

Recently, Cerciello et al. (2011b) have proposed a new, automated method based on cross-correlation template matching of the contour of vertebral bodies for estimating intervertebral kinematics during flexion-extension spinal motion in sagittal plane (see section 5.2). Accuracy of the method has been tested using images of a calibration model. The method has been also compared to manual landmarking (Kondracki, 2001) and other automated methods (Bifulco et al., 2001; Muggleton and Allen, 1997; Zheng et al., 2004) and is resulted to provide a better representation of the evolution over time of *in vivo* intervertebral data in terms of lower noise content (i.e. measurement error).

5.2 Advanced template matching for intervertebral kinematic estimation

---

A method based on cross-correlation template matching for automatic recognition of vertebrae in fluoroscopic sequences of lumbar flexion-extension spine motion in the sagittal plane is presented (see also Cerciello et al., 2011b). The method involves a strong enhancement of the outline of vertebrae by estimating gradient images. In order to achieve a reliable estimate of the gradient images severe image denoising is also applied

In the paragraph 5.2.1 particular attention is paid to fluoroscopic noise suppression and to edge-preserving filter design. The cross-correlation index adopted for template matching and the vertebrae recognition procedure are then described in the paragraphs 5.2.2 and 5.2.3, respectively.

5.2.1 Fluoroscopic image noise filtering

Image template matching can perform much more effectively when the contours of the object are matched (Argyriou and Vlachos, 2003). By using gradient images a high cross-correlation will be produced when the template is in the correct position but will be poor elsewhere: this will significantly increase accuracy of the object recognition. A simple central difference filter can be employed to estimate the gradient of a raw image along both horizontal and vertical directions. Gradient operators are, however, very sensitive to noise. Therefore, emphasis should be devoted to the suppression of image noise before the gradient estimation.

As discussed in Chapter IV, fluoroscopic images exhibit severe noise that should be reduced while preserving diagnostic structures in order to avoid the failure of the gradient template matching algorithm. Quantum noise is by far the dominating noise in X-ray fluoroscopy, while other types of noise can be neglected (for instance, Chan et al., 2003; Hensel et al., 2007). Image quantum noise is generally modeled as Poisson-distributed. Although Poisson noise does not exactly fit the general concept of additive or multiplicative noise, it can be well-approximated to a local zero-mean additive Gaussian noise with signal-dependent variance (Aach and Kunz, 1996; Hensel et al., 2007).

Various methods have been proposed for reducing noise in low-dose X-ray images. The simpler methods are based on a linear filter that is composed of a temporal and/or a spatial low-pass filter. Although linear low-pass filters can strongly reduce noise, they also reduce the signal components (e.g. edge and structures) and, thus, they are not appropriate for object recognition (usually based on edge detection). For overcoming the limitations of linear filters, several improvements have been proposed, including temporal filters combined with motion detection, edge-preserving adaptive filters, non-linear diffusion or multi-resolution filters (for instance, Cerciello et al., 2011b; Crouse et al., 1998; Dabov et al., 2007; Elad and Aharon, 2006; Foi, 2009; Gilboa, 2006; Hirakawa and Parks, 2006;)

In particular, in Chapter IV it has been suggested that spatial adaptive averaging filters, specifically designed for signal-dependent noise, can provide a good trade-off between noise reduction and edge preservation in fluoroscopic spinal images. In practice, a filter that performs a local conditional average, by considering the local

noise variance, combined with a novel approach to preserve edges has been adopted for the noise reduction of the spinal fluoroscopic images (Cerciello et al., 2011b).

The filter performs the average of the only neighbouring pixels that differ less than $\pm\tau$ (filter threshold) from the gray level of the central pixel of the filter mask. The threshold τ is set to two times the estimated standard deviation ($2\sigma_{gl}$) of the noise associated with the local gray level, but an upper limit for τ has been applied corresponding to the average gray level transition (Δ_s) between the vertebrae and surrounding soft tissues (the latter quantity must be heuristically measured for each fluoroscopic sequence). If static (i.e. when scene is motionless) images are available, they can be used for estimating the sample noise variance as a function of the mean pixel gray level (i.e. σ_{gl}^2). More specifically, the noise sample variance at each image pixel has been calculated from all possible differences between the available static images and associated with the mean of the raw pixel gray levels at that pixel. Once estimated the local Skellam moments, the local variance of the image Poisson noise has been easily computed (see Appendix C). It is interesting to note that, since the Skellam parameters are extracted from all the possible differences between static frames, estimation of quantum-noise parameters by difference can be effectively performed also when few statics frames are available. In our case, about 10 static frames were acquired during patient's apnea at the beginning of the clinical procedure. Furthermore, the sampling rate was fairly below the 25 frames per second that was consistent to the hypothesis of not correlation of noise components frame by frame (required for the Skellam modeling, see Appendix C).

The formula of the emplyed filter is:

$$g'(x,y) = \frac{1}{(\sum_k \sum_l u(k,l))} \sum_{k=x-w}^{x+w} \sum_{l=y-w}^{y+w} [g(k,l) \cdot a(k,l)]$$

$$a(k,l) = \begin{cases} 0\,, & |g(k,l)| \geq |\tau| \\ 1\,, & |g(k,l)| < |\tau| \end{cases} \quad \text{where } \tau = \begin{cases} |2\sigma_{gl}| & \text{if } |2\sigma_{gl}| < |\Delta_s|/2 \\ |\Delta_s|/2 & \text{if } |2\sigma_{gl}| \geq |\Delta_s|/2 \end{cases} \tag{27}$$

where g'(x,y) is the filtered pixel; g(k,l) are the pixels of the raw image around the coordinates (x,y); w is the spatial hemi-dimension of the filter; σ_{gl} is the noise standard deviation corresponding to the gray level at the position (x,y); Δ_S is the

average gray-level transition at the vertebra edges. The hemi-dimension of the filter is fixed to about 2.5 mm (corresponding to an odd number of pixels depending on the pixel size) which is much lower than the average lumbar disc height (about 12 mm). With reference to an entire real fluoroscopic sequence of lumbar spine (for image characteristics, see paragraph 4.4.3) the spatial averaging operation, processed such as in Eq. (27), is resulted to be computed on about 70% of the filter mask (mean value computed on all image processed) with a mean decrease of the noise standard deviation of about nine times. The related edge blurring, calculated by measuring the percentage reduction of the average slope of the edges in the gradient direction and also in its opposing direction between raw and filtered images (Wang et al., 2008), is resulted of about 15%. Figure 5.1ab represents an original fluoroscopic image of lumbar spine beside the output of the noise suppression filter; in order to appreciate the noise suppression and edge preservation it is also shown a profile of the gray levels along a vertical image segment (Figure 5.1c) depicted in white on both images. Figure 5.2a shows the result obtained processing the fluoroscopic image of Figure 5.1b with the central difference filter (only the magnitude of the gradient image was displayed). For sake of comparison, Figure 5.2b presents the magnitude of the gradient image obtained by directly applying the Sobel filter to the raw (unprocessed) fluoroscopic image of Figure 5.1a.

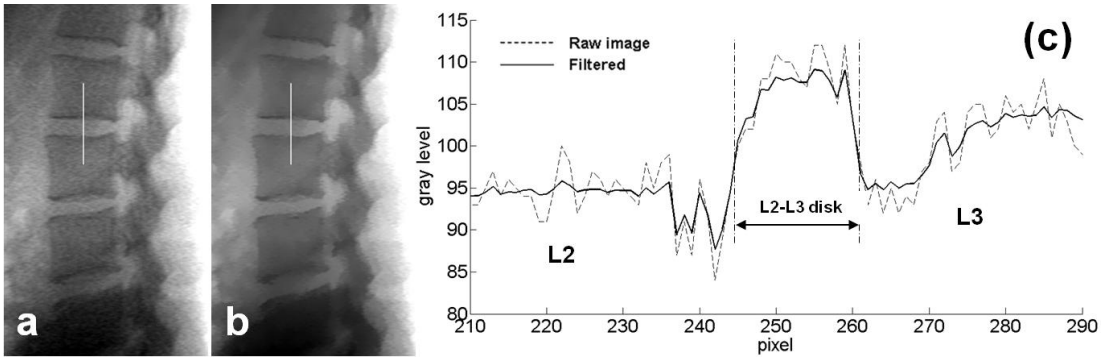

Figure 5.1. (a) Original fluoroscopic image; (b) The output of the noise suppression filter; (c) Gray level profile along the vertical image segment (depicted in white) before and after applying the noise suppression filter (from Cerciello et al., 2011b).

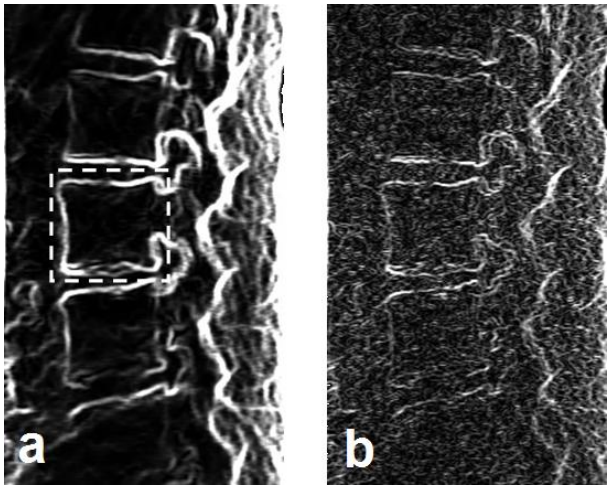

Figure 5.2. (a) Magnitude of the gradient image with the current method, the template relative to the vertebra L3 is also shown (dashed white line); (b) Estimation of the image gradient by using a common Sobel operator (from Cerciello et al., 2011b).

5.2.2 Cross-correlation index

Cross-correlation has been adopted as measure of similarity for template matching. Although cross-correlation is computationally more expensive and more sensitive to imaging scale, large rotation and perspective distortions with respect to other criteria, it is much more robust to image noise. In addition, cross-correlation can be formulated in order to be insensitive to both contrast and brightness variations: the effect of local image contrast can be removed by using a normalized expression of cross-correlation, while the variations of brightness can be compensated using a mean-centered cross-correlation (Lewis, 1995). A suitable expression of the zero-mean normalized cross-correlation index has been considered, given by (Cerciello et al., 2001b):

$$\mathrm{NCC}(x,y) = \frac{1}{2}\frac{\sum_{i=-I/2}^{I/2}\sum_{j=-J/2}^{J/2} G_x(x+i,y+j)\cdot T_x(i,j)}{\sqrt{\sum_{i=-I/2}^{I/2}\sum_{j=-J/2}^{J/2} G_x^2(x+i,y+j)}\cdot\sqrt{\sum_{i=I/2}^{I/2}\sum_{j=I/2}^{J/2} T_x^2(i,j)}} + \frac{1}{2}\frac{\sum_{i=-I/2}^{I/2}\sum_{j=-J/2}^{J/2} G_y(x+i,y+j)\cdot T_y(i,j)}{\sqrt{\sum_{i=-I/2}^{I/2}\sum_{j=-J/2}^{J/2} G_y^2(x+i,y+j)}\cdot\sqrt{\sum_{i=-I/2}^{I/2}\sum_{j=-J/2}^{J/2} T_y^2(i,j)}} \qquad (28)$$

where G_x and G_y are the components of the gradient vector in the horizontal and vertical directions relative to the observed fluoroscopic image; T_x and T_y are the components of the gradient vector relative to the template; I and J are the dimensions of the template (in pixels). It is worth noting that this expression for the cross-

correlation index not only takes into account the product of the gradient magnitudes, but also performs a scalar product between the gradient vectors:

$$|G_x| \cdot |T_x| + |G_y| \cdot |T_y| = |G'||T'| \cos\theta \tag{29}$$

where cos θ is the angle between the two vectors. This results in a more accurate match between image and template (Figure 5.3).

In order to reduce the computational time required for the image processing, the cross-correlation index can be carried out as a multiplication in the frequency domain and the frames of the video sequence can be cropped such that only areas that contain information about the vertebrae are kept.

5.2.3 Vertebrae recognition procedure

The recognition procedure has been designed to minimize the reliance on the operator. Four landmarks on the corners of each vertebral body of interest are required to be selected in a single frame of the sequence, generally in the first frame that is motionless (i.e. no motion blurring)[3]. After noise suppression, the gradient images are computed from each raw image of the fluoroscopic sequence and the gradient vertebral template, which includes the entire vertebral body and its close surroundings, is automatically generated from the selected landmark coordinates.

[3] It must be noted that in some real cases, such as a severe disc degeneration, it is not always possible to select a template which entirely surrounds the vertebral body without including other parts of adjacent vertebrae. The inclusion of other anatomical structures, which are not rigidly fixed to the vertebra of interest, would lead to a decrease in vertebra tracking capability. This problem could be, however, solved by designing an opportune shape of the template, instead of a rectangular one, which includes only the unambiguous vertebra edges.

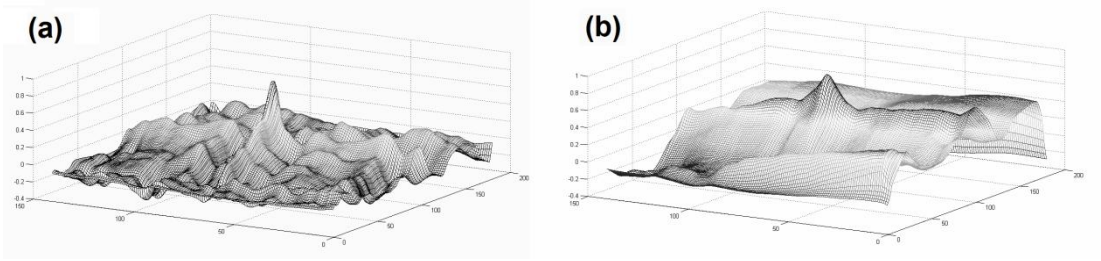

Figure 5.3. (a) Normalized cross correlation map obtained using a fluoroscopic gradient-image; (b) The correspondent map obtained using the unprocessed image.

The location of the selected vertebra is carried out by searching for the coordinates of the maximum of the cross-correlation index in each gradient image. Since the template and observed images are both spatially translated and rotated, the cross-correlation function maximum is searched in the three-parameter space: x-position, y-position and rotation angle. The cross-correlation index is computed rotating the main template progressively with 1° increments. It is then repeatedly computed around the cross-correlation function maximum while progressively rotating the template with 0.1° increments. The coordinates of the global maximum of the cross-correlation estimate the vertebra position, while the angle corresponding to that maximum is held as the vertebra angle of rotation.

Since pixel grid structure results from the spatial sampling at the image acquisition stage, the accuracy of vertebra location depends on the image acquisition system. To provide a location that is more accurate than the pixel dimension, sub-pixel interpolation by least-squares fitting of cubic polynomial is performed in the neighbourhood of the cross-correlation maximum.

At the end of the vertebra recognition procedure, the x- and y-position and the angles of rotation of the selected vertebra are available for all the frames of the fluoroscopic sequence. These three parameters over time completely describe the planar, rigid motion of the vertebra (i.e. three degrees of freedom). The procedure must be repeated for different vertebrae. For each pair of adjacent vertebrae (i.e. motion segment) the relative motion of the upper vertebra is then estimated with respect to the lower which is considered fixed (i.e. intervertebral kinematics).

5.3 Method validation

Fluoroscopic images of a calibration model, already employed in previous studies (Bifulco et al., 2001; Breen, 1991; Lam et al., 2009; Muggleton and Allen, 1997; Simonis, 1994, Zheng et al., 2004), have been used to assess the accuracy of the estimation method (Figure 5.4). The model consists of two human lumbar vertebrae (L3 and L4) linked, at the disc level, by means of a universal joint (Figure 5.5). The joint allows the vertebra L3 to rotate with known preset angles with respect to L4 which is fixed to a support. The fluoroscopic images were obtained by progressively rotating L3 in the sagittal plane with respect to L4 in steps of 5°. The size of digital image was 512 by 512 pixels, while image intensity was quantized to 256 gray levels. Pixel size was about 0.25 mm by 0.25 mm.

Table 5.1 shows the results obtained by processing the fluoroscopic images of the calibration model. Intervertebral angles has been compared to the preset angles and also to previous results reported in literature obtained by other automated methods from the same image set (Bifulco et al., 2001; Muggleton and Allen, 1997; Zheng et al., 2004). To complete the assessment of the intervertebral kinematics, the coordinates of the intervertebral center of rotation has been computed for each rotation step, as suggested in McCane at al. (2005). They has been compared to the coordinates of the center of the universal joint, which is the true pivot point for the intervertebral motion. Table 5.2 shows the expected coordinates of the center of intervertebral rotation together with the computed coordinates; the distances between the center of the universal joint and the estimated intervertebral centers of rotation are also reported. Average error achieved for the intervertebral angle is of the order of 0.4 degrees and approximately 2 mm for the intervertebral center of rotation. Figure 5.6a shows a fluoroscopic image of the calibration model and the location of the computed intervertebral centers of rotation (white crosses) superimposed on an enlargement of the image (Figure 5.6b); the true center of the joint is represented as a white dot.

Table 5.1. Intervertebral angles of the calibration model (all values are expressed in degree)

Intervertebral (L3-L4) angles				
Preset angle	**Computed angle**	**Muggleton et al., 1997**	**Bifulco et al., 2011**	**Zheng et al., 2004**
5	4.9	4.5	5.1	5
10	10.5	10.1	10.1	10
15	15.5	15.6	15.8	16
20	20.8	20.6	20.8	21

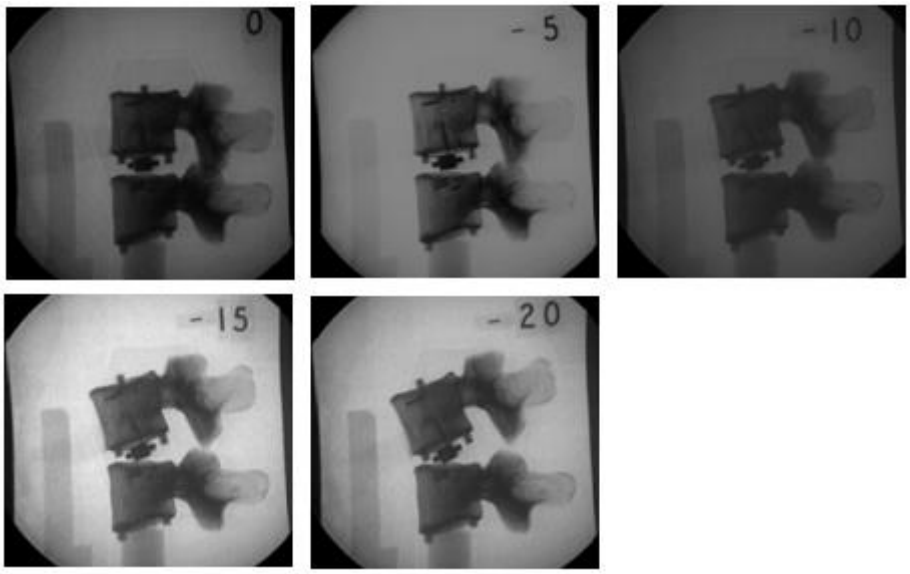

Figure 5.4. Fluoroscopic image sequence of the calibration model employed for the method validation (from Bifulco et al. 2001).

Figure 5.5. The calibration model (from Breen et al., 2006).

Table 5.2. Intervertebral centers of rotation of the calibration model

Estimated Intervertebral (L3-L4) centers of rotation				
Angle step (degree)	**label in Fig. 5.6**	**X-coord. (pixel)**	**Y-coord. (pixel)**	**Distance error (mm)**
0 ÷ 5	(a)	199.3	237.8	2.2
5 ÷ 10	(b)	192.9	226.6	1.6
10 ÷ 15	(c)	193.3	234.0	1.9
15 ÷ 20	(d)	187.8	229.6	2.8
Expected (true location, pixel)		199	229	

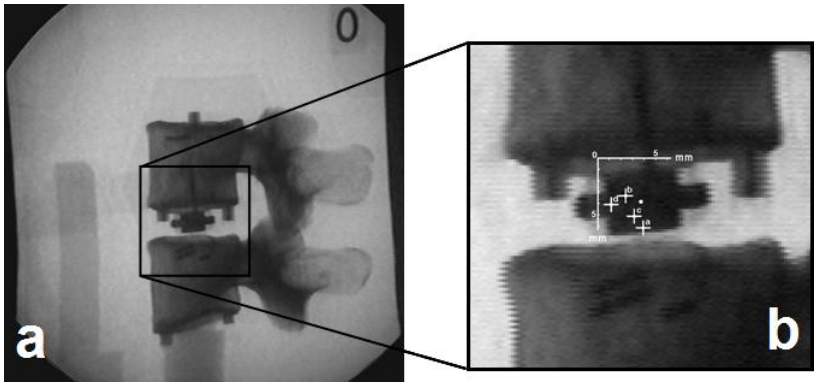

Figure 5.6. (a) Fluoroscopic image of the calibration model; (b) An enlargement of the universal joint with the estimated intervertebral centres of rotation superimposed (from Cerciello et al., 2011b).

5.4 Case study 1: *in vivo* fluoroscopic sequences

Five fluoroscopic image sequences of lumbar spine of healthy subjects[4] (Figure 5.7), have been processed in order to assess the described method with respect to manual landmarking and other automated approaches.

During the image acquisition the subjects lay on their side and were secured to a motorized table (Breen et al., 2006). The passive motion table had a lower section that could execute a smooth arc from the neutral position to 40° left, then to 40° right and back to neutral in one motion. The X-ray parameters were set to 73 kV and 2mA and the duration of the subject's movement took no more than 24s. Dosimeters measured about 0.9 Gycm^2. Images were captured from fluoroscope at a rate of 5

[4] These sequences have been already used in previous studies of Kondracki, 2001 and Zheng et al., 2004.

frames per second. Pixel size was 0.43mm by 0.43mm and images were digitized with 256 gray levels.

The comparison between the described method, manual landmarking and other examined automated methods is reported in paragraph 5.4.1. The clinical feasibility of the proposed method for the diagnosis of intervertebral instability is discussed in paragraph 5.4.2.

5.4.1 Data comparison

The vertebrae recognition procedure has been performed and results (i.e. estimated intervertebral angle and position) has been compared to the results obtained by other methods from the same images. The following methods has been compared: manual selection (Kondracki, 2001), template matching by simple cross-correlation (as that presented by (Muggleton and Allen, 1997)), multiple template matching (Bifulco et al., 2001), generalized Hough transform (Zheng et al., 2004) and the current method (gradient cross-correlation). The comparison between the different methods has been performed in terms of evaluation of the noise content (i.e. measurement error) in the resulting intervertebral data.

Intervertebral angles and positions obtained by videofluoroscopy can be considered as a superposition of the sampled true kinematic signal (i.e. intervertebral motion) and noise (i.e. measurement error). Since intervertebral motion can be only gradual and smooth (also due to viscoelastic properties of disc and other soft tissues, which provide a damping effect (Niosi and Oxland, 2004)), the true kinematic signal is band-limited (Cerciello et al., 2011b). On the contrary, measurement error depends on several factors (e.g. imperfections of algorithms, computation approximation, etc.) and can be considered as additive and white (i.e. uncorrelated, band-unlimited) (Challis, 1995; Cholewicki et al., 1991). Therefore, the lower frequency part of the estimated signals is mainly associated with motion, while the remaining (high-frequency content) with noise. Noise content can be significantly reduced by low-pass filtering and the residuals of the filtering operation (high frequency content) can be assumed indicative of the level of noise (i.e. measurement error) committed by each method.

Figure 5.7. Fluoroscopic images of lumbar spine.

By considering the dynamics of motion of the motorized table, which took a full course of lumbar flexion-extension in about 20 seconds, the spectral content of motion can be considered to be fairly included in a band of 0.14 Hz (low-pass Butterworth filter cut-off frequency) (for instance, Figure 5.8). The Ljung–Box whiteness test has been performed (with a significance level of 0.05) for all the residuals to ensure that they are uncorrelated and, hence, representative of random noise and not of motion. For each estimation method the root mean square (RMS) value of the residuals has been the calculated; this provides a concise index of the amount of noise. Table 5.3 summarizes and compares the RMS values of the residuals corresponding to the different estimation methods. As an example, for one of the sequences (subject #4), results obtained by the analysis of noise level in the *in vivo* intervertebral data are shown in Figure 5.9.

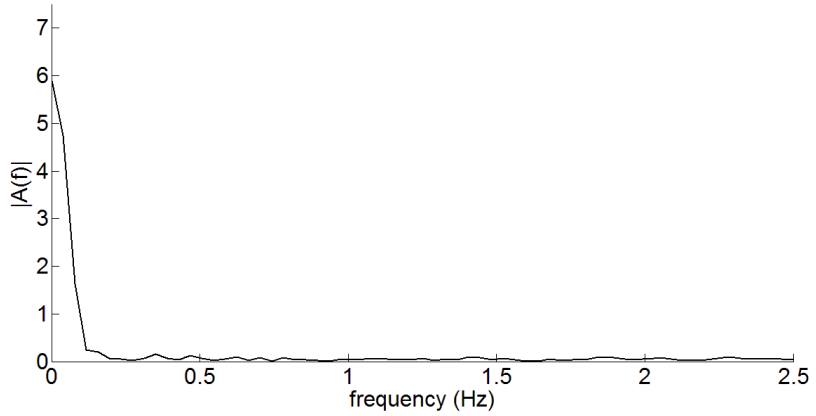

Figure 5.8. Spectral content (Fourier Transform) of the intervertebral angle signal (experimental raw data).

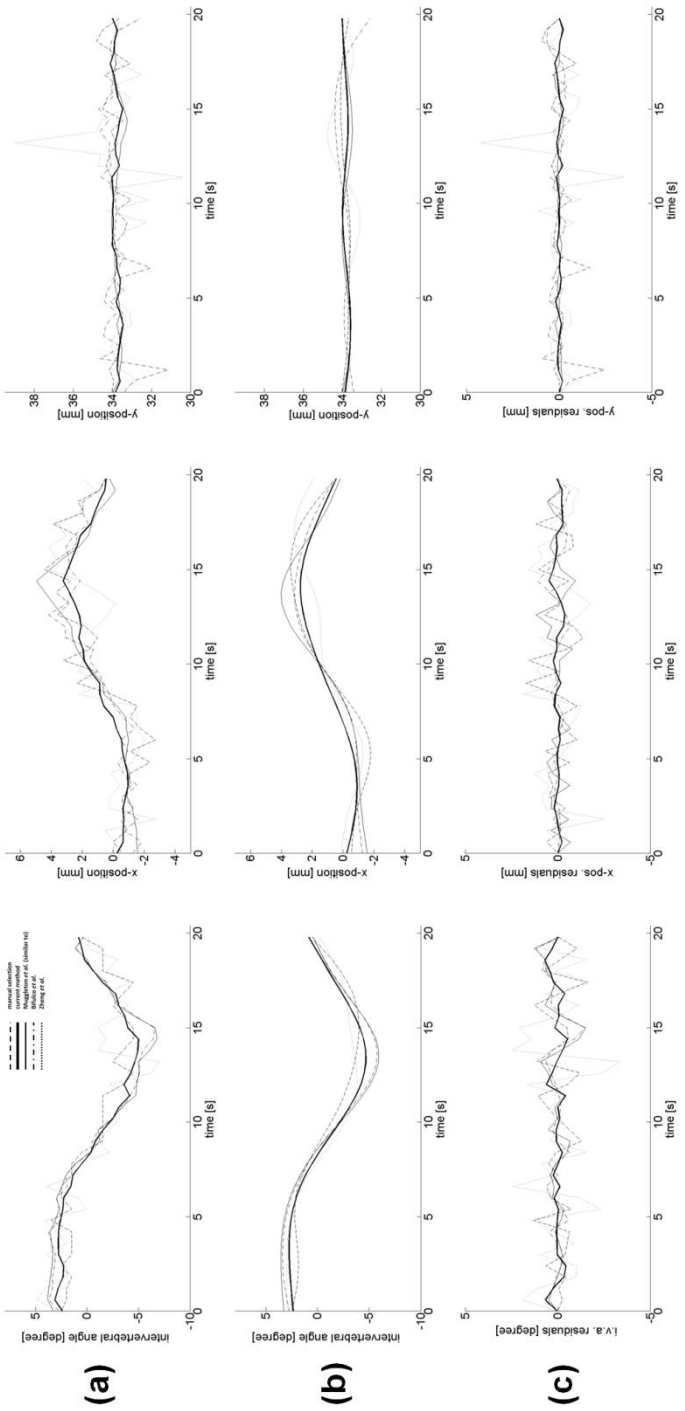

Figure 5.9. (a, at the top) Kinematic signals estimated with the different methods (subject #4); (b, at the middle) Corresponding low-passed kinematic signals; (c, at the bottom) Residuals of the low-pass operation (i.e. measurement error). Manual data: dashed lines; current results: continuous bold lines; Muggleton et al. (similar to): continuous lines; Bifulco et al. data: dash-dotted lines; Zheng *et al.* data: dotted lines (from Cerciello et al., 2011b).

Table 5.3. Root mean square (RMS) values of the residuals corresponding to the different estimation method

RMS values of residuals (L2-L3 intervertebral angles, x- and y-coordinates)					
	Current method	**Manual selection**	**Muggleton et al., 1997 (similar to)**	**Bifulco et al., 2001**	**Zheng et al., 2004**
Angle (degree)	0.30	0.71	0.74	0.51	1.40
X-coord. (mm)	0.18	0.73	0.54	0.46	0.98
Y-coord. (mm)	0.11	0.38	0.51	0.62	1.09

Since manual identification of vertebrae is still the most employed clinical technique, the current kinematic data have been carefully compared to previous data obtained from the same images through a manual selection of each vertebra carried out with great care and attention by an experienced clinician (Kondracki, 2001). In order to test the similarity between the two methods (manual selection and current method) the root mean square (RMS) differences between the two entire datasets (absolute and relative kinematic data) have been computed. For the L2 absolute angles the RMS difference is 0.97 degrees and for L2 trajectory the RMS difference is 0.78 mm. For the L3 vertebra the results are 1.05 degrees and 0.72 mm, respectively. For the intervertebral angles the RMS difference is 1.3 degrees and for the intervertebral trajectory the RMS difference is 0.9 mm. Figure 5.10 shows the distribution of the differences between the datasets of the L2-L33 intervertebral angles: the mean of this distribution is 0.13 degrees and the SD is 1.29 degrees. Figure 5.11 shows the distribution of the differences between the datasets of the x-coordinate (Figure 5.11a) and y-coordinate (Figure 5.11b) of the L23 intervertebral trajectories. The distribution of the differences between the x-coordinates has a mean value of -0.25 mm and an SD of 1.0 mm. The distribution of the differences between the y-coordinates has a mean value of -0.01 mm and an SD of 0.49 mm. By using Lilliefors test, the distribution of the differences resulted to be consistent with a normal distribution (all p-values were greater than 0.1 at significance level of 0.05).

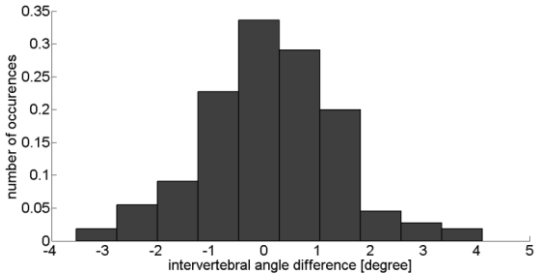

Figure 5.10. Distribution of the difference between datasets of the L2-L3 intervertebral angles (from Cerciello et al., 2011b).

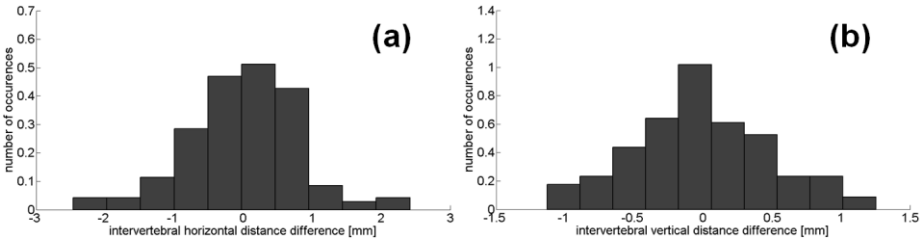

Figure 5.11. Distribution of the difference between datasets of the x-coordinate (a) and of the y-coordinate (b) of the L2-L3 intervertebral trajectories (from Cerciello et al., 2011b).

As an example, Fig. 5.12 shows the computed vertebral angle of L2 and L3 against time as obtained using the two different methods. From the figure it is possible to appreciate the progressive motion impressed by the motorized table.

Figure 5.13 represents the L2-L3 segment of the subject #1 and the intervertebral kinematic parameters estimated by manual selection and the current method. The graph representing the L2-L3 intervertebral angles against time (Figure 5.13c) is much more significant than that represented in Figure 5.12 to appreciate the current method accuracy; being intervertebral angle obtained by difference, it is affected by a greater measurement error due to the propagation of errors. The enhanced smoothness of the time-evolution of the intervertebral angles obtained by the current method with respect to those obtained using manual selection (that appears more alternating) is evident. This is also particularly clear for the intervertebral trajectory data (Figure 5.13b); however, it is worth noting that the trajectory is confined within 1-2 mm in the y-dimension (inferior-superior direction) and within 6-7 mm in the x-dimension (anterior-posterior direction). Figure 5.14 and 5.15 show the L2-L3 intervertebral kinematics computed for the other four subjects (#2, #3, #4, #5).

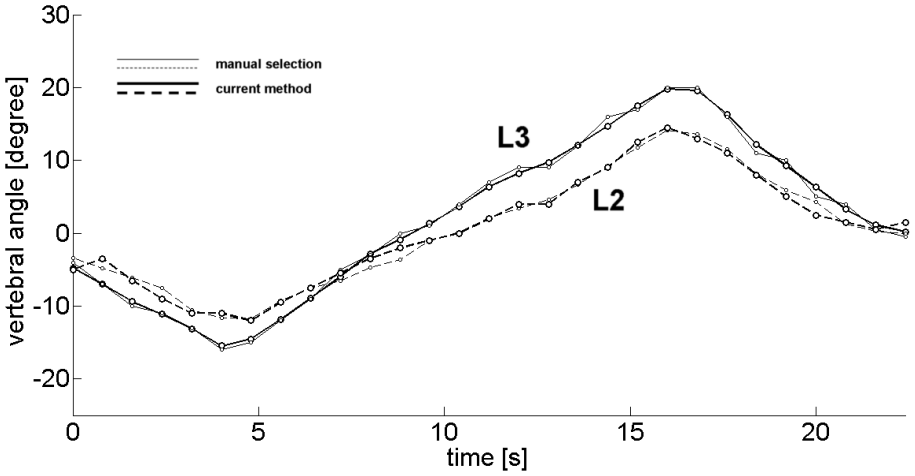

Figure 5.12. L2 and L3 vertebral angle plotted against time (subject #1). Positive angles correspond to flexion while negative angles to extension. L3 manual selection: continuous thinner lines; L2 manual selection: dashed thinner lines; L3 current method: continuous bold line; L2 current method: dashed bold lines (Cerciello et al., 2011b).

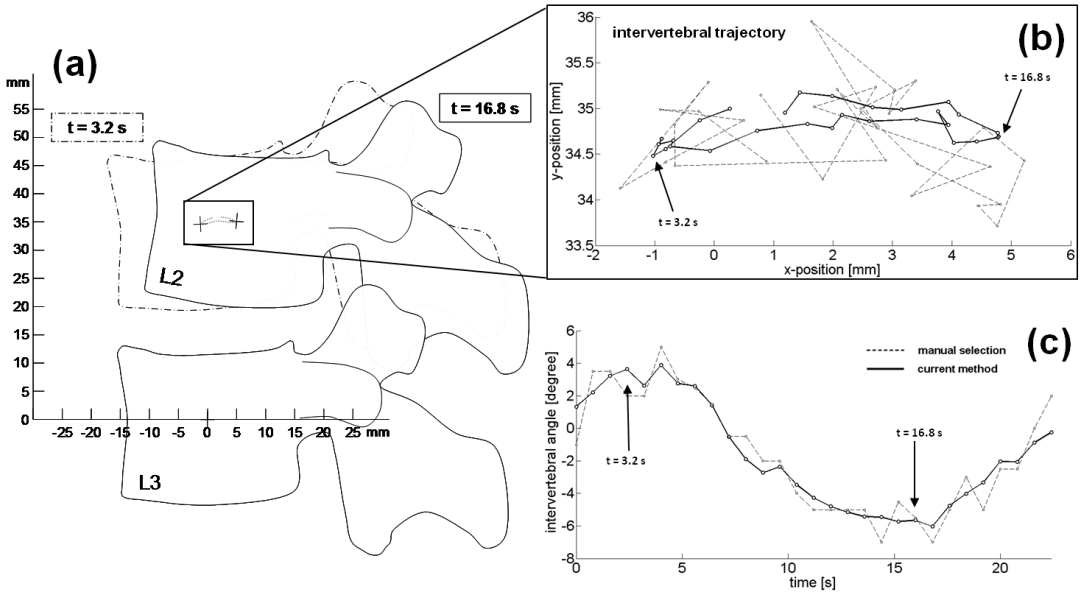

Figure 5.13. Intervertebral kinematics of the L2-L3 segment of the subject #1. (a) Drawing of the L2-L3 segment at two different time instants (t=3.2 s, dash-dotted lines, and t=16.8 s, continuous lines); (b) Intervertebral trajectory of L2 with respect to L3 (fixed); (c) L2-L3 intervertebral angle against time. Manual data: dashed lines; current results: continuous bold lines (from Cerciello et al., 2011b).

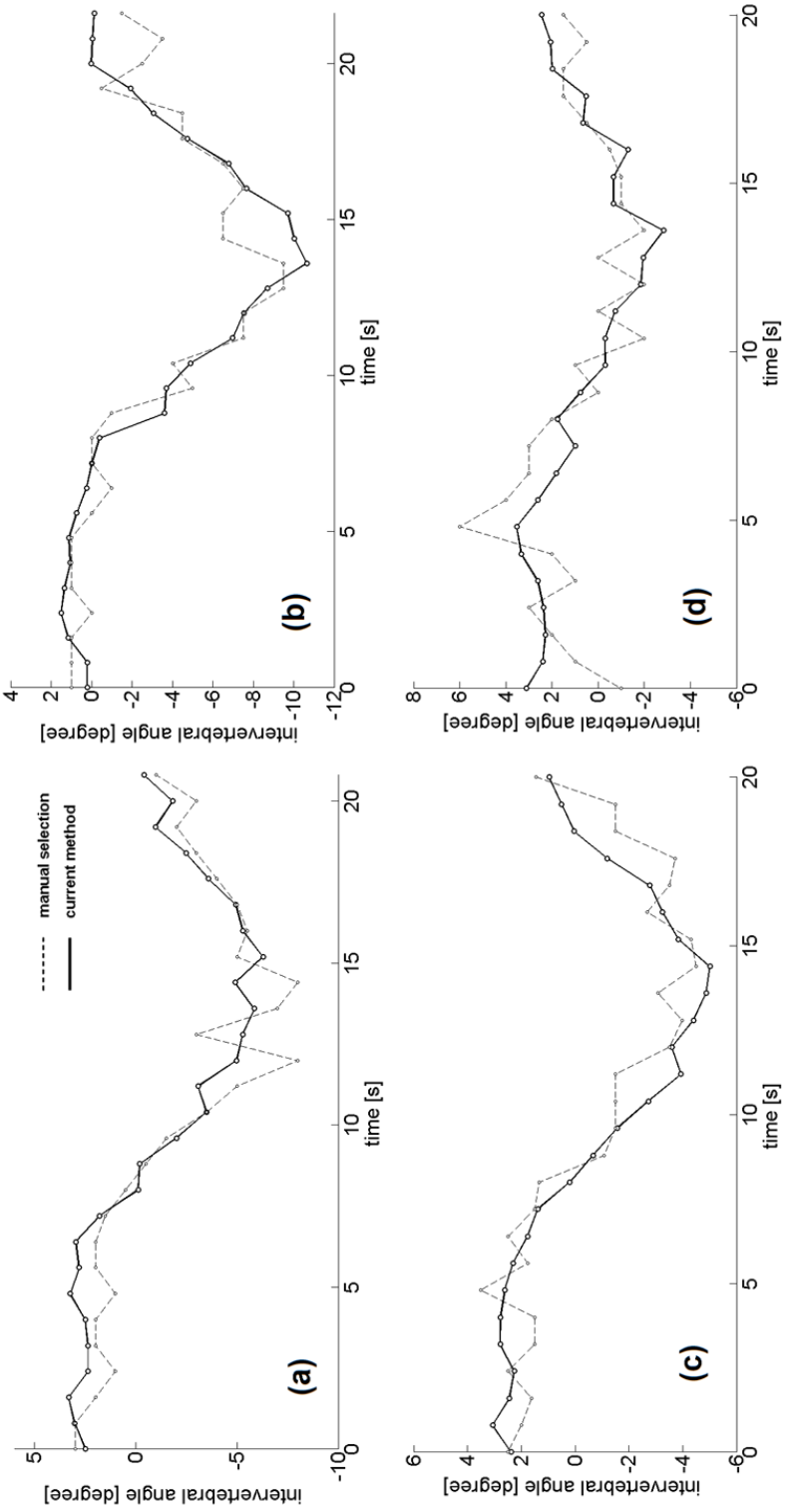

Figure 5.14. L2-L3 intervertebral angle plotted against time. Manual data: dashed lines; current results: continuous bold lines ((a): subject #2, (b): subject #3, (c): subject #4, (d): subject #5) (from Cerciello et al., 2011b).

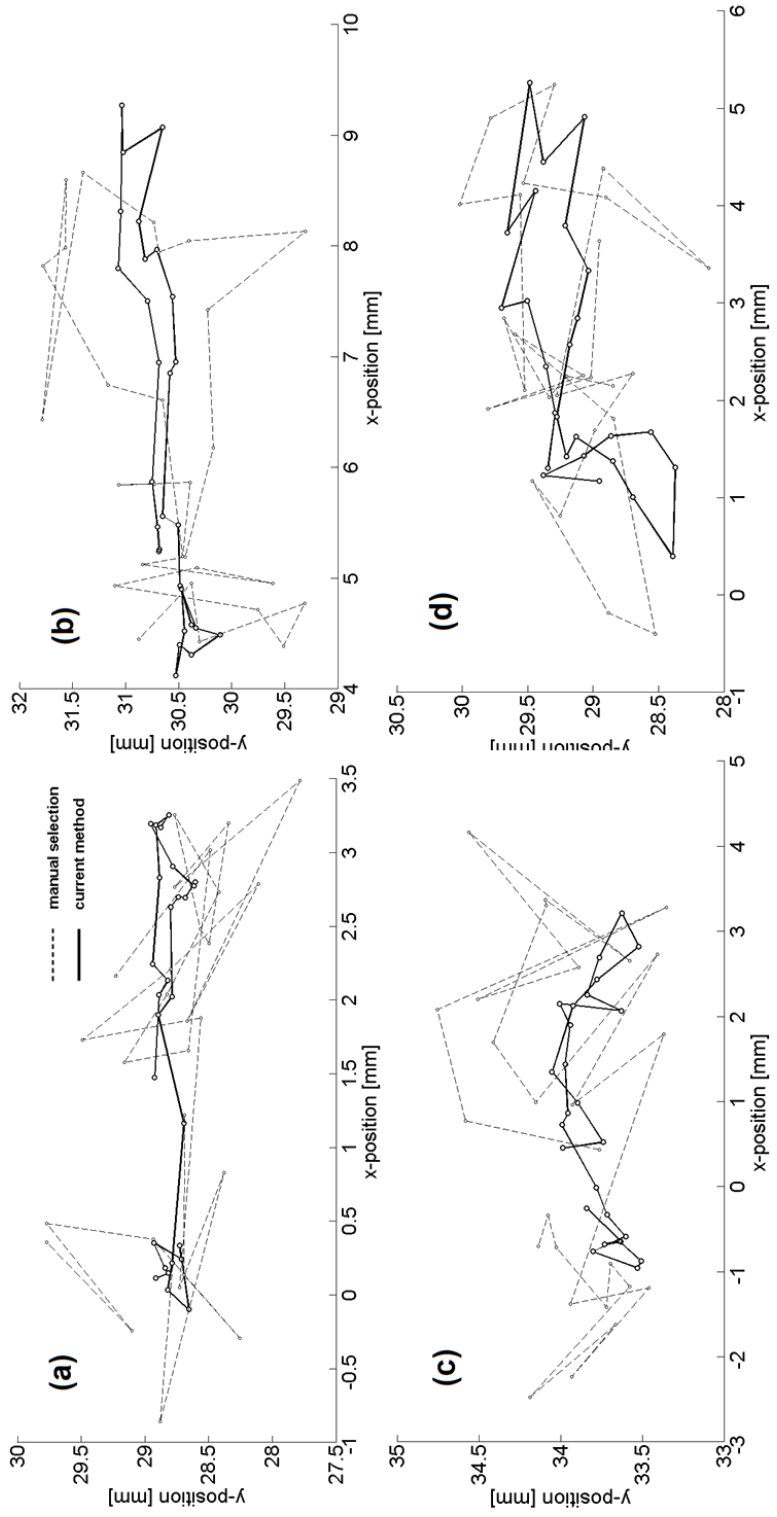

Figure 5.15. L2-L3 intervertebral trajectory. Manual data: dashed lines; current results: continuous bold lines ((a): subject #2, (b): subject #3, (c): subject #4, (d): subject #5) (from Cerciello et al., 2011b).

5.4.2 Discussion

Results obtained from the calibration model have assessed the proposed methodology against known values of intervertebral angle and position. In this regard, it is worth highlighting that the model was built with some tolerances for the rotation angle contained within ±1° (Breem, 1991; Bifulco et al., 2001; Muggleton and Allen, 1997; Simonis, 1994); as a result, all the examined studies have provided results within this range, but with a common, small bias for the intervertebral angle values. In the light of this, results obtained for the center of rotation are more significant in order to assess the accuracy of intervertebral kinematic estimation. The proposed method has provided an excellent localization of the center of rotation, in spite of the fact that it is the most sensitive to measurement errors (i.e. is the most sensitive to vertebrae mislocation) (Panjabi, 1979; Panjabi, 1992a).

The employed model represents, however, a highly simplified setting: the lower vertebra is fixed, the upper vertebra performs a pure rotation around the fixed center of the joint, there is no soft tissue and images do not show motion artefacts. *In vivo* measurements will be, therefore, affected by higher errors than those obtained using the calibration model. A comparison of different methods (manual and automated) by using *in vivo* fluoroscopic spinal images has been thus performed in order to better evaluate the clinical feasibility of the proposed methodology.

According to the results obtained by the estimation of measurement errors, the proposed methodology is resulted to provide a better estimate of the *in vivo* intervertebral kinematics with respect to the other examined methods (Kondracki, 2001; Bifulco et al., 2001; Muggleton and Allen, 1997; Zheng et al., 2004). In particular, a more gradual and smoother evolution of the intervertebral kinematic parameters over time has been observed respect to those obtained by manual landmarking. This should indicate a better performance in describing the intervertebral kinematics. Indeed, it is reasonable to expect that intervertebral motion is smooth and progressive; this hypothesis is also enforced by considering that intervertebral disc acts as a shock absorber and, therefore, smoothes sudden variations in intervertebral rotation and translation (Adams et al., 1996). Therefore, the alternating variations around the local mean of the intervertebral angle and

position is associated with measurement random errors and not to real intervertebral motion.

It is also important to note that measurement errors are also resulted to be reasonably smaller that the expected measurements of abnormal translation and rotation (range of motion) for diagnosis of intervertebral instability. This offers encouraging expectations for clinical application of the method.

5.5 Summary

Intervertebral kinematic estimation is based on the recognition of vertebral bodies in fluoroscopic image sequences. Manual landmarking is generally used in clinical setting mainly due to its simplicity . This operation can, however, result in an inaccurate estimation of kinematic parameters. Automated approaches can, on the contrary, limit the reliance on the operator and improve the accuracy of estimation. In this Chapter the main automated approaches proposed in literature for vertebrae recognition in fluoroscopic image sequences have been examined and compared. In addition, a recently proposed automated method based on cross-correlation template matching has been described in details. The innovative part of this method is the use of gradient images (instead of raw images) combined with an adapted cross-correlation index for template matching procedure. The analysis of the accuracy of the proposed method witnesses its clinical potential with respect to manual landmarking and other automated approaches.

In Chapter VI the possibility to represent the estimated intervertebral kinematic data as continuous-time signals and to describe the actual motion pattern of instantaneous center of rotation is explored.

Chapter 6

Continuous description of intervertebral motion

If a function x(t) contains no frequencies higher than B hertz, it is completely determined by giving its ordinates at a series of points spaced 1/(2B) seconds apart
Claude Elwood Shannon

Diagnosis of segmental instability is commonly based on measurement of abnormal range of motion (i.e. sagittal translation and rotation) through plain radiographs of end-of-range spinal positions. Anterior translation greater than 3 mm and sagittal rotation greater than 10° are generally assumed as suggestions for surgical operation (Leone et al., 2007). Several studies on lumbar spine seem, however, to suggest that disc degeneration can maintain intervertebral ROM within a normal range, while providing an abnormal location of intervertebral center of rotation (for instance, Fujiwara et al., 2000; Schneider et al., 2005). Similar considerations have been raised by a few studies on cervical spine kinematics (Bogduk and Mercer, 2000; Dimnet et al., 1982; Hwang et al., 2008; Lee et al., 1997; Subramanian et al., 2007; Van Mameren et al., 1992),, which recognized center of rotation as the most sensitive parameter to assess mild disc degeneration. The estimation of intervertebral CR suffers, however, from some restrictions that limit its feasibility in clinical setting. An appropriate representation of instantaneous center of rotation requires that the

continuous-time functions of intervertebral rotation and translation or at least a large number of intervertebral positions representing the motion are known. However, in clinical setting a limited number of spinal radiographs are generally acquired in order to limit the X-ray exposure to the patient; as a consequence, a rough approximation to ICR, the so-called finite center of rotation, estimated between two end-of-range spinal positions[5], must be assumed. FCR can offer only a qualitative representation of segmental motion: the motion occurred in between the assumed spinal positions can be significantly varied with respect to that represented by the FCR. At the present, only very few *in vitro* studies have reported accurate estimation of actual instantaneous helical axes of rotation (IHA) for spinal segments (Mansour et al., 2004; Nägerl et al., 2009; Wachowski et al., 2007; Wachowski et al., 2009a; Wachowski et al., 2009b; Wachowski et al., 2010), while no *in vivo* trajectory of ICR has been reported yet.

A continuous-time description of lumbar intervertebral kinematics can offer the opportunity to estimate the actual ICR during the entire segmental motion. Unlike functional flexion-extension radiography, videofluoroscopy provides a continuous screening (at the frame rate) of specific spinal tracts during patient's motion with an acceptable X-ray dose. Intervertebral kinematic estimation is, however, generally affected by large errors due to the low quality of fluoroscopic images, especially for lumbar spine sequences because of the larger amount of soft tissue involved (Bifulco et al., 2001; Cerciello et al., 2011b; Muggleton and Allen, 1997). This is particularly true for estimation of center of rotation (Chen and Katona, 1999; Panjabi, 1979; Panjabi et al., 1982; Panjabi et al., 1992a). Indeed, ICR is very sensitive to the sudden oscillations (i.e. measurement errors) of the estimated intervertebral motion signals (see also paragraph 5.4.1) and can result displaced very far from the motion segment (i.e. its location provides no clinical information). In addition, CR estimate would result restricted to the fluoroscope frame rate (i.e. set-up resolution).

Both needs to reduce measurement errors and to obtain a continuous-time representation of motion extracted by videofluoroscopy can be met through the

[5] Accuracy of FCR estimation is proportional to the magnitude of intervertebral angle of rotation (…). End-of-range spinal positions (i.e. full flexion and full extension) are assumed also for reducing measurement errors.

application of smoothing spline to the kinematic data. Smoothing spline, introduced by Schoenberg (1964) and Reinsch (1967), provides a practical method of smoothing and accurately fitting of biomechanical data (D'Amico and Ferrigno, 1992; Fazel-Rezai and Shwedyk, 1998; McLaughlin et al., 1977; Woltring, 1985; Wood and Jennings, 1979; Wood 1982; Xu et al., 2010a; Xu et al., 2010b). By using spline interpolation kinematic signals and their derivatives can be calculated at any instant of time, while the level of their smoothing is controlled by a single parameter. This can be particularly useful for accurately estimating ICR at any instant of the entire segmental motion.

In this Chapter the application of smoothing spline for obtaining a smooth and continuous-time description of intervertebral kinematics and, more specifically, the estimation of instantaneous center of rotation is discussed. Geometrical considerations on the estimation of ICR are reported in paragraph 6.1, while theoretical considerations supporting the spline interpolation of kinematic data for estimating ICR are illustrated in paragraph 6.2. The application of the spline interpolation method to the estimated experimental intervertebral data (see Chapter V) is discussed in paragraph 6.3.

6.1 Estimation of instantaneous center of rotation

Given a 2D rigid body performing an arbitrary roto-translation motion on a plane x,y (in our case the relative motion of L2 vertebra with respect to L3 on the sagittal plane, Figure 6.1), indicating with $\alpha(t)$ the continuous-time function of its angular rotation, with $r_x(t)$ and $r_y(t)$ the x- and y-component of its translation, with $\omega(t)$ ($=d\alpha(t)/dt$) its angular velocity and with $v_x(t)$ ($=dr_x(t)/dt$) and $v_y(t)$ ($=dr_y(t)/dt$) the x- and y-component of its linear velocity, the coordinates of the ICR ((t) with respect to the reference system xOy (fixed to L3) are given by (Meriam and Kraige, 2002; Wilcox, 2006):

$$ICR_x(t) = -\frac{v_y(t)}{\omega(t)} + r_x(t), \quad ICR_y(t) = \frac{v_x(t)}{\omega(t)} + r_y(t). \tag{30}$$

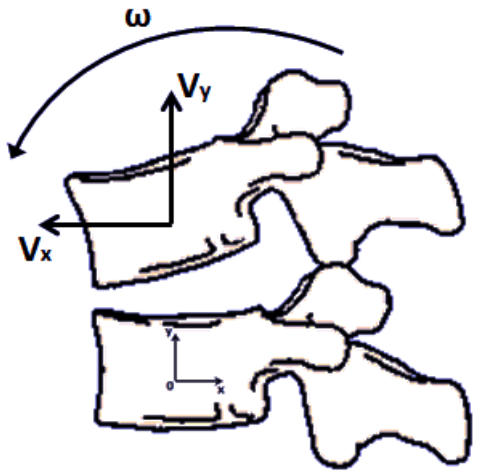

Figure 6.1. Angular and linear velocities used for estimating the ICR of the motion segment.

It is worth noting that ICR could be extremely misplaced from the motion segment when angular velocity is close to zero (i.e. it tends to infinity for pure translations: this is consistent with the definition of ICR). For this reason, the trajectory of the ICR is generally represented only if the absolute value of angular velocity is sufficiently large (i.e. only during the actual performance of intervertebral motion).

6.2 Interpolation and smoothing of noisy discrete kinematic data by splines

According to Eq. (30) the estimation of the actual ICR requires the knowledge of the continuous-time functions of intervertebral angular and linear velocities (i.e. $\omega(t)$, $v_x(t)$ and $v_y(t)$). As a consequence of its dependence on the first derivative of intervertebral motion signals, ICR results very sensitive to measurement errors that must be minimized.

A smooth and continuous-time representation of the joint kinematics can be obtained by interpolating the dataset of estimated kinematic data by cubic smoothing spline functions. Cubic smoothing spline offers a good tradeoff between simplicity and efficiency in adjusting the level of data smoothing, ensures strong continuity up to acceleration and provides a fine convergence to kinematic data with respect to high-

order polynomials that tend to oscillate strongly due to the effect of Runge's phenomenon (D'Amico and Ferrigno, 1992; Xu et al., 2010a; Xu et al., 2010b).
Let the noisy data $z(t_i), i \in [0, n]$ be given and assume that:

$$t_0 < t_1 < \cdots < t_n, \tag{31}$$

the cubic smoothing spline c(t) is the function that minimizes:

$$p\sum_{i=0}^{n}[z(t_i) - c(t_i)]^2 + \int_{t_0}^{t_n}[c''(t)]^2 dn \tag{32}$$

where the smoothing parameter (p) (ranging from 0 to 1) controls the level of smoothing data and c''(t) denotes the second derivate of c(t) (Reinsch, 1967; Schoenberg, 1964).
Using cubic spline a time-continuous polynomial function is obtained for each pair of successive samples of the interpolated kinematic data. Motion signals and their derivatives can be, therefore, calculated at any instant of time by the knowledge of the polynomial coefficients. The kinematic smoothed data obtained by cubic spline can be also considered as the result of a linear low-pass filtering whose level of smoothing is controlled by the smoothing parameter *p*. In case that the noisy data are equispaced and sufficiently long, Feng (1998) established the transfer function of cubic smoothing spline filter (Figure 6.2), given by:

$$H_{lp}(z) = \frac{\frac{1}{6}(z+4+z^{-1})}{\frac{1}{p}\left[z^2+\left(\frac{p}{6}-4\right)z+\left(\frac{2p}{3}+6\right)+\left(\frac{p}{6}-4\right)z^{-1}+z^{-2}\right]}. \tag{33}$$

Using Feng's formulation, low-pass filter cut-off frequency (w_t) can be obtained giving the corresponding value for the smoothing parameter (p) by the expression:

$$w_t \cong \sqrt[4]{(\sqrt{2}-1)p}\,. \tag{34}$$

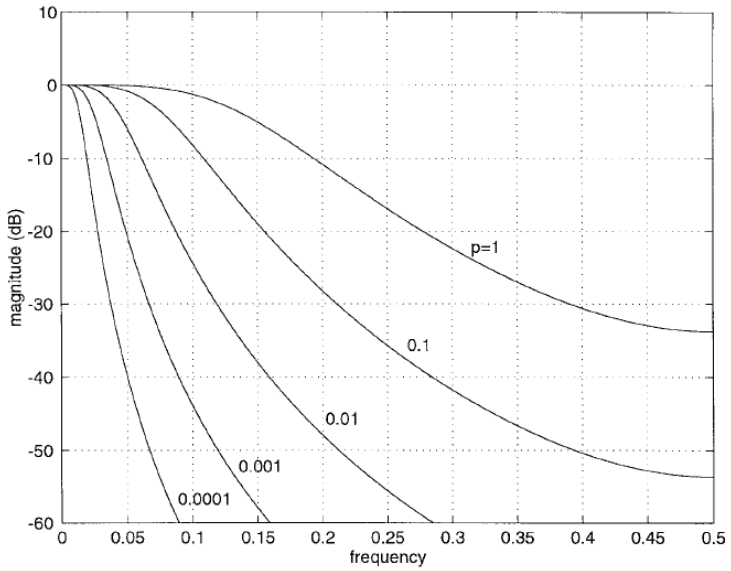

Figure 6.2. Transfer functions of the cubic spline smoothing filter for p = 0:0001; 0:001; 0:01; 0:1, and 1. The filter is equivalent to a fourth-order lowpass filter with a maximum flatness feature (from Feng, 1998).

In other words, the choice of the smoothing parameter (associated with the required level of smoothing) can be inferred by the analysis of the frequency content of signals. As discussed in Chapter V, the lower frequency part of the estimated intervertebral signals within a bandwidth of 0.14 Hz can be associated with motion, while the remaining high-frequency content with noise. This is also consistent to the Sampling Theorem due to the fluoroscope frame-rate of 5 Hz. In other words, for this "enough slow" movement the sampling frequency (frame rate of the fluoroscope) results higher than that minimum required by the Sampling Theorem for a complete, continuous-time reconstruction of the motion signals.

In accord to Eq. (34) the smoothing parameter has been set to 0.6 corresponding to a low-pass filter cut-off frequency equal to 0.14 Hz. The Ljung–Box whiteness test has been performed to ensure that the residuals of the filtering operation (i.e. the filtered out high frequency content) are uncorrelated and, then, representative of random noise and not motion (see also Burkhart et al., 2011).

6.3 Case study 2: *in vivo* fluoroscopic sequences

Experimental intervertebral data obtained by (L2 and L3) vertebrae tracking in five fluoroscopic spinal sequence of healthy subjects undergone passive lumbar motion have been utilized (see Chapter V) (Cerciello et al, 2001v). Cubic spline interpolation of experimental data have been performed in order to obtain a smooth and continuous-time representation of the intervertebral motion signals and to estimate the ICRs during the actual intervertebral motion. Results of spline interpolation are reported in paragraph 6.3.1, while the clinical feasibility of the described methodology is discussed in paragraph 6.3.2.

6.3.1 Data comparison

The experimental discrete data (i.e. estimated L2-L3 intervertebral angles, α, and positions, r_x and r_y) have been interpolated by a cubic smoothing spline (with the smoothing parameter set to 0.6). As an example, Figure 6.3 shows a description of L2-L3 intervertebral motion extracted by videofluoroscopy and the corresponding smoothing spline approximation (subject #4: intervertebral angle and x- and y-displacement against time). According to the motion impressed by the motorized table, it is recognizable a joint extension followed by a flexion. Below, the residuals of the smoothing operation are also shown.

For each pair of successive samples a time-continuous polynomial function is obtained. By the knowledge of the polynomial coefficients of the interpolating functions the first derivative of the kinematic signals (i.e. angular velocity, $\omega(t)$, and linear velocities, $v_x(t)$ and $v_y(t)$) can be calculated at any instant of time.

To better appreciate the continuous-time interpolation and the low-pass filtering provided by splines, Figure 6.4 presents an enlargement of Fig. 6.3a (from the 7^{th} to the 11^{th} second), where the experimental data of intervertebral rotation are represented as white circles, while the resulting smoothing spline as a continuous bold line. As an example, for a time interval between two subsequent samples (at the times t=9.2[s] and t=9.4[s]) the expression of the continuous-time function is shown. Below, the corresponding angular velocity signal associated with this inter-sample time interval is also reported.

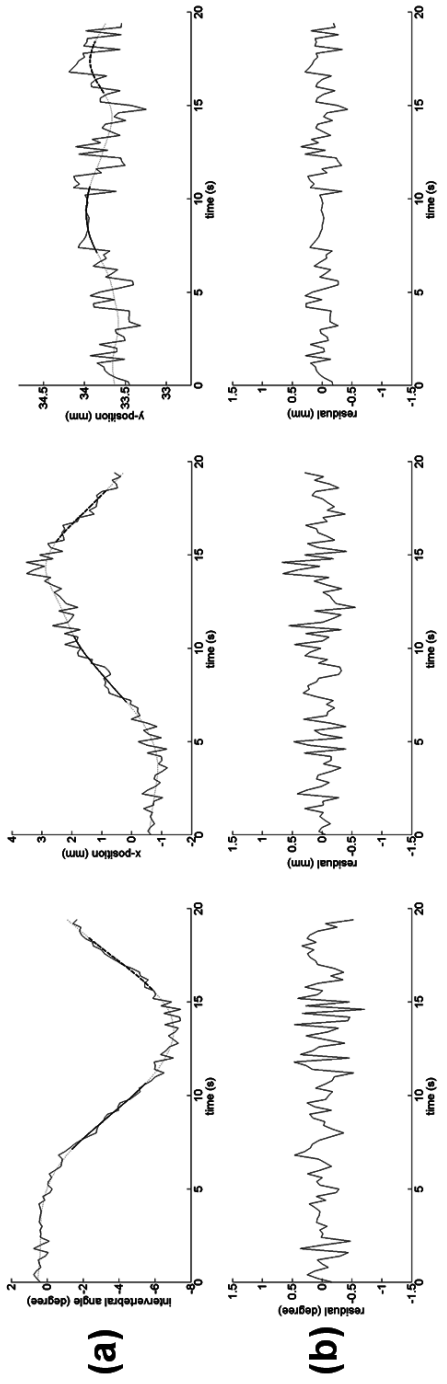

Figure 6.3. (a, from left to right) Intervertebral angle, x- and y-displacement of the L2 vertebra with respect to L3 plotted against time (subject #1). Raw data: continuous line; filtered data (by smoothing spline, p=0.6): dotted line. During patient's motion, the intervertebral joint performs an extension followed by a flexion. On filtered data, extension is shown as a continuous bold line and flexion as a dashed bold line in correspondence of intervertebral angular velocity (absolute value) greater than 1 degree per second; (b) corresponding residuals of the smoothing operation (difference between the raw and filtered signals). Residual values are plotted using an expanded y-scale (from Bifulco et al., expected 2012).

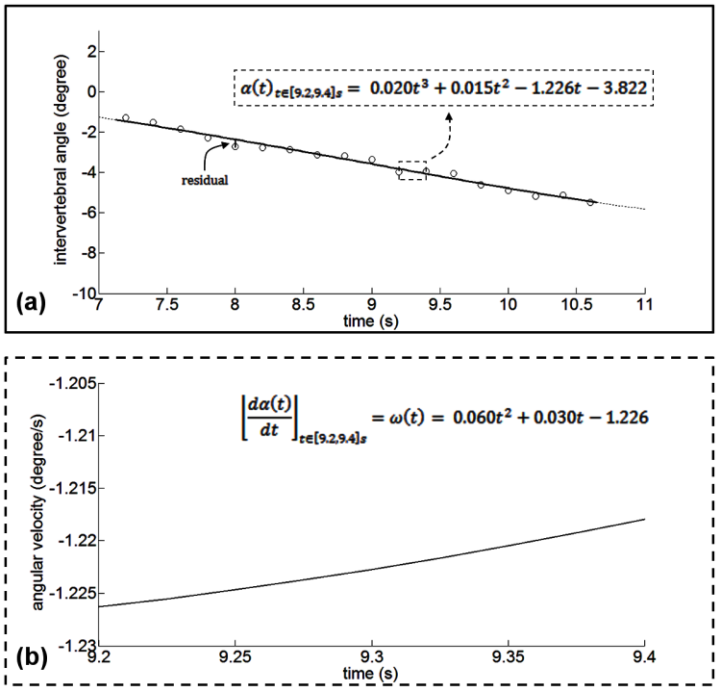

Figure 6.4. (a) A particular of the interpolation of experimental data relative to the intervertebral rotation (already shown in Fig. 2a) in the time interval that goes from 7 [s] to 11 [s]. Experimental data are depicted as white circles, while the continuous-time function provided by the smoothing spline interpolation is represented as a continuous bold line. As an example, the expression of the interpolating function between two subsequent samples (t=9.2[s] and t=9.4[s]) is reported; (b) The corresponding angular velocity signal (i.e. ω(t)) associated to the regarded time interval (t=9.2[s] - t=9.4[s]) and the expression of the interpolating function (from Bifulco et al., expected 2012).

Figure 6.5 represents the estimated intervertebral angular and linear velocities obtained by the polynomial differentiation of the spline approximations depicted in Figure 6.3a. The angular accelerations resulted lower than 1.08 degree/s^2 which is consistent with the table motion.

Concise measurements of overall intervertebral rotation (i.e. angle extent) and translation (i.e. horizontal displacement) have been extracted from the continuous-time kinematic signals. To evaluate the clinical effectiveness of the spline interpolation method, a comparison between these concise measurements and standard parameters currently used in clinical application has been performed (see Table 6.1, results are shown as mean +/- standard deviation): intervertebral sagittal rotation and translation have been repeatedly computed at patient's full extension (at time t=12.6[s]) using the technique proposed by Dupuis et al. (1985), while FCR have been calculated between different image-pairs according to McCane et al. (2005). Having multiple images at either end of the spinal motion, not a single FCR

measurement, but a set of them has been calculated between the neutral position (at $t_{i,1}$=1.8[s], $t_{i,2}$=2.0, $t_{i,3}$=2.2, $t_{i,4}$=2.4; $t_{i,5}$=2.6, $t_{i,6}$=2.8, $t_{i,7}$=3.0, $t_{i,8}$=3.2, $t_{i,9}$=3.4, $t_{i,10}$=3.6, for a total of 10 images) and the full extension (at $t_{f,1}$=12.6[s], $t_{f,2}$=12.8, $t_{f,3}$=13.0, $t_{f,4}$=13.2; $t_{f,5}$=13.4, $t_{f,6}$=13.6, $t_{f,7}$=13.8, $t_{f,8}$=14.0, $t_{f,9}$=14.2, $t_{f,10}$=14.4, for a total of 10 images) of the L2-L3 segmental motion (Figure 6.6). On average, absolute differences result 0.74 degrees for sagittal rotation, 0.59 mm for translation and 1.02 mm for the x- and y-position of center of rotation.

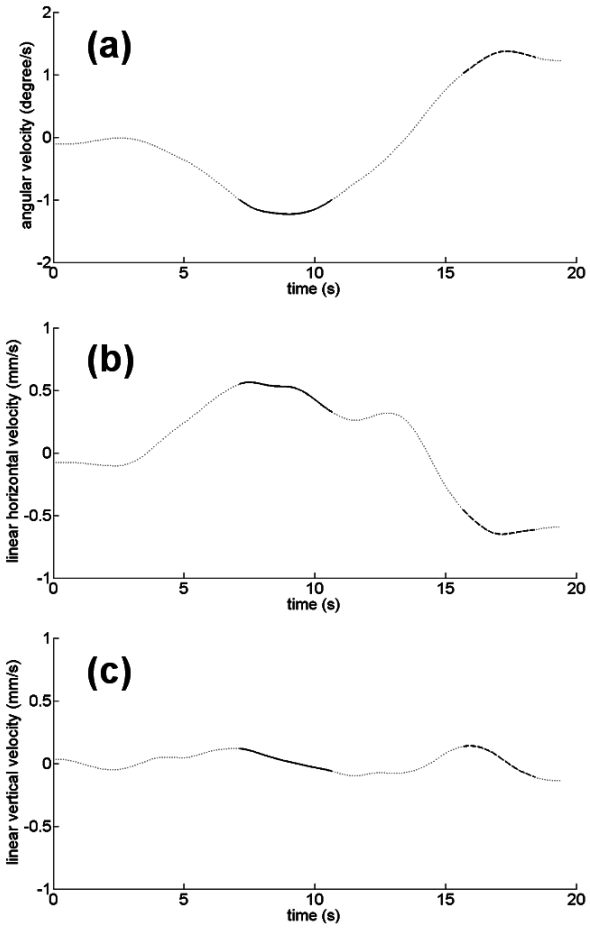

Figure 6.5. (a) Angular linear velocity, (b) linear horizontal velocity (anterior-posterior direction) and (c) linear vertical velocity (cranial-caudal direction) of the L2 vertebra with respect to L3 (that is assumed to be fixed) plotted against time (subject #1). Extension: continuous bold line; flexion: dashed bold line (as in Fig. 2a) (from Bifulco et al., expected 2012).

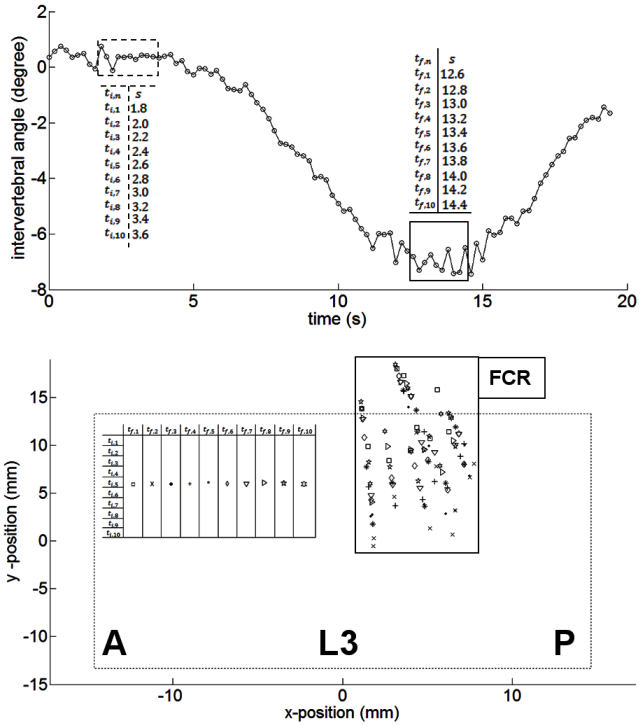

Figure 6.6. (a) Intervertebral angle of the L2 vertebra with respect to L3 plotted against time (subject #1) with the instants of time between which the FCRs have been computed; (b) FCRs obtained by considering different image-pairs between the neutral position and the full extension of the motion segment.

As previous mentioned, the spectral content of the experimental raw data (angle, x- and y-position) results highly similar for all subjects, showing a main component at about 0.05 Hz and concentrating more than 95% of the energy below 0.14 Hz that is the equivalent cut-off frequency for a spline smoothing parameter of about 0.6 (see Eq. (34). Residual analysis has been performed for all the subjects and smoothing parameters. The whiteness of the filtering residuals has been verified (with a significance level of 0.05) for smoothing parameters greater than 0.3.

As an example, the trajectory of the estimated ICR of the subject #4 is represented in Figure 6.7c superimposed on a schematic profile of the L2-L3 vertebral segment. The ICRs are located just below the superior endplate of the L3 vertebra in the posterior half. During the extension the ICR moves from a posterior position to an anterior, while during the flexion on the contrary direction. The corresponding L2-L3 FCR loci (presented as mean +/- standard deviation) are plotted for comparison (Figure 6.7d). On the top, the trajectory of the L2 vertebra center with respect to the

L3 (fixed) is also represented (Figure 6.7b). For sake of completeness, the ICR trajectories obtained for different smoothing parameters are shown in Figure 6.8.

Some authors have suggested that a higher-order smoothing spline (than cubic) should produce a better approximation to derivatives of kinematic data at endpoints ((Fazel-Rezai and Shwedyk, 1998; Woltring, 1985; Wood and Jennings, 1979; Wood 1982). However, endpoints errors in first derivative data (i.e. velocity) are negligible (Vint and Hinrichs, 1996) and, in any case, no points have been considered at the extremities of data sets. In addition, spinal motion is generally smooth and progressive (i.e. acceleration is close to zero). In practice, no significant evidence can be recognized between results obtained by quintic smoothing spline with respect to cubic spline interpolation. As a confirmation, Figure 6.9 shows the ICR locations estimated by quintic spline interpolation. A comparison between measurements obtained after cubic and quintic spline interpolation has been also performed (see Table 6.1); on average, absolute differences between cubic and quintic spline result 0.05 degrees for sagittal rotation, 0.11 mm for translation and 0.07 mm and 0.32 mm for the x- and y-average position of ICR, respectively.

Figure 6.11 represents the L2-L3 ICR locations obtained for the other subjects (#1, #2, #3, #5).

Table 6.1. Concise measurements of intervertebral motion (mean +/- standard deviation)

subject #number (neutral position – full extension time [s])	method	sagittal rotation [degree]	sagittal translation [mm]	center of rotation [mm]	
				X	Y
subject #1 (5.2s – 13.6s)	standard measurement	7.96 ± 1.34	3.40 ± 1.00	4.27 ± 1.90	9.30 ± 4.61
	continuous kinematics (cubic)	7.04	3.46	2.35 ± 2.32	9.37 ± 3.35
	continuous kinematics (quintic)	7.08	3.49	2.33 ± 2.52	9.87 ± 3.88
subject #2 (6.6s – 14.2s)	standard measurement	9.64 ± 1.40	4.21 ± 1.17	8.50 ± 1.72	9.01 ± 3.75
	continuous kinematics (cubic)	9.88	3.87	9.41 ± 1.77	9.38 ± 5.67
	continuous kinematics (quintic)	9.95	4.16	9.53 ± 1.77	9.14 ± 5.99
subject #3 (6.6s – 15.6s)	standard measurement	6.09 ± 1.77	3.21 ± 2.15	3.76 ± 1.77	-0.19± 3.94
	continuous kinematics (cubic)	7.16	4.59	3.54 ± 1.62	5.04 ± 2.97
	continuous kinematics (quintic)	7.18	4.58	3.61 ± 1.56	4.81 ± 2.98

* Standard measurements: sagittal rotation and translation (Dupuis et al., 1985), center of rotation (McCane et al. 2005); smoothing parameter (cubic and quintic spline): 0.6; center of rotation for the continuous kinematics (cubic and quintic spline) is assumed only for intervertebral angular velocity (absolute value) greater than 1 degree per second.

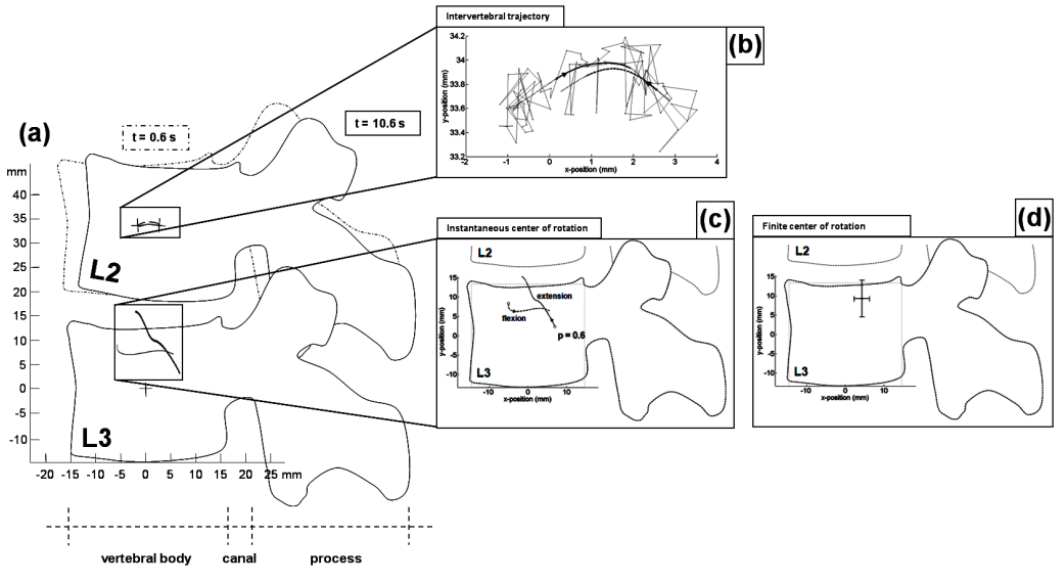

Figure 6.7. (a) Schematic drawing of the L2-L3 segment of the subject #1 at two different time instants (t=0.6s, dash-dotted lines, and t=10.6 s, continuous lines); (b) Enlarged detail of the intervertebral trajectory of the L2 vertebra with respect to L3 (fixed). Positive angles correspond to flexion, while negative angles to extension. Raw data: continuous gray line; filtered data (by cubic spline, p=0.6): dotted line; extension: continuous bold line; flexion: dashed bold line; (c) Enlarged detail of the trajectory of the instantaneous center of rotation (ICR) obtained using cubic spline, p=0.6. Extension: continuous bold line; flexion: dashed bold line. Initial ICR positions in extension and in flexion are represented as a white circles, solid black arrows represent the directions of the ICR trajectory during extension and flexion; (d) Loci (mean ± standard deviation) of the finite center of rotation (FCR) obtained (McCane et al., 2005) by considering different image-pairs between the neutral position (at $t_{i,1}$=1.8[s], $t_{i,2}$=2.0, $t_{i,3}$=2.2, $t_{i,4}$=2.4; $t_{i,5}$=2.6, $t_{i,6}$=2.8, $t_{i,7}$=3.0, $t_{i,8}$=3.2, $t_{i,9}$=3.4, $t_{i,10}$=3.6, for a total of 10 images) and the full extension (at $t_{f,1}$=12.6[s], $t_{f,2}$=12.8, $t_{f,3}$=13.0, $t_{f,4}$=13.2; $t_{f,5}$=13.4, $t_{f,6}$=13.6, $t_{f,7}$=13.8, $t_{f,8}$=14.0, $t_{f,9}$=14.2, $t_{f,10}$=14.4, for a total of 10 images) of the segmental motion; a set of 100 FCRs were obtained by considering all possible combinations of images-couples between the initial stage of motion (neutral position) and the final stage of motion (full extension). The location of this distribution should be compared to the ICR trajectory in extension (from Bifulco et al., expected 2012).

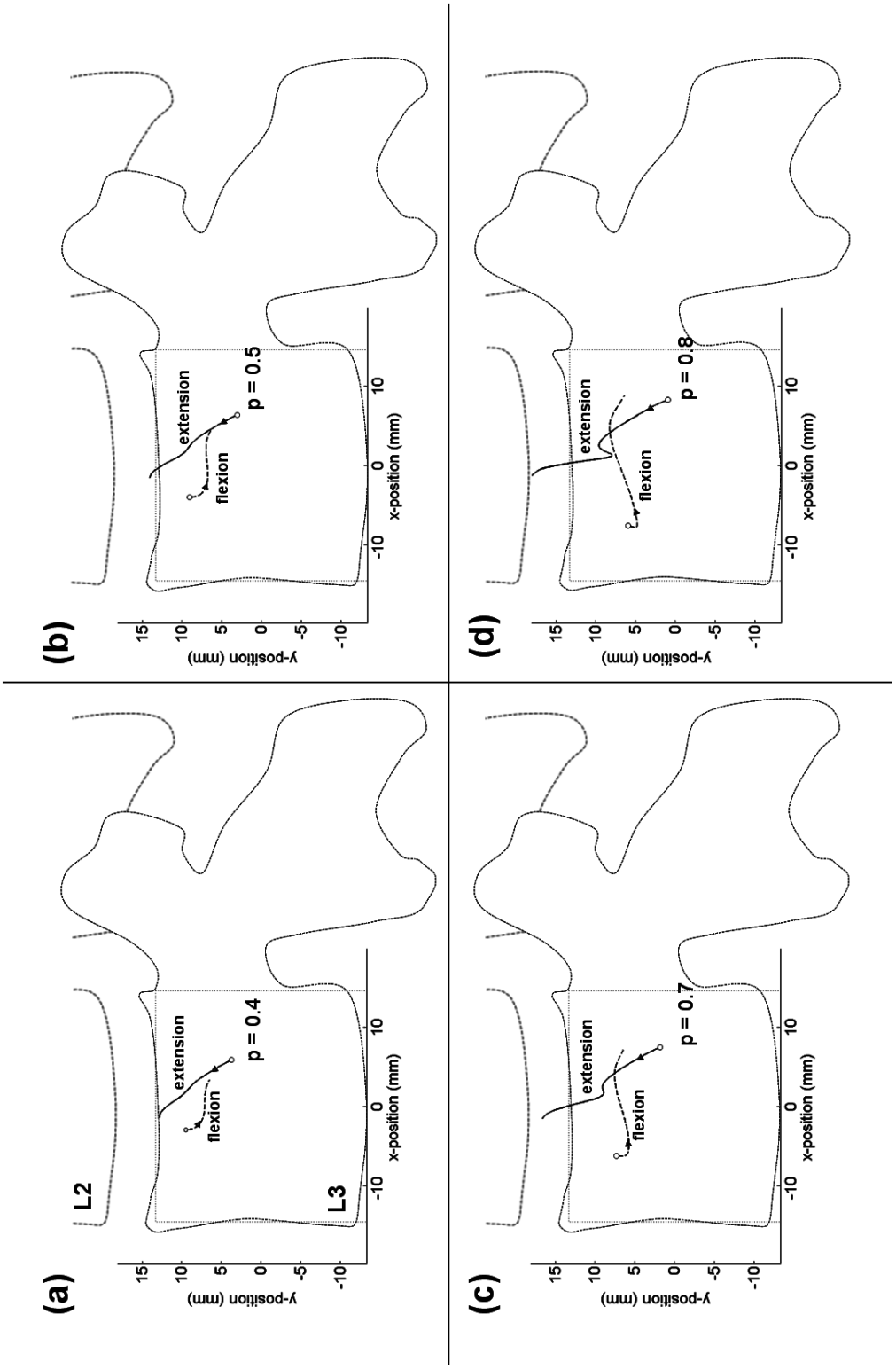

Figure 6.8. ICR trajectories obtained by cubic spline using different smoothing parameter ((a) p=0.4; (b) p=0.5; (c) p=0.7; (d) p=0.8) superimposed on the schematic drawing of the L2-L3 segment (subject #1). Extension: continuous bold line; flexion: dashed bold line. The whiteness of the residuals was positively verified for all these smoothing parameters by Ljung–Box test (with a significance level of 0.05) (from Bifulco et al., expected 2012).

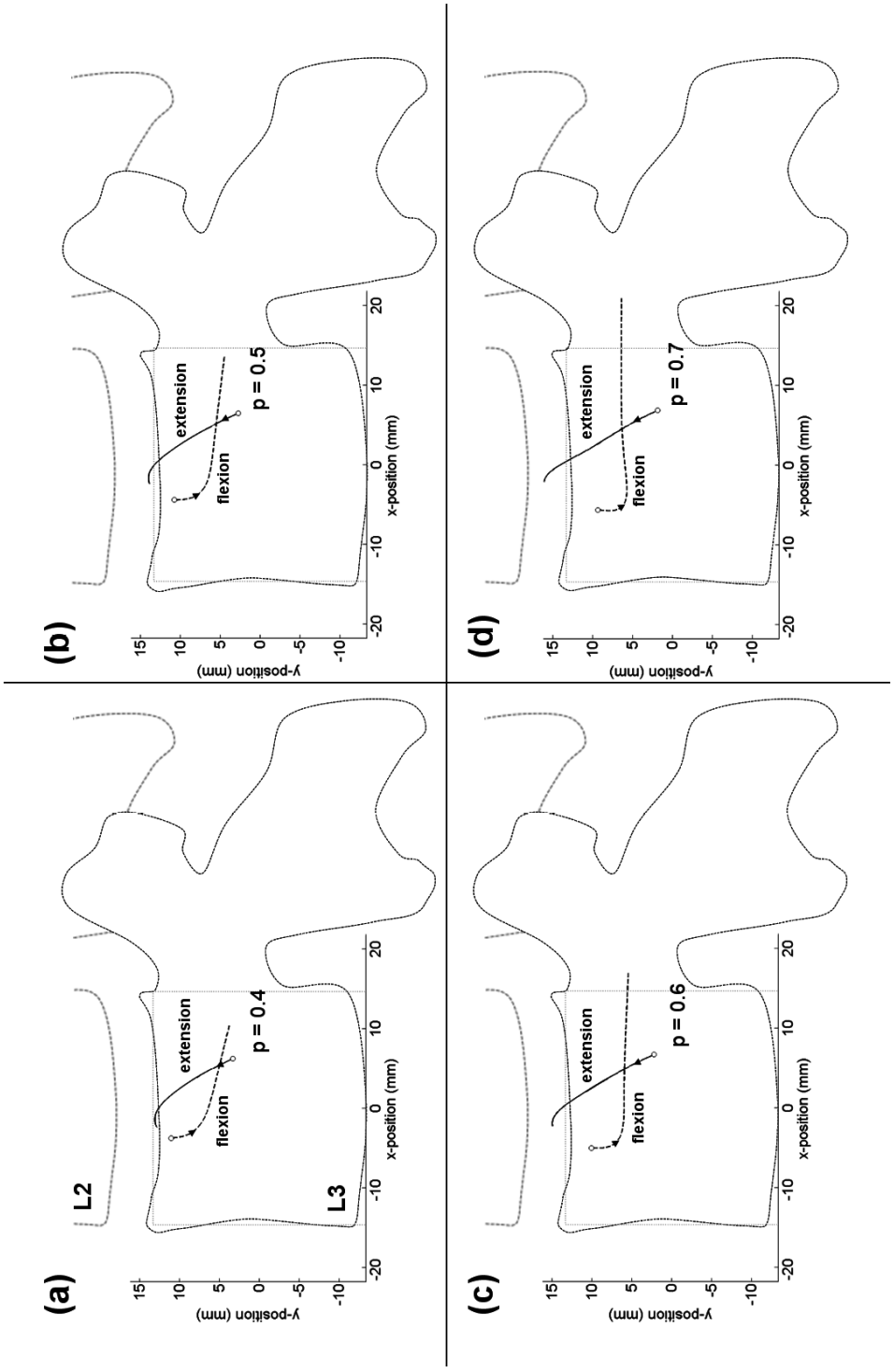

Figure 6.9. ICR trajectory obtained by using quintic smoothing spline (smoothing parameter: (a) *p*=0.4; (b) *p*=0.5; (c) *p*=0.6; (d) *p*=0.7) superimposed on the schematic drawing of the L2-L3 segment (subject #1). Extension: continuous bold line; flexion: dashed bold line. The whiteness of the residuals was positively verified for all these smoothing parameters by Ljung–Box test (with a significance level of 0.05). These trajectories (quintic spline) should be compared with those correspondent (cubic spline) showed in Fig. 6.8 (from Bifulco et al., expected 2012).

6.3.2 Discussion

For using smoothing spline interpolation the degree of the piecewise-polynomial function and the smoothing parameter has been conveniently chosen. In this regard, it is important to note that patient's motion must be slow enough both to satisfy the Sampling Theorem due to the fluoroscope frame rate (see also paragraph 6.2) and to provide good quality images (i.e. small motion blurring). Furthermore, it is well-known that intervertebral disc acts as a damper (Niosi and Oxland, 2004) and segmental motion is limited in its performance. As a consequence, true kinematic signals are confined within very low-frequency, while the sudden oscillations of the estimated kinematic signals (Figure 6.4a) are associated with measurement error and not with motion (otherwise, this would require an excessive amount of energy loss due to viscoelastic properties of soft tissues) (Cerciello et al., 2001b; Challis, 1995; Cholewicki et al., 1991). In practice, continuous-time kinematics can be obtained by smoothing spline without using higher degree polynomials (than cubic) and very low smoothing parameter. This is also confirmed by the small difference occurs on the estimated ICR locations by using different smoothing parameters (Figure 6.9) or quintic spline instead of cubic (Figure 6.10). As an evidence of the appropriateness of the filtering operation, it has been also observed that the residuals between the raw and filtered kinematic signals are uncorrelated (i.e. corresponding to white noise and not to motion).

Kinematic measurements extracted from the continuous-time description of intervertebral motion are resulted to be consistent with those estimated by methods currently employed for clinical diagnosis of segmental instability (Dupuis et al., 1985; McCane et al., 2005). Intervertebral ICR trajectories also result in accordance with accurate kinematic data (IHA migration) obtained *in vitro* for a flexion-extension movement of lumbar segments by using a high resolution kinematic tracking system (Mansour et al., 2004; Nägerl et al., 2009; Wachowski et al., 2007; Wachowski et al., 2009a; Wachowski et al., 2009b; Wachowski et al., 2010).

As previously mentioned, the estimated ICR is located at the posterior half of the lower vertebra (L3), slightly below the superior endplate. This is about in agreement with previous FCR locations presented in literature for *in vivo* spinal motion (Pearcy and Bogduk, 1988; Schneider et al., 2005; Xia et al., 2010) and *in vitro* studies

(Gertzbein et al., 1984; Haher et al., 1992; Rousseau et al., 2006a; Rousseau et al., 2006b; Schmidt et al., 2008a; Schmidt et al., 2008b; White and Panjabi, 1990). However, it is important to note that the spinal motion was passively performed by a motorized table and neither load on the spine nor the action of neuromuscular elements were involved. In principle, this could alter the segmental kinematics.

6.4 Summary

Intervertebral kinematics closely depends on condition of the soft tissue intended for constraining segmental motion. Disc degeneration, facet joints osteoarthritis, ligamentous degeneration and muscle alterations can lead to vertebral instability that is suggested to be a major cause of low back pain.

In clinical practice diagnosis of intervertebral instability is based on concise measurements of range of intervertebral motion through functional flexion-extension radiography. However, it was largely pointed out that intervertebral instantaneous center of rotation is much more sensitive to mild degeneration of disc and ligament with respect to range of motion. Generally, FCR is computed from only two or a few more segmental positions using functional radiography and is improperly assumed as a rough approximation to ICR. Errors in FCR computation are even larger than for the other kinematic parameters.

With respect to functional radiography, videofluoroscopy can provide the description of the complete performance of intervertebral motion. However, the need of extremely accurate intervertebral kinematic measurements has, to date, limited the clinical application of videofluoroscopy. Smoothing spline can offer a suitable and practical technique for interpolation and differentiation of sampled kinematic data extracted by videofluoroscopy, offering both noise reduction (that is necessary to avoid erroneous misplacements of ICR from the motion segments) and continuous-time motion representation (that permits to estimate the CR at any instant of time).

Continuous-time description of intervertebral motion by smoothing spline is appeared to provide an enrichment of information obtained by functional radiography and, more specifically, the possibility to estimate the trajectories of the actual ICR in lumbar spine during *in vivo* flexion-extension motion. This can have a

significant impact on clinical evaluation of early disc degeneration and segmental instability and in evaluating prosthetic implant performance.

Conclusion

When something can be read without effort,
great effort has gone into its writing.
Enrique Jardiel Poncela

An automated method specifically designed for a very accurate recognition of vertebral bodies in fluoroscopic sequences of lumbar spine motion in the sagittal plane has been described. The method involves a strong enhancement of the outline of vertebral bodies by estimating gradient images. An accurate characterization of fluoroscopic noise has been proposed and severe image denoising has been performed in order to achieve a more reliable estimate of the gradient images. The method has been validated against known values of intervertebral angle and position of a spinal calibration model and results for real fluoroscopic sequences of lumbar spine motion in the sagittal plane have been compared to results obtained from the same image sequences using manual landmarking and other automated algorithms.

A smooth and continuous-time representation of intervertebral motion based on cubic spline interpolation of the experimental kinematic data extracted by videofluoroscopy has been proposed. Analysis of frequency content of intervertebral signals has been involved to choose the most suitable smoothing parameter. Instantaneous center of rotation has been estimated during the entire intervertebral motion by the knowledge of the continuous-time intervertebral signals and their derivatives. To evaluate the clinical feasibility of the proposed spline interpolation

method, a comparison has been performed between concise measurements of sagittal rotation and translation extracted from the continuous-time description of intervertebral motion and as obtained in clinical setting. The locations of the instantaneous center of rotation have been compared to clinical estimates of finite center of rotation.

Results achieved with the proposed methodology offer a better representation of intervertebral kinematics with respect to manual landmarking and other automated approaches. Fluoroscopic image denoising improves image quality that can be resulted comparable to that expected from more expensive sensors or higher X-ray dosage. In particular, spatial adaptive filtering, specifically designed for signal-dependent noise, has been proved to improve the vertebrae recognition procedure providing a good trade-off between noise reduction and edge preservation in fluoroscopic images. Naturally, to fully take advantage of the potential of the denoising algorithm, an accurate noise modeling have been investigated. Continuous-time representation of intervertebral motion has provided an improvement of the information available from functional radiography and allowed to describe the actual instantaneous center of rotation during the entire segmental motion. This may have important clinical implications in diagnosis of segmental instability and evaluation of prosthetic implant.

In the future, the application of denoising algorithms combined to more complex gradient operators can be explored in order to further improve the accuracy of vertebrae recognition. The design of an opportune shape of vertebral template which includes only unambiguous vertebral edges (without including other parts of adjacent vertebrae) is also suggested. This can be particularly useful for cervical spine analysis due to the more complex anatomy of cervical vertebrae. Furthermore, a new spinal calibration model that more closely reproduces actual *in vivo* conditions should be adopted in order to obtain a more accurate and reliable assessment of estimation methods of intervertebral kinematics. Future works should also concentrate on definition of normal intervertebral path (healthy subjects) and identification of abnormal paths and their association to specific spine pathologies. Application on assessment of rehabilitation, physical therapy and prosthesis implant performance might be successively explored.

Appendix A

Anatomy of lumbar spine

Lumbar spine is the lower region of spinal column, as shown in Figure A.1. In a human, there are five lumbar vertebrae connecting proximally to the thoracic spine and distally to the sacrum. Each vertebra is often referred to as a 'level' and represented with an 'L' to define the lumbar spine and a number to specify the particular level. The individual lumbar vertebrae are designated L1 (being the most proximal vertebra), L2, L3, L4 and L5 (being the most distal vertebra).

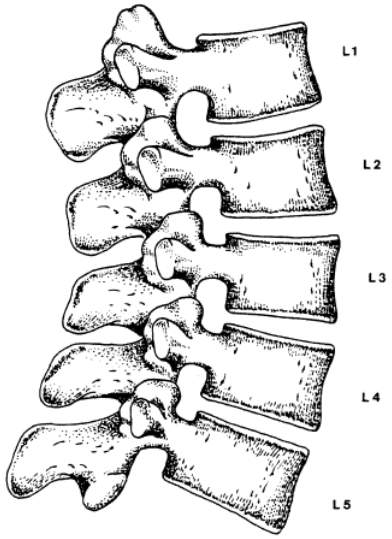

Figure A.1. Lumbar spine (from Bogduk, 1997).

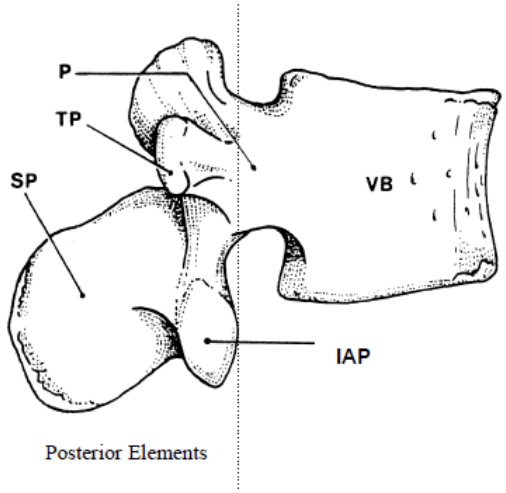

Figure A.2. Bony anatomy of lumbar vertebrae: VB – Vertebral Body; TP – Transverse Process; SP – Spinous Process; P – Pedicle; L – Lamina; SAP – Superior Articulating Process; IAP – Inferior Articulating Process (from Bogduk, 1997).

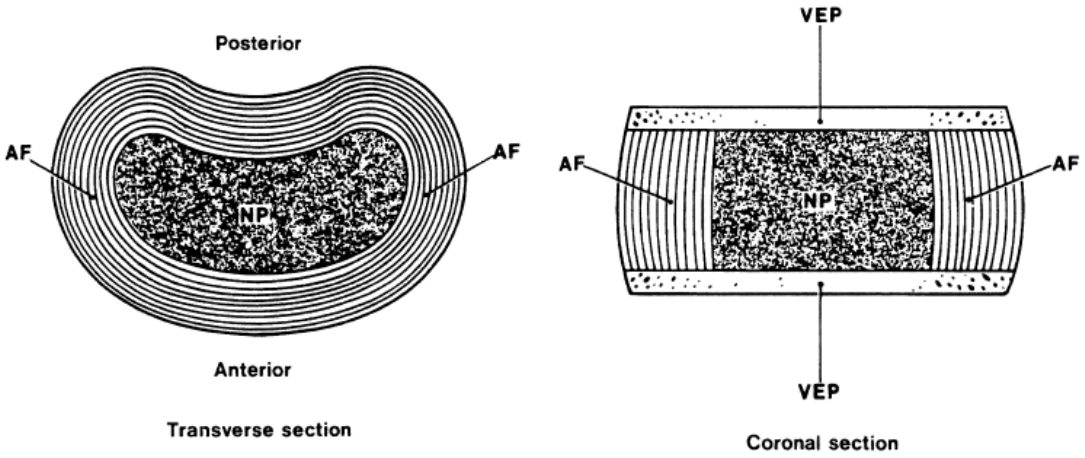

Figure A.3. Anatomy of the intervertebral disc: AF – Anulus Fibrosus; NP – Nucleus Pulposus; VEP – Vertebral Endplate (from Bogduk, 1997).

The bony anatomy of each vertebra is shown in Figure A.2. The anterior portion of the vertebra consists of the vertebral body. The vertebral body is the main load bearing structure of the vertebra. The superior and inferior surfaces of the vertebral bodies are flat to enhance their load carrying capacity. The vertebral body consists of an external shell of cortical bone surrounding a core of cancellous bone. The trabeculae of the cancellous core are arranged in a grid type pattern longitudinally to improve strength and allow dynamic flexibility during loading of spine.

Lumbar spine also consists of a complex array of soft tissue elements. The major soft tissues are intervertebral disc, spinal musculature and ligaments. In particular, intervertebral disc is thought to have an important role in contributing and controlling the spinal motion. As a result, disc degeneration is usually considered the primary cause of segmental instability.

Intervertebral disc is the soft tissue present between adjacent vertebral bodies. Any two adjacent vertebrae and their intervening intervertebral disc are generally termed as motion segment. Intervertebral disc height is the vertical distance between adjacent vertebral bodies. As can be seen from Figure 3.8, intervertebral disc varies from front to back. Anteriorly the disc height is larger than in the posterior disc. The anatomy of the intervertebral disc is shown in Figure A.3. Each intervertebral disc consists of a central, fluid-like mass called the nucleus pulposus. Peripherally to the nucleus pulposus the anulus fibrosus is observable. It consists of discontinuous concentric sheets or lamellae of collagen fibers. Both superiorly and inferiorly to the nucleus pulposus and the inner rings of the anulus fibrosus are then the vertebral endplates.

The function of intervertebral disc is three-fold. Firstly, it serves to bind adjacent vertebral bodies together. Secondly, it allows for load transfer from one vertebral body to an adjacent vertebral body. Thirdly (and probably the most important), it allows for movement of vertebrae.

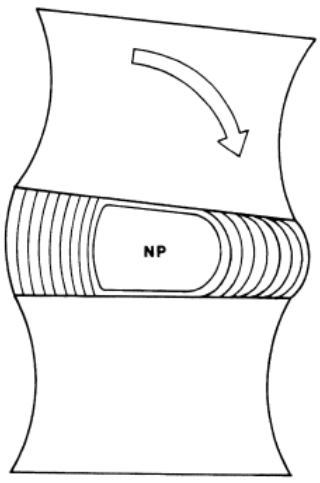

Figure A.4. Bending (flexion-extension) of the lumbar motion segment (from Bogduk, 1997).

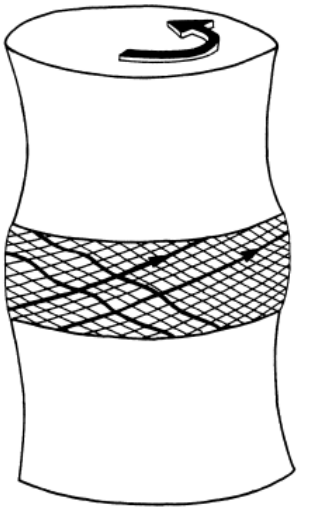

Figure A.5. Axial rotation of the lumbar motion segment (from Bogduk, 1997).

The knowledge of the forces/loads acting on the intervertebral disc during spinal motion can tell us something about the mechanical behavior of each motion segment. Rotation of one vertebra with respect to another in the sagittal (i.e. flexion and extension) or coronal (i.e. lateral bending) planes produces a combination of compressive and tensile loading to the disc. The region of the disc in the direction of motion and in front of the point of rotation will experience a compressive load. The region behind the centre of rotation and in the opposite direction of motion will experience tension. This is shown in Figure A.4. Rotation in the transverse plane (i.e. axial rotation or twisting) invokes a different mechanism in the disc to carry the load. As one vertebra twists relative to another, the anular fibers oriented in the direction of the rotation are loaded, while the fibers oriented away from the direction of rotation slacken (see Figure A.5). Hence, only half of the anular fibres are used to resist axial rotation. However, if torsion is performed under a physiological compressive load, tension of the fibers in the opposite direction to loading is maintained.

Appendix B

Fluoroscopic image intensifier

X-ray fluoroscopy provides digital-television viewing of anatomical structures inside the body with an acceptable, low X-ray dose. The components included in a modern fluoroscopic imaging system are shown in Figure B.1. Some components are similar to those included in systems used exclusively for radiography, whereas others are unique to fluoroscopy. For instance, additional apparatus are typically attached to allow for image recording, such as a spot-film device, film changer, photospot camera, cine camera, or analog-to-digital converter.

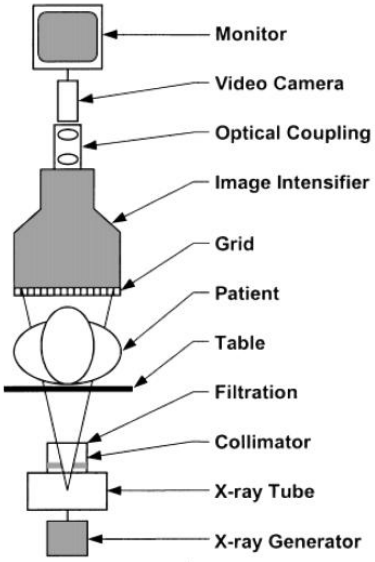

Figure B.1. Diagram shows the components of a fluoroscopic imaging chain (from Schueler, 2000

The image intensifier is surely the most important component of modern fluoroscopic equipments providing the brightness gain necessary to reduce X-ray dosage to the patient during the long acquisition of anatomical dynamic images. The image intensifier converts incident X-rays into a minified visible light image and, in the process, amplifies the image brightness by about 10,000 times for better visibility to the viewer. The major components of an image intensifier include an input layer (photocathode) to convert X-rays to electrons, electron lenses to focus the electrons, an anode to accelerate them, and an output layer (fluorescent screen) to convert them into a visible image (Figure B.2). An optical coupling system generally distributes light from the image intensifier output window to a video camera and/or other digital image recording devices for post-processing. All the components of the image intensifier are contained within an evacuated bottle. As a result of the acceleration of the electrons and image minification, the illumination level of the output image compared with that of the input image is greatly increased. This illumination increase, known as brightness gain, ranges from 5,000 to 20,000. The conversion factor is another measure of image intensifier brightness gain. In modern image intensifiers, conversion factors are 100–300 cd × m^{-2}/mR × s^{-1}, where cd × m^{-2} is the unit of measure of the light output of the image intensifier and mR × s^{-1} is the unit of measure of the X-ray exposure rate into the image intensifier. Image intensifiers can be also described by their contrast ratio, spatial resolution or detected quantum efficiency.

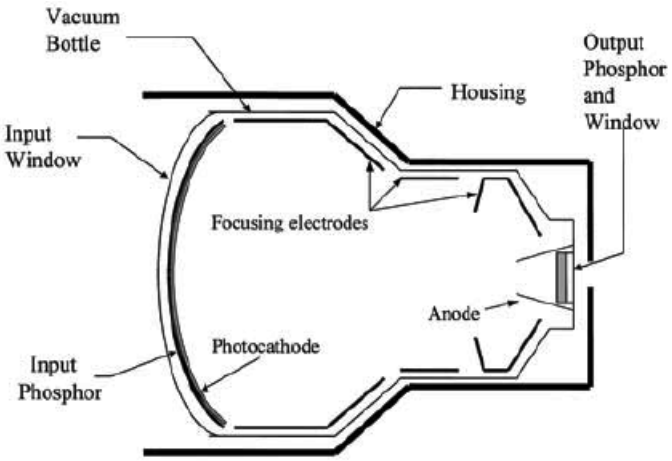

Figure B.2. Cross-sectional schematic of an image intensifier shows its major components (from Wang and Blackburn, 2000).

Image intensifiers are available with different diameter input windows of 10–40 cm. The selection of the diameter depends on the maximum FOV (field of view) requirements of the clinical application. Fluoroscopic systems designed for extremities may be configured with a 10–15-cm-diameter image intensifier, whereas a 40-cm-diameter unit is useful for imaging the abdomen or peripheral vasculature. Most image intensifiers also allow selection of a magnification mode. In magnification mode, the central circular area of the input layer is focused onto the full output layer by adjusting the voltage of the electron optics electrodes. Multiple magnification mode sizes are available on most fluoroscopic systems.

Appendix C

Fluoroscopic difference-image modeling by Skellam distribution

At low exposure levels the difference K between two independent X-ray photon counts N_1 and N_2 each having Poisson distribution can be modeled as Skellam-distributed (Skellam, 1946):

$$\mathcal{S}_{N_1,N_2}(K = N_1 - N_2) = e^{-(\lambda_1+\lambda_2)}\left(\frac{\lambda_1}{\lambda_2}\right)^{\frac{K}{2}} I_k\left(2\sqrt{\lambda_1\lambda_2}\right)$$

where λ_1 and λ_2 are the expected photon counts and $I_k(z)$ is the modified Bessel function of the first kind. The mean and variance of the Skellam distribution are given by:

$$E[K] = E[N_1] - E[N_2], \quad var[K] = E[N_1] + E[N_2]$$

with

$$E[N_1] = var[N_1] = \lambda_1, \quad E[N_2] = var[N_2] = \lambda_2$$

for the properties of the Poisson distributions.

Image intensity of the difference between two fluoroscopic images at the position r = $[x,y]^T$ is linearly dependent on the difference between the numbers of detected photons at that position and can be, in turn, characterized as a Skellam distribution:

$$D(r) \sim \mathcal{S}_{G_1,G_2}(D(r) = G_1(r) - G_2(r)) \sim c_d \mathcal{S}_{N_1,N_2}(K(r) = N_1(r) - N_2(r)).$$

If fluoroscopic static (i.e. motionless) images are adopted (i.e. $E[G_1(r)] \cong E[G_2(r)]$), the mean and variance of difference-image intensity result:

$$E[D(r)] = c_d\{E[G_1(r)] - E[G_2(r)]\} \cong 0$$

and

$$var[D(r)] = c_d\{E[G_1(r)] + E[G_2(r)]\} \cong 2c_d E[G(r)].$$

Therefore, given a fluoroscopic sequence the noise variance of the differences between pairs of fluoroscopic static frames at an image location (pixel) is linearly dependent on the mean of the raw pixel values (g) at that location:

$$\widehat{\sigma_D^2(r)} = 2c_d \mu\big(\widehat{g(r)}\big).$$

Once estimated the Skellam parameters, the characteristics of the fluoroscopic noise can be easily derived (i.e. Skellam noise variance is proportional to the Poisson noise variance). Noise Skellam modeling requires, however, that noise components must be uncorrelated frame by frame (Skellam, 1946; Hwang et al., 2007a; Hwang et al., 2007b). This assumption can be assumed only if the lag (i.e. persistence of luminescence) of the fluoroscopic device is shorter than the sampling interval. Older image intensifier had phosphors with lag times on the order of 30–40 ms, while current image intensifier tubes have lag times of approximately 1 ms (Wang and Blackburn, 2000). Therefore, the sampling frequency should be at least less than 25 frames per second to consider noise sample uncorrelated between two subsequent images.

Figures C.1 shows the experimental observations of the image noise level against the mean pixel intensity obtained from difference-images between about 100 fluoroscopic static images of a step phantom. The clipping phenomena at the extremes of the pixel value data range are observable.

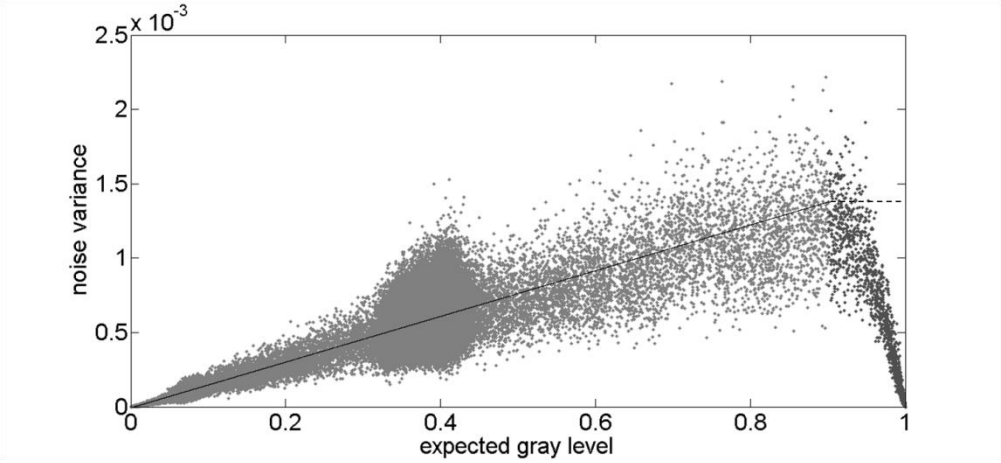

Figure C.1. Sample noise variance (bright-gray points) obtained by difference-images from a fluoroscopic sequence of a step phantom. The estimated mean-variance characteristic is shown as a solid black line. The clipped observations (dark-gray points) have been excluded from the analysis (from Cerciello et al., 2011a).

Bibliography

Aach, T., Kunz, D., 1996. Noise Reduction and Image Enhancement Algorithms for Low-Dose X-Ray Fluoroscopy. In: Proceedings of Bildverarbeitung für die Medizin: Algorithmen, Systeme, Anwendungen, Aachen, Germany, 95–100.

Adams, M.A., McNally, D.S., Dolan, P., 1996. 'Stress' distributions inside intervertebral discs. The effects of age and degeneration. Journal of Bone and Joint Surgery, British Volume 78(6), 965-972.

Amer A., Dubois E., 2005. Fast and Reliable Structure-Oriented Video Noise Estimation, IEEE Transaction. on Circuits and Systems for Video Technology, IEEE Proceedings 15, 113–118.

Anderson, J.A.D., Sweetman, B.I.A., 1975. Combined flexirule/hydrogoniometer for measurement of lumbar spine and its sagittal movement. Rheumatology & Rehabilitation 14, 173-179.

Anderst, W.J., Vaidya, R., Tashman, S., 2008. A technique to measure three-dimensional in vivo rotation of fused and adjacent lumbar vertebrae, Spine Journal, 2008, 8(6), 991-997.

Argyriou, V., Vlachos, T., 2003. Estimation of sub-pixel motion using gradient cross-correlation. Electronic Letters 39(13), 980-982.

Auerbach, J.D., Wills, B.P., McIntosh, T.C., Balderston, R.A., 2007. Evaluation of spinal kinematics following lumbar total disc replacement and circumferential fusion using in vivo fluoroscopy. Spine 32(5), 527-536.

Axelsson, P., Johnsson, R., Stromqvist, B., 1992. Effect of lumbar orthosis on intervertebral mobility. A roentgen stereophotogrammetric analysis. Spine 17, 678–681.

Barrett, H.H., Swindell, W., 1981. Radiological imaging. New York Academic, New York, 29-61.

Bifulco, P., Cesarelli, M., Allen, R., Sansone, M., Bracale, M., 2001. Automatic Recognition of Vertebral Landmarks in Fluoroscopic Sequences for Analysis of Intervertebral Kinematics. Journal of Medical and Biological Engineering and Computing 39 (1), 65-75.

Bifulco, P., Sansone, M., Cesarelli, M., Allen, R., Bracale, M., 2002. Estimation of out-of-plane vertebra rotations on radiographic projections using CT data: a simulation study. Medical Engineering & Physics 24(4), 295-300.

Bifulco, P., Cesarelli, M., Romano, M., Allen, R., Cerciello, T., 2009. Vertebrae tracking through fluoroscopic sequence: a novel approach. In: Proceedings of the World Congress on Medical Physics and Biomedical Engineering: The Triennial Scientific Meeting of the IUPESM, Munich, Germany, Springer IFMBE Proceedings 25(4), 619-622.

Bifulco, P., Cesarelli, M., Allen, R., Romano, M., Fratini, A., Pasquariello, G., 2010. 2D-3D Registration of CT Vertebra Volume to Fluoroscopy Projection: A Calibration Model Assessment. EURASIP Journal on Advances in Signal Processing (10), 1-8.

Bifulco, P., Cesarelli, M., Cerciello, T., Romano, M., 2012 (*expected*). A continuous description of intervertebral motion by means of spline interpolation of kinematic data extracted by videofluoroscopy. Journal of Biomechanics (*submitted: under second revision*).

Blumenthal, S., McAfee, P.C., Guyer, R.D., et al., 2005. A prospective, randomized, multicenter Food and Drug Administration investigational device exemptions study of lumbar total disc replacement with the CHARITE artificial disc versus lumbar fusion: part I: evaluation of clinical outcomes. Spine 30, 1565–1575 discussion E387-91.

Bogduk, N., Amevo, B., Pearcy, M., 1995. A biological basis for instantaneous centres of rotation of the vertebral column. Proceedings of the Institution of Mechanical Engineers, Part H. Journal of Engineering in Medicine 209, 177-183.

Bogduk, N., 1997. Clinical Anatomy of the Lumbar Spine and Sacrum, 3rd edition. Churchill Livingstone, Melbourne.

Bogduk, N., Mercer, S., 2000. Biomechanics of the cervical spine. I: Normal kinematics. Clinical Biomechanics 15, 633-648.

Boos, N., Rieder, R., Schade, V., Spratt, K.F., Semmer, N., Aebi, M., 1995. The diagnostic accuracy of MRI, work perception, and psychosocial factors in identifying symptomatic disc hisniations. Spine 20, 2613-2625.

Bosco, A., Bruna, A., Messina, G., Spampinato, G., 2005. Fast Method for Noise Level Estimation and Denoising. In: Proceedings of International Conference on Consumer Electronics, Las Vegas, 2005, SPIE Proceedings, 211–212.

Bram, J., Zanetti, M., Min, K., Jodler, J., 1998. MR abnormalities of the intervertebral disk and adjacent bone marrow as predictors of segmental instability of the lumbar spine. Acta Radiologica 39, 18–23.

Breen, A.C., Allen, R., Morris, A., 1989. Spine kinematics: a digital videofluoroscopic technique. Journal of Biomedical Engineering 11, 224-228.

Breen, A.C., 1991. The measurement of the kinematics of the human spine using videofluoroscopy and image processing. PhD thesis, University of Southampton, Southampton.

Breen, A.C., Muggleton, J.M., Mellor, F.E., 2006. An objective spinal motion imaging assessment (OSMIA): reliability, accuracy and exposure data. BMC Musculoskeletal Disorders 7(1), 1-10

Brunelli, R., Poggio, T., 1993. Face Recognition: Features versus Templates. IEEE Transaction Pattern Analysis and Machine Intelligence 15(10), 1042-1052.

Burkhart, T.A., Dunning, C.E., Andrews, D.M, 2011. Determining the optimal system-specific cut-off frequencies for filtering in-vitro upper extremity impact force and acceleration data by residual analysis. Journal of Biomechanics 44, 2728–2731.

Burton, A., Tillotson, M., 1988. Reference values for 'normal' regional lumbar sagittal mobility. Clinical Biomechanics 3 (2), 106-113.

Cerciello, T., Bifulco, P., Cesarelli, M., Romano, M., Allen, R., 2009. Automatic vertebra tracking through dynamic fluoroscopic sequence by smooth derivative template matching. In: Proceeding of the 9th International Conference on Information Technology and Applications in Biomedicine, Larnaca, Greece, IEEE Proceedings, 1-4.

Cerciello, T., Bifulco, P., Cesarelli, M., Paura, L., Pasquariello, G., Allen, R., 2010a. Noise reduction in fluroscopic image sequences for joint kinematics analysis. In: Proceedings of the 22nd Mediterranean Conference on Medical and Biological Engineering and Computing, Chalkidiki, Greece, Springer IFMBE Proceedings, 29, 323-326.

Cerciello, T., Bifulco, P., Cesarelli, M., Romano, M., D'Antò, M., Pasquariello, G., 2010b. Continuous description of intervertebral kinematics by spline interpolation of motion data obtained processing fluoroscopic lumbar sequences. In: Proceedings of the Second National Congress of Bioengineering, Turin, Italy, Atti del Congresso Nazionale di Bioingegneria, Pàtron Editore, 1-2.

Cerciello, T., Cesarelli, M., Paura, L., Bifulco, P., Romano, M., Allen, R., 2011a. Noise-parameter modeling and estimation for X-ray fluoroscopy. In: Proceedings of the 4th International Symposium on Applied Sciences in Biomedical and Communication Technologies, Barcelona, Spain, ACM Proceedings, 1-5.

Cerciello, T., Romano, M., Bifulco, P., Cesarelli, M., Allen R., 2011b. Advanced template matching method for estimation of intervertebral kinematics of lumbar spine. Medical Engineering & Physics 33 (10), 1293-1302.

Challis, J.H., 1995. An examination of procedures for determining body segment attitude and position from noisy biomechanical data. Medical Engineering & Physics 17(2), 83-90.

Challis, J.H., 2001. Estimation of the finite center of rotation in planar movements. Medical Engineering & Physics 23 (1), 227–233.

Chan, C.L., Katsaggelos, A.K., Sahakian, A.V., 1993. Image Sequence Filtering in Quantum-Limited Noise with Applications to Low-Dose Fluoroscopy. IEEE Transactions on Medical Imaging 12(3), 610-621.

Chen, J., Katona, T.R., 1999. The limitations of the instantaneous centre of rotation in joint research. Journal of Oral Rehabilitation 26, 274-279.

Cholewicki, J., McGill, S.M., Wells, R.P., Vernon, H., 1991. Method for measuring vertebral kinematics from videofluoroscopy. Clinical Biomechanics 6(2), 73-78.

Cossette, J.W., Farfan, H.F, Robertson, G.H., Wells R.V., 1971. The instantaneous center of rotation of the third lumbar intervertebral joint. Journal of Biomechanics 4, 149-153.

Crisco, J.J., Chen, X., Panjabi, M.M., Wolfe, S.W.. Optimal marker placement for calculating the instantaneous center of rotation. Journal of Biomechanics 27,1183–1187.

Crouse, M.S., Nowak, R.D., Baraniuk, R.G., 1998. Wavelet-based statistical signal processing using hidden Markov models. IEEE Transactions on Signal Processing 46(4), 886 – 902.

D'Amico, M., Ferrigno, G., 1992.Comparison between the more recent techniques for smoothing and derivative assessment in biomechanics. Medical and Biological Engineering and Computing 30(2), 193-204.

D'Antò, M., Cesarelli, M., Bifulco, P., Romano, M., Fiore, F., Cerciello, V., Cerciello, T., 2010. Perfusion CT of the liver: slop method analysis. In: Proceedings of the Second National Congress of Bioengineering, Turin, Italy, Atti del Congresso Nazionale di Bioingegneria, Pàtron Editore, 1-2.

Dabov, K., Foi, A., Katkovnik, V., Egiazarian, K., 2007. Image denoising by sparse 3-D transform-domain collaborative filtering. IEEE Transactions on Image Processing 16(8), 2080-2095.

Dickey, J.P., Pierrynowski, M.R., Bednar, D.A., Yang, S.X., 2002. Relationship between pain and vertebral motion in chronic low-back pain subjects. Clinical Biomechanics 17, 345-352.

Dimnet, J., Pasquet, A., Krag, M.H., Panjabi, M.M., 1982. Cervical spine motion in the sagittal plane: Kinematics and geometric parameters. Journal of Biomechanics 15, 959-969.

Dimnet, J., Guinguand, M., 1984. The finite displacements vector's method: an application to the scoliotic spine**.** Journal of Biomechics 17(6), 397-408.

Dolan, P., Adams, M.A., 1993. The relationship between EMG activity and extensor moment generation in the erector spinae muscles during bending and lifting activities. Journal of Biomechanics 26, 513-522.

Dupuis, P.R., Yong-Hing, K., Cassidy, J.D., Kirkaldy-Willis, W.H., 1985. Radiological diagnosis of degenerative lumbar spinal instability. Spine 10, 262-266.

Elad, M., Aharon, M., 2006. Image denoising via sparse and redundant representations over learned dictionaries. IEEE Transactions On Image Processing 15(12), 3736-3745.

Farfan, H.F., Gracovetsky, S., 1984. The Nature of Instability. Spine 9(7), 714-719.

Fazel-Rezai, R., Shwedyk, E., 1998. Biomechanic signal filtering for dynamic analysis purpose: a quantitative comparison between different methods. Journal of Biomechanics 31(Supplement 1), 85.

Feng, G., 1998. Data Smoothing by Cubic Spline Filters. IEEE Transactions on signal processing 46(10), 2790-2796.

Foi, A., Alenius, S., Katkovnik, V., Egiazarian, K., 2007. Noise measurement for raw-data of digital imaging sensors by automatic segmentation of non-uniform targets. IEEE Sensors Journal 7, 1456–1461

Foi, A., Trimeche, M., Katkovnik, V., Egiazarian, K, 2008. Practical Poissonian-Gaussian noise modeling and fitting for single-image raw-data. IEEE Transactions on Image Processing 17(10), 1737-1754.

Foi, A., 2009. Clipped noisy images: Heteroskedastic modeling and practical denoising. Signal Processing, 89(12), 2609-2629.

Frankel, V., Burstein, A., 1974.Biomechanics of the locomotor system. In: Ray, C.D. (Ed.), Medical engineering. Year book. Medical Publishers, Chicago, pp. 505-515.

Fujiwara, A., Lim, T.H., An, H.S., Nobuhiro, T., Jeon, C.H., Andersson, G.B.J., Haughton, V.M., 2000. The effect of disc degeneration and facet joint osteoarthritis on the segmental flexibility of the lumbar spine, Spine 25(23), 3036-3044.

Gertzbein, S.D., Holtby, R., Tile, M., Kapasouri, A., Chan, K.W., Cruickshank, B., 1984. Determination of a locus of instantaneous centers of rotation of the lumbar disc by moire fringes. A new technique. Spine 9, 409-413.

Gertzbein, S.D., Seligman, J., Holtby, R., Chan, K.H., Kapasouri, A., Tile, M., Cruickshank, B., 1985. Centrode patterns and segmental instability in degenerative disc disease. Spine 10, 257-261.

Gilboa, G., Sochen, N., Zeevi, Y.Y., 2006. Variational denoising of partly textured images by spatially varying constraints. IEEE Transactions on Image Processing 15(8), 2281 – 2289.

Gonzalez, R.C., Woods, R.E., 1992. Digital Image Processing, third edition. Addison-Wesley, Reading, Massachusetts.

Haher, T.R., O'Brien, M., Felmly, W.T., Welin, D., Perrier, G., Choueka, J., Devlin, V., Vassiliou, A., Chow, G., 1992.Instantaneous axis of rotation as a function of the three columns of the spine. Spine 17, S149-S154.

Harrison, R.M., Kotre, C.J., 1986. Noise and threshold contrast characteristics of a digital fluoroscopic system. Physics in Medicine and Biology 31, 512-586.

Hensel, M., Pralow, T., Grigat, R.R., 2007. Modeling and Real-Time Estimation of Signal-Dependent Noise in Quantum-Limited Imaging. In: Proceedings of the 6th WSEAS International Conference on Signal Processing, Robotics and Automation, Corfu Island, Greece, 183-191.

Hindle, R.J., Pearcy, M.J., Cross, A., 1990. Mechanical function of the human lumbar interspinous and supraspinous ligaments. Journal of Biomedical Engineering 12, 340-344.

Hirakawa, K., Parks, T.W., 2006. Image denoising using total least squares. IEEE Transaction on Image Processing 15(9), 2730-42.

Hwang, Y., Kim, J.S., Kweon, I.S., 2007a. Sensor noise modeling using the Skellam distribution: Application to the color edge detection. IEEE Conference on Computer Vision and Pattern Recognition, Minneapolis, Minnesota, Stati Uniti, IEEE, 1-8.

Hwang, Y., Kweon, I.S., Kim, J.S., 2007b. Color edge detection using the Skellam distribution as a sensor noise model. In: Proceedings of Annual Conference Society of Instrumentation and Control Engineers, Takamatsu, Japan IEEE, 1972-1979.

Hwang, H., Hipp, J.A., Ben-Galim, P., Reitman, C.A., 2008. Threshold cervical range-of-motion necessary to detect abnormal intervertebral motion in cervical spine radiographs. Spine 33(8), 261-267.

Junghanns, H., 1931. Spondylolisthesis ohne spalt in zwischengelenstuck. Archiv fur Orthopadische und Unfall-Chirurgie. l 129, 118–127.

Kirkaldy-Willis, W.H., Farfan, H.F., 1982. Instability of the lumbar spine. Clinical Orthopaedics and Related Research 1165, 110–123.

Knutsson, F., 1944. The instability associated with disc degeneration in the lumbar spine. Acta Radiologica 25,593–609.

Kondracki, M., 2011. Clinical applications of digitized videofluoroscopy in the lumbar spine. PhD thesis, University of Southampton, Southampton.

Krismer, M., van Tulder, M., 2007. Low back pain (non-specific). Best Practice & Research Clinical Rheumatology 21(1), 77-91.

Lam, S.C., McCane, B., Allen, R., 2009. Automated tracking in digitized videofluoroscopy sequences for spine kinematic analysis. Image and Vision Computing 27, 1555-1571.

Le Huec, J.C., Mathews, H., Basso, Y., et al., 2005. Clinical results of Maverick lumbar total disc replacement: two-year prospective follow-up. Orthop. Clin. North Am. 36, 315–322.

Lee, S.W., Draper, E.R., Hughes, S.P., 1997. Instantaneous center of rotation and instability of the cervical spine.A clinical study. Spine 22(6), 641-648.

Leone, A., Guglielmi, G., Cassar-Pullicino, V.N., Bonomo, L., 2007. Lumbar Intervertebral Instability: A Review. Radiology 245(1), 62-77.

Lewis, J.P., 1995. Fast Template Matching. Vision Interface, 120-123.

Lo, C.M., Sawchuk, A.A., 1979. Nonlinear restoration of filtered images with Poisson noise. In: Applications of digital image processing III; Proceedings of the Seminar, San Diego, California, 84-91.

Luo, Z.P., Buttermann, G.R., Lewis, J.L., 1996. Determination of spinal facet joint loads from extra articular strains – a theoretical validation. Journal of Biomechics 29, 785–790.

Manek, N.J., MacGregor, A.J., 2005. Epidemiology of Back Disorders: Prevalence, Risk Factors, and Prognosis. Current Opinion in Rheumatology 17(2), 134-140.

Mansour, M., Spiering, S., Lee, C., Dathe, H., Kalscheuer, A.K., Kubein-Meesenburg, D., Nägerl, H., 2004. Evidence for IHA migration during axial rotation of a lumbar spine segment by using a novel high-resolution 6D kinematic tracking. Journal of Biomechanics 37, 583–592.

McCane, B., Abbott, J.H., King, T., 2005. On calculating the finite centre of rotation for rigid planar motion. Medical Engineering & Physics 27(1), 75-79.

McAfee, P.C., Cunningham, B., Holsapple, G., et al., 2005. A prospective, randomized, multicenter Food and Drug Administration investigational device exemption study of lumbar total disc

replacement with the CHARITE artificial disc versus lumbar fusion: part II: evaluation of radiographic outcomes and correlation of surgical technique accuracy with clinical outcomes. Spine 30, 1576–1583 discussion E388-90.

McCane, B., King, T.I., Abbott, J.H., 2006. Calculating the 2D motion of lumbar vertebrae using splines. Journal of Biomechanics 39, 2703-2708.

McGill, S.M., Brown, S., 1992. Creep response of the lumbar spine to prolonged full flexion. Clinical Biomechics 7, 43-46.

McLaughlin, T.M., Diltman, C.J., Lardner, T.J., 1977. Biomechanical analysis with cubic spline functions. Research Quarterly 48(3), 569-582.

Meriam, J.L., Kraige, L.G., 2002. Engineering Mechanics: Dynamics (5th Edition). John Wiley & Sons, New York.

Morgan, F.P., King, T., 1957. Primary instability of lumbar vertebrae as a common cause of low back pain. Journal of Bone Joint Surgery British 39-B, 6–22.

Muggleton, J.M., Allen, R., 1997. Automatic location of vertebrae in digitized videofluoroscopic images of the lumbar spine. Medical Engineering & Physics 19(1), 77-89.

Murata, M., Morio, Y., Kuranobu, K.., 1994. Lumbar disc degeneration and segmental instability: a comparison of magnetic resonance imaging and plain radiographs of patients with low back pain. Archives of Orthopaedic and Trauma Surgery 113, 297–301.

Nachemson, A.L., Schultz, A.B., Berkson, M.H., 1979. Mechanical properties of human lumbar spine motion segments: influence of age, sex, disc level, and degeneration. Spine 4, 1–8.

Nägerl, H., Hawellek,T., Lehmann, A., Hubert, J., Saptschak, J., Dörner, J., Raab, B.W., Fanghänel, J., Kubein-Meesenburg, D., Wachowski, M.M., 2008. Non-linearity of flexion-extension characteristics in spinal segments. Acta of Bioengineering and Biomechanics 11(4), 3-8.

Niosi, C.A., Oxland, T.R., 2004.Degenerative mechanics of the lumbar spine. The Spine Journal 4, 202S-208S.

Nizard, R.S., Wybier, M., Laredo, J.D. 2001. Radiologic assessment of lumbar intervertebral instability and degenerative spondylolisthesis. Radiologic Clinics of North America 39(1), 55-71.

Olsen S.I., 1993. Estimation of noise in images: An evaluation. In: Proceedings of CVGIP: Graphical Models and Image Processing 55, 319–323.

Panjabi, M., 1979. Centers and angles of rotation of body joints: a study of errors and optimization. Journal of Biomechanics 12, 911-920.

Panjabi, M.M., Goel, V.K., Walter, S.D., Schick, S., 1982. Errors in the center of and angle of rotation of a joint: An experimental study. Journal of Biomechanical Engineering 104, 232-237.

Panjabi, M.M., Krag, M.H., Dimnet, J.C., Walter, S.D., Brand, R.A., 1984. Thoracic spine centers of rotation in the sagittal plane. Journal of Orthopaedic Research 1, 387-394.

Panjabi, M., Chang, D., Dvorak, J., 1992a. An analysis of errors in kinematics parameters associated with in vivo functional radiographs. Spine 2, 200-205.

Panjabi, M., 1992b. The stabilizing system of the spine. Part I. Function, dysfunction, adaption, and enhancement. Journal of Spinal Disorder **5**(4), 383-389.

Panjabi, M.M., 1992c. The stabilizing system of the spine. Part II. Neutral zone and instability hypothesis. Journal of Spinal Disorders 5(4), 390-396.

Panjabi, M.M., 2003. Clinical spinal instability and low back pain. Journal of Electromyography and Kinesiology 13, 371-379.

Penning, L., Wilmink, J.T., van Woerden, H.H., 1984. Inability to prove instability. A critical appraisal of clinical radiological flexion-extension studies in lumbar disc degeneration. Diagnostic Imaging in Clinical Medicine 53: 186-192.

Pearcy, M., Portek, I., Shepherd, J., 1984a. Three-dimensional x-ray analysis of normal movement in the lumbar spine. Spine 9, 294-297.

Pearcy, M.J., Tibrewal, S.B., 1984b. Axial rotation and lateral bending in the normal lumbar spine measured by three-dimensional radiography. Spine 9(6), 582-587.

Pearcy, M.J., Shepherd, J., 1985. Is there instability in spondylolisthesis?. Spine 10, 175-177.

Pearcy, M.J., 1986. Measurment of back and spinal mobility. Clincal Biomechanics, 44-51,

Pearcy, M.J., Bogduk, N., 1988. Instantaneous axes of rotation of the lumbar intervertebral joints. Spine 13(9), 1033-41.

Pearcy, M.I., Hindle, R.J., 1989. New method for the non-invasive three-dimensional measurement of human back movement. Clinical Biomechics 4 (2),73-79.

Posner, I., White, A.A. 3rd, Edwards, W.T., Hayes, W.C., 1982. A biomechanical analysis of the clinical stability of the lumbar and lumbosacra spine. Spine 7, 374–389.

Portek, I., Pearcy, M.J., Reader, G.P., Mowat, A.G., 1983. Correlation between radiographic and clinical measurement of lumbar spine movement. British Journal of Rheumatology 22, 197–205. 77.

Putzier, M.,Funk,J.F.,Schneider,S.V.,etal.,2006.Charite total disc replacement — clinical and radiographical results after an average follow-up of 17 years. European Spine Journal 15,183–195.

Qiu, T.X., Teo, E.C., Lee, K.K., Ng, H.W., Yang, K., 2003. Validation of T10–T11 finite element model and determination of instantaneous axes of rotations in three anatomical planes. Spine 28, 2694–2699.

Reinsch, C.H., 1967. Smoothing by Spline Functions. Numerische Mathematik 10, 177-183.

Rosenberg, P., 1955. The R-center method, a new method for analyzing vertebral motion by x-rays. Journal of the American Osteopathic Association 1, 103-111.

Reichmann, S., Berglund, E., Lundgren, K., 1972. Das bewegungszentrum in der lendenwirbelsa¨ule bei flexion und extension. Z. Anat. Entwickl. 138, 283–287.

Reuleaux, F., 1875. The Kinematics of Machinery: Outline of a Theory of Machines (translated by A.B.W. Kennedy). Dover.

Rousseau, M.A., Bradford, D.S., Bertagnoli, R., Hu, S.S., Lotz, J.C., 2006a. Disc arthroplasty design influences intervertebral kinematics and facet forces. Spine Journal 6(3), 258-266.

Rousseau, M.A., Bradford, D.S., Hadi, T.M., Pedersen, K.L., Lotz, J.C., 2006b. The instant axis of rotation influences facet forces at L5/S1 during flexion/extension and lateral bending. European Spine Journal 15, 299-307.

SariAli, el-H., Lemaire, J.P., Pascal-Mousselard, H., Carrier, H., Skalli, W., 2006. In vivo study of the kinematics in axial rotation of the lumbar spine after total intervertebral disc replacement: long-term results: a 10-14 years follow up evaluation. European Spine Journal 15(10), 1501-1510.

Schmidt, H., Heuer, F., Claes, L., Wilke, H.J., 2008a. The relation between the instantaneous center of rotation and facet joint forces - A finite element analysis. Clinical Biomechanics 23, 270-278.

Schmidt, H., Heuer, F., Wilke, H.J., 2008b. Interaction between finite helical axes and facet joint forces under combined loading. Spine 33(25), 2741-2748.

Schneider, G., Pearcy, M.J., Bogduk, N., 2005. Abnormal motion in spondylolytic spondylolisthesis. Spine 30(10), 1159-64.

Schoenberg, I.J., 1964. Spline functions and the problem of graduation.Mathematics 52, 947-950.

Scholten, P.J.M., Veldhuizen, A.G., Grootenboer, H.J., 1988. Stability of the human spine: a biomechanical study. Clinical Biomechanics, 3(1), 27-33.

Selvik, G., 1989. Roentgen stereophotogrammetry. A method for the study of the kinematics of the skeletal system. Acta Orthopaedica Scandinavica, 60 (Suppl 232), 1-51.

Shaffer, W.O., Spratt, K.F., Weinstein, J., Lehmann, T.R., Goel, V., 1990. The consistency and accuracy of roentgenograms for measuring sagittal translation in the lumbar vertebra motion segment. Spine 15, 741–750.

Simonis C, 1994. Parallel calculation and analysis of spine kinematics using videofluoroscopy and image processing. PhD thesis, University of Southampton, Southampton.

Skellam, J.G., 1946. The frequency distribution of the difference between two poisson variates belonging to different populations. Journal of the Royal Statistical Society: Series A 109(3), 296.

Spiegelman, J.J., Woo, S.L.. A rigid-body method for finding centers of rotation and angular displacements of planar joint motion. Journal of Biomechics 20(7), 715-721.

Soini, J., Antti-Poika, I., Tallroth, K., Konttinen, Y.T., Honkanen, V., Santavirta, S., 1991. Disc degeneration and angular movement of the lumbar spine comparative study using plain and flexion-extension radiography and discography. Journal of Spinal Disorders 4, 183–187.

Stokes, I.A., Frymoyer, J.W., 1987. Segmental motion and instability. Spine 12, 688–691.

Subramanian, N., Reitman, C.A., Nguyen, L., Hipp, J.A., 2007. Radiographic assessment and quantitative motion analysis of the cervical spine after serial sectioning of the anterior ligamentous structure. Spine 32(5), 518-526.

Tallroth, K., Alaranta, H., Soukka, A., 1992. Lumbar mobility in asymptomatic individuals. Journal of Spinal Disorder 5, 481–484.

Van Mameren, H., Sanches, H., Beurgens, J., Drukker, J., 1992. Cervical spine motion in the sagittal plane (II) position of segmental averaged instantaneous centers of rotation: a cineradiographic study. Spine 17, 467-474.

Vint, P.F., Hinrichs,R.N., 1996. Endpoint error in smoothing and differentiating raw kinematic data: An evaluation of four popular methods. Journal of Biomechanics 29(12), 1637-1642.

Wachowski, M.M., Ackenhausen, A., Dumont, C., Fanghänel, J., Kubein-Meesenburg, D., Nägerl, H, 2007. Mechanical properties of cervical motion segments. The archive of mechanical engineering LIV(1), 5-15.

Yoshioka, T., Tsuji, H., Hirano, N., et al., 1990. Motion characteristic of the normal lumbar spine in young adults: instantaneous axis of rotation and vertebral center motion analyses. Journal of Spinal Disorder 3, 103–113.

Yochum, T.R., Rowe, L.J., 1996. Essentials of skeletal radiology, 2nd Ed. Williams and Wilkins, Baltimore.

Wachowski, M.M., Mansour, M., Lee, C., Ackenhausen, A., Spiering, S., Fanghänel, J., Dumont, C., Kubein-Meesenburg, D., Nägerl, H., 2009a. How do spinal segments move?. Journal of Biomechanics 42, 2286-2293.

Wachowski, M.M., Hubert, J., Hawellek, T., Mansour, M., Dorner, J., Kubein-Meesenburg, D., Fanghanel, J., Raab, B.W., Dumont, C., Nagerl, H, 2009b. Axial rotation in the lumbar spine following axial force wrench. Journal of Physiology and Pharmacology 60(Suppl. 8), 61-64.

Wachowski, M.M., Hawellek, T., Hubert, J., Lehmann, A., Mansour, M., Dumont, C., Dörner, J., Raab, B.W., Kubein-Meesenburg, D., Nägerl, H, 2010. Migration of the Instantaneous Axis of Motion during Axial Rotation in Lumbar Segments and Role of the Zygapophysial Joints. Acta of Bioengineering and Biomechanics 12(4), 39-47.

Wang, J., Blackburn, T.J., 2000. The AAPM/RSNA physics tutorial for residents: X-ray image intensifiers for fluoroscopy. Radiographics 20(5), 1471-1477.

Wang, X., Tian, B., Liang, C., Shi, D., 2008. Blind Image Quality Assessment for Measuring Image Blur. In: Proceedings of Congress on Image and Signal Processing, Sanya, Hainan, China, IEEE, 467-470.

White, A.A., Panjabi, M.M., The basic kinematics of human spine: a review of past and current knowledge. Spine 3 (1978), 12–20.

White, A.A., Panjabi, M.M., 1990. Clinical Biomechanics of the Spine. Lippincott Williams & Wilkins, Philadelphia.

Wilcox, R.K., 2006. An introduction to basic mechanics. Current Orthopaedics 20, 1-8.

Wilson, D.C., Niosi, C.A., Zhu, Q.A., Oxland, T.R., Wilson, D.R., 2006. Accuracy and repeatability of a new method for measuring facet loads in the lumbar spine. Journal of Biomechics 39, 348–353.

Woltring, H.J., 1985. On optimal smoothing and derivative estimation from noisy displacement data in biomechanics. Human Movement Science 4(3), 229-245.

Wood, G.A., Jennings, L.S., 1979. On the use of spline functions for data smoothing. Journal of Biomechanics 12, 477-479.

Wood, G.A., 1982. Data smoothing and differentiation procedures in biomechanics. Exercise and Sport Science Reviews 10(1), 308-362.

Wood, K.B., Popp, C.A., Transfeldt, E.E., Geissele, A.E., 1994. Radiographic evaluation of instability in spondylolisthesis. Spine 19:1697–1703.

Xia, Q., Wang, S., Kozanek, M., Passias, P., Wood, K., Li, G., 2010. In-vivo motion characteristics of lumbar vertebrae in sagittal and transverse planes. Journal of Biomechanics 43, 1905-1909.

Xu X., Chang, C.C., Faber, G.S., Kingma, I., Dennerlein, J.T., 2010a. Comparing polynomial and cubic spline interpolation of segment angles for estimating L5/S1 net moment during symmetric lifting tasks.Journal of Biomechanics 43(3), 583-586.

Xu, X., Chang, C.C., Faber, G.S., Kingma, I., Dennerlein, J.T., 2010b. Interpolation of segment Euler angles can provide a robust estimation of segment angular trajectories during asymmetric lifting tasks. Journal of Biomechanics 43, 2043-2048.

Zheng, Y., Nixon, M.S., Allen, R., 2004. Automated segmentation of lumbar vertebrae in digital videofluoroscopic images. IEEE Transactions on Medical Imaging 23(1), 45-52.

Zigler, J., Delamarter, R., Spivak, J.M. et al., 2007. Results of the prospective, randomized, multicenter Food and Drug Administration investigational device exemption study of the ProDisc-L total disc replacement versus circumfer- ential fusion for the treatment of 1-level degenerative disc disease. Spine.32, 1155-62; discussion 1163.